LATTICE ANOMALIES AND MAGNETIC STATES IN Fe_5Si_3-Mn_5Si_3 ALLOYS

Thesis by

Chih Chieh Chao

In Partial Fulfillment of the Requirements
for the Degree of
Doctor of Philosophy

California Institute of Technology
Pasadena, California
1972

(Submitted April 6, 1972)

To Grace and Timothy

ACKNOWLEDGEMENT

The author wishes to express his deepest appreciation to Professor Pol E. Duwez and Dr. Chang-chyi Tsuei for their highly inspirational advice and continuing support and encouragement throughout this work. He is also deeply thankful to Professor Börje Persson for numerous stimulating and highly rewarding discussions. Many useful discussions with Dr. R. Hasegawa and his assistance in connection with the magnetization measurements are gratefully acknowledged. The author is also indebted to Dr. Thomas Sharon for many helpful discussions. This work was made possible through the help of Charles Young in the electrical resistance and Curie temperature measurements, F. Youngkin, J. Brown, J. Wysocki, S. Kotake and C. Geremia in technical assistance, and Mrs. Betty Wolar in typing the rough draft. It is a privilege to have Mrs. Ruth Stratton type the thesis.

Financial support was gratefully received from the Atomic Energy Commission and the California Institute of Technology.

To his parents who sent him to study in this country, the author wishes to express his heartiest gratitude for their constant prayers and continuing encouragement and support. He also wishes to acknowledge his sincere appreciation to his wife, Grace, for her never ending understanding and encouragement throughout the course of the present work.

ABSTRACT

The lattice anomalies and magnetic states in the $(Fe_{100-x}Mn_x)_5Si_3$ alloys have been investigated. Contrary to what was previously reported, results of x-ray diffraction show a second phase (α') present in Fe-rich alloys and therefore strictly speaking a complete solid solution does not exist. Mössbauer spectra, measured as a function of composition and temperature, indicate the presence of two inequivalent sites, namely 6(g) site (designated as site I) and 4(d) (site II). A two-site model (TSM) has been introduced to interpret the experimental findings. The compositional variation of lattice parameters a and c, determined from the x-ray analysis, exhibits anomalies at $x = 22.5$ and $x = 50$, respectively. The former can be attributed to the effect of a ferromagnetic transition; while the latter is due to the effect of preferential substitution between Fe and Mn atoms according to TSM.

The reduced magnetization of these alloys deduced from magnetic hyperfine splittings has been correlated with the magnetic transition temperatures in terms of the molecular field theory. It has been found from both the Mössbauer effect and magnetization measurements that for composition $0 \leq x < 50$ both sites I and II are ferromagnetic at liquid-nitrogen temperature and possess moments parallel to each other. In the composition range $50 < x \leq 100$, the site II is antiferromagnetic whereas site I is paramagnetic even at a temperature below the bulk Néel temperatures. In the vicinity of $x = 50$ however, site II is in a state of transition between ferromagnetism and antiferromagnetism. The present study also suggests that only Mn in site II are responsible for the antiferromagnetism in Mn_5Si_3 contrary to a previous report.

Electrical resistance has also been measured as a function of temperature and composition. The resistive anomalies observed in the Mn-rich alloys are believed to result from the effect of the antiferromagnetic Brillouin zone on the mobility of conduction electrons.

TABLE OF CONTENTS

INTRODUCTION

The intermetallic compounds Fe_5Si_3 and Mn_5Si_3 both crystallize in the $D8_8$ (Mn_5Si_3 type, hexagonal) structure$^{(1,2)}$ with the $P6_3/mcm$ space group symmetry.$^{(3)}$ This type of crystal structure was first determined by Amark et al.$^{(1)}$ and more recently by Aronsson.$^{(4)}$ According to Aronsson$^{(2)}$, Fe_5Si_3 and Mn_5Si_3 form a complete solid solution and results of his x-ray analysis show an anomaly in the compositional variation of both lattice parameters a and c. Similar anomalies observed in metallic hexagonal alloys such as MgIn have been interpreted in terms of the Fermi-surface--Brillouin-zone interactions.$^{(5)}$ In the past, a great deal of both theoretical and experimental work has been done in this field.$^{(5-15)}$ However, it is not immediately apparent that this is also the cause of anomalies observed in the $(Fe\text{-}Mn)_5Si_3$ alloys and the main purpose of the present study, in fact, is to clarify the physical origin of the lattice anomalies in the Fe_5Si_3-Mn_5Si_3 alloy system.

Magnetic properties of $Fe_5Si_3$$^{(16-18)}$ and $Mn_5Si_3$$^{(19)}$ have recently been studied and it is found that the former is ferromagnetic with a Curie point T_c ranging from 373^oK to 385^oK while the latter is antiferromagnetic with its Néel temperature $T_N = 68^oK$. Furthermore, the Fe and Mn atoms are known to have very similar electronic configurations. In view of these, it would be interesting to study how the magnetic states change as a function of alloy composition. It would also be interesting to see if there is any magnetic effect on the lattice spacing.

In the course of the present study a paper(20) on the Mössbauer and magnetic measurements of some of these alloys appeared. Unfortunately, due to the improper technique of alloy preparation, much of the results of Ref. 20 is doubtful. Furthermore, the lattice parameter anomalies were not touched in their work.

The present study involves experimental technique of x-ray diffraction, Mössbauer effect spectroscopy, magnetization measurements and electrical resistance measurements. A detailed description of these experimental procedures will be discussed in the next chapter. In Chapter III, some of the established theories relevant to the present work will be briefly reviewed. From the experimental results with their analysis presented in Chapter IV, a physical model will be introduced and applied in understanding much of the experimental findings. This will be treated in Chapter V. Finally, a summary with concluding remarks of the present study will be presented in the last chapter.

II. EXPERIMENTAL PROCEDURES

A. Preparation of Alloys

The Fe-Mn-Si alloys were prepared by induction melting of appropriate quantities of the constituents (99.99% pure Fe, 99.99% pure Mn and 99.999% pure Si) on a water-cooled silver boat(21) in an argon atmosphere. During the melting process a certain amount of Mn evaporated from the sample. This was compensated for by adding extra Mn to the initial weight of Mn. After melting, the ingot was carefully weighed to ensure that the composition was close to the nominal one. To obtain both the desired alloy phase and the homogeneity, the samples were annealed for approximately 9 days at 950°C.

It should be mentioned here that alumina crucible used in Ref. 20 would not be appropriate in preparation of these alloys for the reason that Mn reacts strongly with Al forming a number of possible second phases such as $MnAl_6$ and MnAl(22), for example.

B. X-Ray Diffraction

The Debye-Scherrer method(23) was used both to identify the alloy structure and to determine the lattice constants. The powdered specimen prepared by grinding the alloy and then passing it through a 325-mesh screen, was loaded into a thin-walled quartz capillary of 0.5 mm diameter. The capillary was then mounted on the rotating specimen holder of a 114.6 mm diameter Debye-Scherrer camera. The sample capillary must be centered in the incoming x-ray beam. Typical exposure was about 24 hours at 35 kV and 10 ma with vanadic acid filtered chromium radiation. Intense background was observed in the high angle region of the Bragg diffraction pattern due to fluorescent radiation and diffuse scattering. Appreciable reduction of background was achieved, however, by first doubling the exposure time and then bleaching the film with Farmer's reducer (Kodak R-4a).(24) Lattice parameters were corrected for film shrinkage, camera radius error, and specimen centering error by extrapolating against the Nelson-Riley function.

C. Mössbauer Effect Experiments

Figure 1 shows the schematic diagram of the Mössbauer effect apparatus used to obtain the γ ray resonance absorption spectra. The source in this case is 15 mCi of Co^{57} diffused in a Cu matrix. The absorber is the powdered specimen dispersed uniformly in a wax-disc of approximately 1.5 cm diameter. To achieve the maximum absorption, the optimum absorber thickness is found experimentally to contain 20-30 mg of Fe per square centimeter of the absorption area.

A current pulse proportional to the γ ray energy is generated whenever a transmitted photon is detected by a $Xe-Co_2$ proportional counter. This pulse is amplified and then analyzed for energy by a single channel analyzer, and only photons of energy corresponding to 14.4 keV transition are allowed to enter a multichannel analyzer. This multichannel analyzer with 512 channels produces a square wave with a period of 512×100 μsec, which is then integrated by an operational amplifier. This triangular wave is used as the reference signal to drive the velocity transducer(25) which produces the Doppler shift of the γ ray emitted by the source. As the source undergoes a periodic

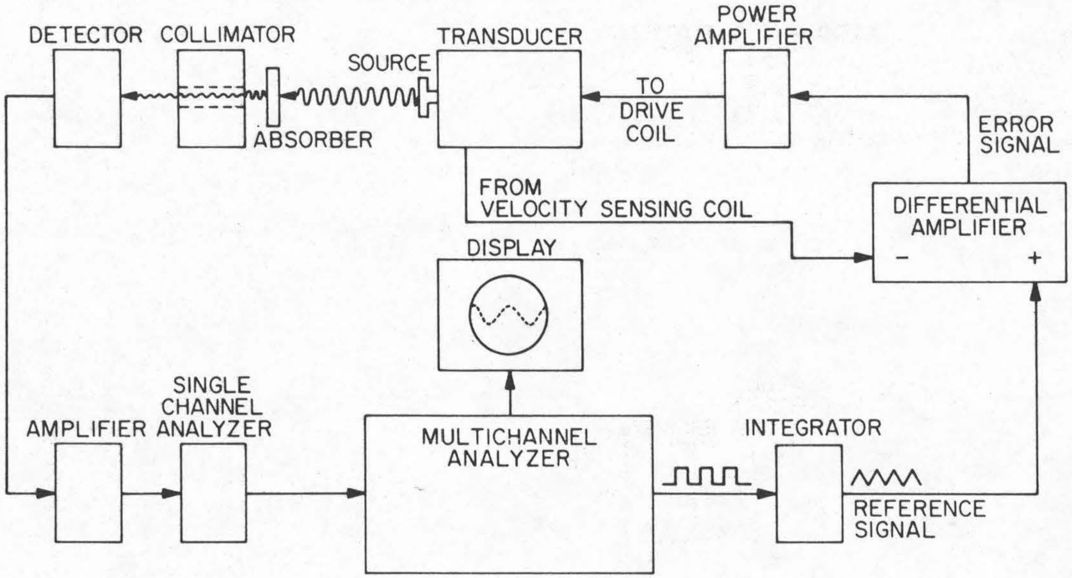

Fig. 1. Schematic diagram of the Mössbauer effect apparatus

parabolic motion corresponding to a triangular velocity wave, a clock inside the multichannel analyzer opens one channel after another for 100 μsec intervals. The actual motion of the source is sensed by a pickup coil which feeds the information back to compare with the reference signal through a differential amplifier. Thus by adjusting both the differential and power amplifiers the error signal may be minimized so that the transducer actually follows very closely the triangular velocity wave.

To calibrate the velocity scale, the data due to an Fe foil were least squares fitted to a six peak spectrum (Fig. 2), and the peak separation was assumed to be that of Preston et al (10.657 mm/sec for the outer peak separation).$^{(26)}$

Mössbauer effect was also measured at 77°K and 4.2°K using liquid-nitrogen and helium, respectively. Above room temperature, a specially designed oven was used to provide continuous temperature control with a stability of about ±0.5°K.

D. Magnetic Properties Measurements

Magnetic moments of alloys $(Fe_{100-x}Mn_x)_5Si_3$ for $x = 0,10,\cdots,70$ were measured between 4.2°K and 300°K and in magnetic fields up to 7.3 kG. The measurements were made in the null-coil pendulum magnetometer whose design and performance are described in detail in Ref. 27. The reciprocal susceptibility and magnetization as functions of temperature, both derived from magnetization vs. magnetic field, are useful in confirming the magnetic states of the samples.

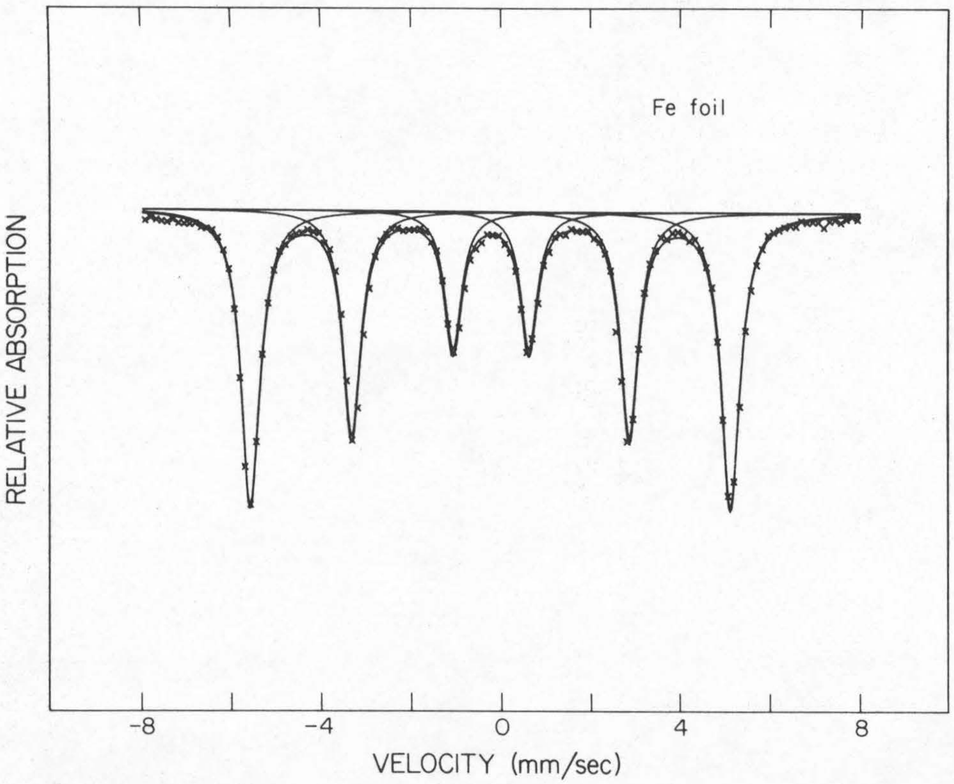

Fig. 2. Mössbauer absorption spectrum of a .001" Fe foil

E. Ferromagnetic Transition Temperature Measurements

In the ferromagnetic region, the Curie point was determined by means of an AC inductance Wheatstone bridge with a PAR lock-in amplifier as a null detector. The output signal of the lock-in amplifier was plotted on an X-Y plotter against temperature which was measured by copper-constantan thermocouples. The bridge was initially balanced to a null at room temperature. As temperature increases through the Curie point, the sample undergoes a magnetic transition which causes an appreciable change in the sample coil inductance. Thus an abrupt change in the lock-in amplifier output would be observed.

F. Electrical Resistance Measurements

Due to the extreme brittleness of the alloys, cutting of a resistivity sample was rather difficult. Two techniques were employed. Samples were first cut into rectangular rods by a mechanical wire saw with tungsten carbide abrasive, and then cleaned in an ultrasonic vibrator. The desired dimensions of the sample were successfully obtained, but more cracks were introduced by this technique which produced random discontinuities in the resistance vs. temperature curves. A wire spark cutter was then used to cut the ingots into somewhat irregularly shaped rods. This cutting technique, however, introduces very little strain to the sample. In fact, this machine was especially designed to cut materials for the study of dislocations. In spite of the fact that the absolute resistivity of these alloys cannot be obtained due to the difficulty in accurate dimension measurements, relative resistances as functions of temperature ($4.2^{\circ}K - 300^{\circ}K$) were successfully measured.

The resistance was measured by the standard four-point method. This essentially consists of measuring the current flowing through the specimen and the potential difference across the sample. Temperature was measured from 77°K to 300°K using copper constantan thermocouples, and from 4.2°K to 77°K using a calibrated germanium crystal. The experimental uncertainties of resistance and temperature were estimated at about ±1% and ±0.1°K, respectively.

III. BRIEF REVIEW OF RELEVANT THEORIES

A. Mössbauer Effect

1. General Discussion

The Mössbauer effect is a phenomenon of recoilless nuclear gamma ray resonance in solids. In this recoil-free emission, the linewidth ΔE of the γ ray in the ideal case is determined by the lifetime τ of the excited state. If $\tau \simeq 10^{-7}$sec, it follows from the uncertainty principle that $\Delta E \simeq \hbar/\tau \simeq 5\times10^{-9}$eV . The ultimate resolving power for a 14.4 keV γ ray source is then $\Delta\nu/\nu = \Delta E/E \simeq 10^{-12}$, where ν is the frequency of the γ photon. This extremely high energy-resolution clearly indicates that Mössbauer effect is capable of resolving the hyperfine (hf) splittings in solids which are very small energy differences ($\sim 10^{-8}$eV) arising from the interaction of nuclear quadrupole and magnetic moments with the surrounding electric charge and magnetic spin distributions. It is, therefore, a highly useful technique in the field of solid state physics.

Out of a great number of Mössbauer isotopes, Fe^{57} has been most widely used due to its low γ energy (14.4 keV), relatively long lifetime of the excited state and long lifetime of Co^{57} (270 days). This, in particular, is owing to the fact that iron, possessing 2.14% of Fe^{57}, is a common constituent of magnetic materials. The decay scheme of Co^{57} is shown in Fig. 3.

2. Recoilless Probability

Recoilless probability f is defined as the fraction of zero-phonon transitions in a system in which the only other possibility is

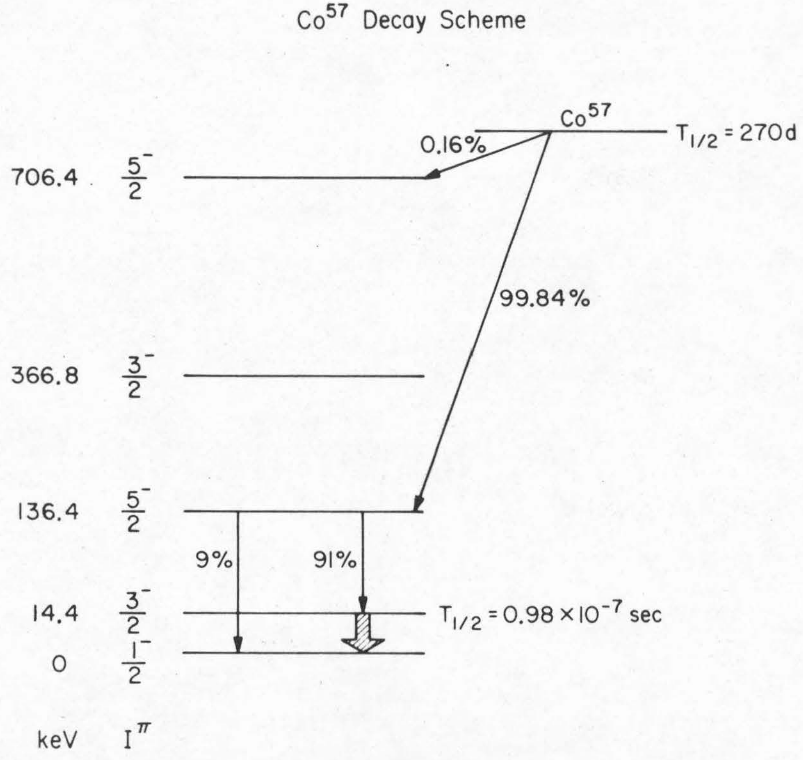

Fig. 3. Decay scheme of Co^{57}. The Mössbauer transition is indicated by the dashed arrow.

one-phonon transitions where a phonon of energy $\hbar\omega$ is excited where ω is frequency of the γ wave. The recoil energy E_r or the average energy transferred to the lattice is then $\hbar\omega(1-f)$, that is,

$$\hbar\omega(1-f) = E_r \quad . \tag{1}$$

Since $E_r = \hbar^2 k^2/2m$, and $\hbar\omega = 2m\omega^2 <u^2>$ for an oscillating nucleus, where k is the gamma wave vector and $<u^2>$ is the mean square displacement of the nucleus, Eq. (1) becomes

$$f = 1 - \frac{E_r}{\hbar\omega} = 1 - k^2 <u^2>$$

$$\cong \exp(-k^2 <u^2>) \tag{2}$$

According to the Debye approximation$^{(28)}$

$$<u^2> = \frac{3\hbar}{M\omega_{max}} \int_0^{\omega_{max}} \left[\frac{1}{2} + \frac{1}{\exp(\hbar\omega/k_BT) - 1}\right] \omega\, d\omega \quad , \tag{3}$$

where M is the mass of crystal and $\omega_{max} = k_B\theta_D/\hbar$ where θ_D is the Debye temperature. After integrating the first term, Eq. (3) becomes

$$<u^2> = \frac{3\hbar^2}{4Mk_B\theta_D} \left[1 + 4\frac{T^2}{\theta_D^2} \int_0^{\theta_D/T} \frac{z\,dz}{e^z - 1}\right] \quad . \tag{4}$$

The integral in Eq. (4) approaches $\pi^2/6$ in the limit $T << \theta_D$, and since

$$E_r = \frac{E^2}{2Mc^2} \quad \text{and} \quad k = \frac{E}{\hbar c} \quad , \tag{5}$$

it follows from Eqs. (2), (4) and (5) that for $T << \theta_D$

$$f = \exp\left[-\frac{E_r}{k_B\theta_D}\left(\frac{3}{2} + \frac{\pi^2T^2}{\theta_D^2}\right)\right] \quad . \tag{6}$$

It is clear from Eq. (6) that at low temperatures the Mössbauer absorption probability is considerably large for most Fe-compounds ($E_r \simeq 2 \times 10^{-3}$eV). However, as temperature increases, the recoil-free fraction decreases exponentially.

3. Electrostatic Hyperfine Interactions

The energy of a nuclear charge distribution $\rho(\overline{x})$ in the electrostatic potential $\Phi(\overline{x})$ produced by electrons of the parent atom as well as the surrounding charges can be written(29) as

$$E_e = \int \rho(\overline{x})\, \Phi(\overline{x})\, d^3x \quad . \tag{7}$$

Since the potential Φ is reasonably slowly varying over the region where $\rho(\overline{x})$ is non-negligible, $\Phi(\overline{x})$ may be expanded in a Taylor's series around $\overline{x} = 0$, and Eq. (7) becomes

$$E_e = \int \rho(\overline{x})\left(\Phi(0) + \sum_{i=1}^{3} \Phi_i x_i + \frac{1}{2}\sum_{i=1}^{3}\sum_{j=1}^{3} \Phi_{ij}x_ix_j + \cdots\right)d^3x \tag{8}$$

where

$$\Phi_i = \left(\frac{\partial\Phi}{\partial x_i}\right)_{\overline{x}=0}$$

$$\Phi_{ij} = \left(\frac{\partial^2\Phi}{\partial x_i\partial x_j}\right)_{\overline{x}=0} \quad .$$

Since the electric field gradient Φ_{ij} , a symmetric matrix, may be diagonalized in choosing its principal axes, Eq. (8) then takes the form

$$E_e = Ze\,\Phi(0) + \sum_{i=1}^{3} \Phi_i \int \rho(\bar{x})\, x_i\, d^3x + \frac{1}{2} \sum_{i=1}^{3} \Phi_{ii} \int \rho(\bar{x})\, x_i^2\, d^3x + \cdots \tag{9}$$

where the fact $\int \rho(\bar{x})\, d^3x = Ze$ is used in obtaining the first term.

As far as Mössbauer transitions are concerned, the first term in Eq. (9) is not interesting for it does not contribute a net displacement in the transition energy, and neither is the second term, since the electric dipole moment of the nucleus is zero due to its parity. Furthermore, it has been shown by Wegener$^{(30)}$ that all higher order terms above the third are also zero. Rearranging the third term of Eq. (9), one then obtains

$$E_e = \frac{1}{6} \sum_{i=1}^{3} \Phi_{ii} \int \rho(\bar{x})\, r^2 d^3x + \frac{1}{6} \sum_{i=1}^{3} \Phi_{ii} \int \rho(\bar{x})(3x_i^2 - r^2)\, d^3x\ . \tag{10}$$

This immediately leads to the contribution of the isomer shift and quadrupole splitting.

a. Isomer shift

Applying Laplace's equation, one obtains

$$\sum_{i=1}^{3} \Phi_{ii} \equiv (\nabla^2\Phi)_{\bar{x}=0} = -4\pi\rho(0) = 4\pi e|\Psi(0)|^2 \tag{11}$$

where $|\Psi(0)|^2$ is the total electronic density at the nucleus. Also, if a uniform nuclear charge density is assumed throughout a sphere of nuclear radius R, i.e., $\rho(\bar{x}) = Ze / \frac{4\pi}{3} R^3$ for $|\bar{x}| \leq R$, then

$$\int \rho(\bar{x})\ r^2 d^3x = \frac{3}{5} ZeR^2 \quad . \tag{12}$$

From Eqs. (11) and (12), the first term in Eq. (10) becomes

$$E_{IS} = \frac{2\pi\ Ze^2}{5} R^2 |\Psi(0)|^2 \tag{13}$$

The net shift ΔE_{IS} of the energy levels of the excited (e) and ground (g) states is therefore

$$\Delta E_{IS} = \frac{2\pi\ Ze^2}{5} [R_e^2 - R_g^2]\ |\Psi(0)|^2 \quad . \tag{14}$$

Hence the isomer shift δ, which is observed as the net shift of the Mössbauer absorption line between absorber and source, is

$$\delta = \frac{2\pi\ Ze^2}{5} [R_e^2 - R_g^2][|\Psi_{abs}(0)|^2 - |\Psi_s(0)|^2] \tag{15}$$

Conventionally one writes

$$R_e^2 - R_g^2 = \Delta(R^2)\Big|_{R_g}^{R_e} = 2R^2\left(\frac{\Delta R}{R}\right) \tag{16}$$

where $\Delta R = R_e - R_g$, so that

$$\delta = \frac{4\pi\ Ze^2}{5} R^2\left(\frac{\Delta R}{R}\right) \left(|\Psi_{abs}(0)|^2 - |\Psi_s(0)|^2\right) \quad . \tag{17}$$

It is clear that the first part of this equation (everything outside the brackets) is basically a nuclear parameter, while the second is atomic which is affected by the valence state of the atom.

For Fe^{57}, $R_e < R_g$ or $\Delta R/R < 0$ (28), and, therefore, increasing charge density at the nucleus of absorbers due to s electrons corresponds to decreasing the isomer shift. On the other hand, adding d electrons decreases charge density at the nucleus because of shielding effect, and in turn results in a larger, positive isomer shift.

b. Quadrupole splitting

In the case of quadrupole splitting, the second term in Eq. (10),

$$E_Q = \frac{1}{6} \sum_{i=1}^{3} \Phi_{ii} \int \rho(\bar{x})(3x_i^2 - r^2)\, d^3x \tag{18}$$

may now be considered. Since only s electrons can be present at the nucleus and these electrons make up a spherically symmetric potential, i.e., $\Phi_{xx} = \Phi_{yy} = \Phi_{zz}$, it follows that

$$E_Q = \frac{1}{6} \Phi_{zz} \int \rho(\bar{x}) \left[3 \left(\sum_{i=1}^{3} x_i^2 \right) - 3r^2 \right] d^3x = 0 \quad . \tag{19}$$

It is, therefore, clear that s electrons do not contribute to the quadrupole interaction. However, for those that do contribute to the electric field gradient (efg),

$$\Phi_{xx} + \Phi_{yy} + \Phi_{zz} = 4\pi e |\Psi(0)|^2 = 0 \quad . \tag{20}$$

For cubic symmetry, $\Phi_{xx} = \Phi_{yy} = \Phi_{zz} = 0$ (from Eq. (20)), and consequently quadrupole splitting does not exist.

If axial symmetry is assumed, or

$$\Phi_{xx} = \Phi_{yy} = -\frac{1}{2} \Phi_{zz} , \tag{21}$$

Eq. (18) then becomes

$$E_Q = \frac{1}{4}\,\Phi_{zz} \int \rho(\bar{x})\,(3z^2 - r^2)\, d^3x \qquad (22)$$

The quantum mechanical expression for Eq. (22) follows from the fact that$^{(30)}$

$$\int \rho(\bar{x})\,(3z^2 - r^2)\, d^3x = eQ\,\frac{3m^2 - I(I+1)}{3I^2 - I(I+1)} \qquad (23)$$

where

$$Q = \frac{1}{e} \int \Psi_{II}^* \left[\sum_{i=1}^{A} r_i^2 (3\cos^2\theta_i - 1) \right] \Psi_{II}\, d\bar{r}_1\, d\bar{r}_2 \cdots d\bar{r}_A$$

is the expression for the quadrupole moment of the nucleus of A nucleons and spin I, and m is the quantum number for I_z . Ψ_{II} is the wave function corresponding to the maximum projection of spin I on the z axis. Hence, for the quadrupole splitting in an axially symmetric efg,

$$E_Q(m) = \frac{1}{4}\, e^2 qQ\, \frac{3m^2 - I(I+1)}{3I^2 - I(I+1)} \qquad (24)$$

where $eq = \Phi_{zz}$ is the conventional definition for efg.

For Fe^{57} ($I_e = 3/2$), two energy levels are given by Eq. (24), i.e.,

$$E_Q(\pm\, 3/2) = \frac{1}{4}\, e^2\, qQ$$

$$E_Q(\pm\, 1/2) = -\frac{1}{4}\, e^2 qQ \quad .$$

In Fig. 4a is shown the resulting Mössbauer spectrum (for $q > 0$) with two peaks separated by $\left|\frac{1}{2}\, e^2 qQ\right|$.

However, if nonaxial symmetry is assumed, the quadrupole Hamiltonian is then

$$\hat{H}_Q = \frac{e^2qQ}{4I(2I-1)}\left[3I_z^2 - I(I+1) + \frac{\eta}{2}(I_+^2 + I_-^2)\right] \tag{25}$$

where $\eta = \frac{\Phi_{xx} - \Phi_{yy}}{\Phi_{zz}}$ is the asymmetry parameter, $I_\pm = I_x \pm iI_y$ are the raising and lowering operators, and the components are usually chosen so that $|\Phi_{zz}| \geq |\Phi_{xx}| \geq |\Phi_{yy}|$, making $0 \leq \eta \leq 1$. Equation (25) has the eigenvalues

$$E_Q = \frac{1}{4}e^2qQ\,\frac{3m^2 - I(I+1)}{I(2I-1)}\left(1 + \frac{\eta^2}{3}\right)^{1/2}, \quad m = I, I-1, \cdots, -I\ . \tag{26}$$

For Fe^{57}, again two energy levels result, and the splitting, however, is $\left|\frac{1}{2}e^2qQ\right|\left(1 + \frac{\eta^2}{3}\right)^{1/2}$.

4. Magnetic Hyperfine Interaction

a. Pure magnetic coupling

The magnetic hyperfine splitting arises from the interaction of the nuclear magnetic dipole moment $\overline{\mu}$ with the magnetic field $\overline{H}$ at the nucleus which results from its own electrons. The Hamiltonian of the interaction is

$$\begin{aligned}\hat{H}_M &= -\overline{\mu}\cdot\overline{H} \\ &= -g\mu_n\overline{I}\cdot\overline{H}\ ,\end{aligned} \tag{27}$$

where g is the gyromagnetic ratio and μ_n the nuclear magneton. The eigenvalues of $\hat{H}_M$ are

$$E_M(m) = -\mu Hm/I = -g\mu_n Hm \quad , \quad m = I, I-1, \cdots, -I \tag{28}$$

where m is the quantum number corresponding to I_z . A magnetic hf structure may be obtained by applying Eq. (28) to Fe^{57} (Fig. 4b and Fig. 2). It should be noted that as mentioned earlier quadrupole splitting does not exist in cubic systems such as iron.

b. Combined magnetic and electric interactions

Both magnetic hyperfine and electric quadrupole interactions in general exist in magnetic solids if the symmetry of either the crystal or magnetic(31,32) lattice is lower than cubic. The Hamiltonian of such a combined interaction is the sum of H_Q and H_M described earlier, and they take the form of Eqs. (25) and (27) provided that the principal axis of the axially symmetric efg is parallel to the magnetic field. For the most general case where each is expressed in terms of its own coordinate system, there is no closed form solution available then. However, a closed form solution does exist in the case of axially symmetric efg with symmetry axis at an angle θ with respect to the direction of the magnetic field(28), and it is

$$E(m) = -g\mu_n Hm + (-)^{|m|+\frac{1}{2}} \frac{eqQ}{4} \cdot \frac{3\cos^2\theta - 1}{2} \tag{29}$$

for $e^2qQ/\mu H << 1$.

For $\theta = 0$, this reduces to the special case where the principal axis of the axially symmetric efg is parallel to $\overline{H}$ (see Fig. 4c). In fact this is formally identical to Eq. (29) if in the latter $Q(3\cos^2\theta - 1)/2$ is replaced by Q' .

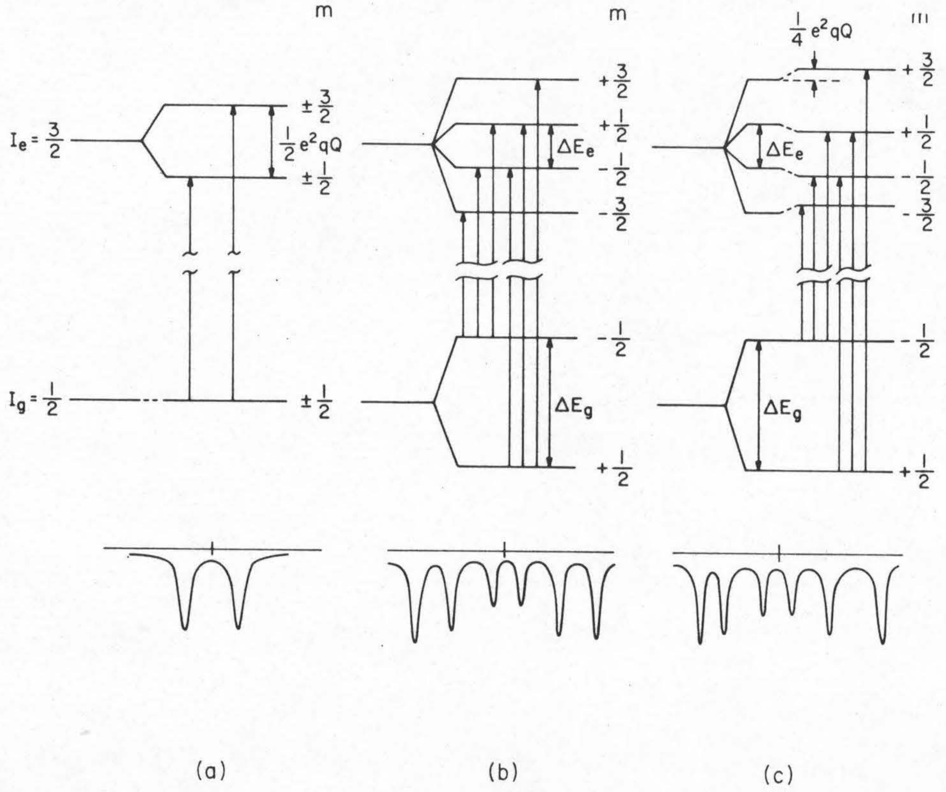

Fig. 4. Nuclear energy levels of Fe^{57} and resulting Mössbauer spectra: (a) Electric quadrupole interaction. (b) Magnetic hyperfine interaction. (c) Combined magnetic and electric quadrupole interaction with the principal axis of electric field gradient parallel to H_{hf}.

5. Contributions to the Magnetic Hyperfine Field

Due to interactions with the surrounding ions, electronic spins fluctuate between the up and down states. When the fluctuations are fast compared to the Larmer frequency of the nuclear spin, the hyperfine field seen by the nucleus averages to zero in the absence of an external field. This is generally the case for the paramagnets. However, when the electronic relaxation rates are comparable to or smaller than the nuclear Larmer frequency, a finite hyperfine field will then be observed. This magnetic hyperfine field is, in fact, due to several mechanisms. According to Marshall(33,34),

$$\overline{H} = \overline{H}_i + \overline{H}_d + \overline{H}_o + \overline{H}_s \quad , \tag{30}$$

where each term will be discussed individually as follows:

a. Internal field

This contribution can be written as

$$\overline{H}_i = \overline{H}_{ext} - D\overline{M} + \frac{4\pi}{3}\overline{M}' + \overline{H}' \tag{31}$$

where D is the demagnetizing factor, $\overline{M}$ the magnetization, and $\overline{M}'$ the domain magnetization ($M' = M$ in a paramagnet), and $\overline{H}'$ is the correction term to the Lorentz field $\frac{4\pi}{3}\overline{M}'$ for non-cubic symmetry. When $\overline{H}_{ext} = 0$, $\overline{H}_i$ is usually very small, of the order of several kilogauss.

b. Dipolar field

Contributions from $\overline{H}_d$ in Eq. (30) arise from the interaction of the atomic spin with electronic spin dipole produced by the surrounding ions. This term can be expressed as follows:

$$\overline{H}_d = -2\mu_B[\frac{\overline{S}}{r^3} - \frac{3\overline{r}(\overline{r}\cdot\overline{S})}{r^5}] \quad . \tag{32}$$

Conbributions from $\overline{H}_d$ are relatively small ($\sim$ 10kOe) (35), and vanish in cubic systems due to zero spin-orbit coupling.

c. Orbital current field

The orbital part of the electronic angular momentum gives rise to a field $\overline{H}_o$

$$\overline{H}_o = -2\mu_B \frac{\overline{L}}{r^3} \quad . \tag{33}$$

In trivalent iron, this contribution is zero since $\overline{L} = 0$, while in metallic Fe where the angular momentum is partially quenched $\overline{H}_o$ is estimated to be +70kOe . (28) In the case of rare earths, however, this term becomes dominant, of the order of 10^3-10^4kOe . (35)

d. Fermi contact term

The last term in Eq. (30), known as the Fermi contact term (35, 36), is given as

$$H_s = -\frac{8\pi\mu_B}{3} \sum_s \left(|\Psi_{s\uparrow}(0)|^2 - |\Psi_{s\downarrow}(0)|^2\right) \quad . \tag{34}$$

This field results from the spin density present at the nucleus, in other words, from the polarization of only the core s and 4s electrons by the 3d electron spins. In describing this mechanism, the sign convention is adopted such that the spins are said to be positive if they are antiparallel to magnetization and the magnetic hyperfine field positive when directed parallel to the magnetization.

According to the Pauli principle, electrons of antiparallel spins are closer to each other than those of parallel spins. However, when the Coulomb interaction is "switched on", the exchange coupling between the 3d and core s electrons is stronger for electrons of antiparallel spin than for parallel spin. In effect, the electron with antiparallel spin to the 3d spins experiences a greater repulsion by the 3d electrons. Consequenty , the inner shell s electrons produce a negative spin density at the nucleus which gives rise to a negative magnetic field. The opposite is true, on the other hand, of the outer shell s electrons. The net magnetic field then depends on whether the inner or the outer s electrons produce a greater contribution. For metallic Fe, the inner electrons predominate, so that a contribution of -(400-500)kOe results from the polarization of the core electrons.

B. The Molecular Field Theory (MFT)(37,38,39)

It is a well known fact that magnetism to some extent has been successfully explained by the exchange interaction which tends to orient the magnetic moments of the atoms in an ordered pattern. This interaction, approximated by a concept known as the molecular field, is opposed by the effect of thermal agitation to preserve a random orientation of magnetic moments. Furthermore, the molecular field H_e is assumed proportional to the magnetization M ,

$$\overline{H}_e = \xi \, \overline{M} \tag{35}$$

where ξ is a constant, independent of temperature. As can be seen from Eq. (35), each spin sees the average magnetic moment due to all the other spins. This assumption was first introduced by P. Weiss(40). It should be noted, however, that Weiss' theory was developed several years before the Bohr theory of the atom and Von Laue's discovery of x-ray diffraction, so that a reproduction of Weiss' treatment should be carried out with a more realistic modification of the quantum theory and the discrete character of the crystal structure. Moreover, since presently we are only interested in the transition elements, the orbital angular momentum is therefore assumed to be quenched ($\overline{L} = 0$) throughout the following treatment.

1. MFT of Ferromagnetism

According to the Heisenberg model, the Hamiltonian of the exchange interaction for a single atom i is given as

$$\hat{H} = -2J\, \overline{S}_i \cdot \sum_{j=1}^{p} \overline{S}_j \tag{36}$$

where the sum is over the p nearest neighbors of the i^{th} atom and the exchange integral J is related to the overlap of the charge distributions of the atoms i and j.

The interactions in Eq. (36) can be replaced by a molecular field H_e so that the Hamiltonian has the form

$$\hat{H} = -g\mu_B\, \overline{S}_i \cdot \overline{H}_e \tag{37}$$

where g is the g-factor and μ_B the Bohr magneton. Comparing Eqs. (36) and (37), one obtains

$$\overline{H}_e = \frac{2J}{g\mu_B} \sum_{j=1}^{p} \overline{S}_j$$

$$= \frac{2Jp}{g\mu_B} \langle \overline{S} \rangle \tag{38}$$

where $\langle \overline{S} \rangle$ is the average value of $\overline{S}_j$. In a simple lattice where all magnetic atoms are identical and crystallographically equivalent, the total magnetic moment $\overline{M}$ can be written in terms of $\langle \overline{S} \rangle$ as

$$\overline{M} = N\, g\, \mu_B \langle \overline{S} \rangle \tag{39}$$

so that

$$\overline{H}_e = \frac{2pJ}{Ng^2\mu_B^2} \overline{M} \tag{40}$$

where N is the number of atoms per gram of sample. This is the molecular field equation with the Weiss coefficient ξ in Eq. (35) given by

$$\xi = \frac{2pJ}{Ng^2\mu_B^2} \quad . \tag{41}$$

As the effect of an applied field $\overline{H}_o$ is considered, the Hamiltonian in Eq. (37) becomes

$$\hat{H} = -g\mu_B\, S_z H \tag{42}$$

where

$$\overline{H} = \overline{H}_o + \overline{H}_e \tag{43}$$

is the total field acting on the ith atom, and, without loss of generality, H_o is chosen to lie in the same direction as M and H_e , say, in the z-axis. The energy eigenvalues of $\hat{H}$ in Eq. (42) are

$$E(m) = -g\mu_B Hm \ , \quad m = S, S-1, \cdots, -S \ . \tag{44}$$

The partition function is then

$$Z_s = \sum_{m=-S}^{S} \exp(\frac{mx}{S}) \tag{45}$$

where

$$x = \frac{g\mu_B SH}{k_B T} \tag{46}$$

is a ratio of magnetic and thermal energies. Therefore, the magnetization M can be given in terms of the partition function as

$$\begin{aligned} M &= Ng\mu_B < S_z > \\ &= Ng\mu_B \frac{Tr[S_z \exp(\hat{H}/k_B T)]}{Z_s(x)} \\ &= \frac{Ng\mu_B \sum_{m=-S}^{S} m \exp(mx/S)}{\sum_{m=-S}^{S} \exp(mx/S)} \ . \end{aligned} \tag{47}$$

This can then be reduced to

$$M = Ng\mu_B SB_s(x) \tag{48}$$

where the Brillouin function $B_s(x)$ is defined as(41)

$$B_s(x) = \frac{2S+1}{2S} \coth(\frac{2S+1}{2S} x) - \frac{1}{2S} \coth \frac{x}{2S} \ . \tag{49}$$

For large x ,

$$\coth y = 1 + 2e^{-2y} + \cdots \ , \tag{50}$$

and Eq. (48) becomes

$$M = Ng\mu_B S[1 - \frac{1}{S}\exp(-g\mu_B H/k_B T)] \quad , \quad (x \text{ large}) \quad . \tag{51}$$

However, for small x, it can be shown that the Brillouin function in Eq. (49) reduces to

$$B_s(x) = \frac{S+1}{3S}\,x \quad , \tag{52}$$

and therefore from Eq. (48)

$$M = \frac{Ng^2\mu_B^2\,S(S+1)}{3k_B T}(H_o + H_e) \quad . \tag{53}$$

Substituting Eq. (40) into Eq. (53), one obtains the susceptibility

$$\chi \equiv \frac{M}{H_o} = \frac{Ng^2\mu_B^2\,S(S+1)/3k_B}{T - \frac{2pJ\,S(S+1)}{3k_B}} \quad . \tag{54}$$

Comparison with the Curie-Weiss law $\chi = \frac{C}{T - T_c}$ gives the Curie temperature

$$T_c = \frac{2pJ\,S(S+1)}{3k_B} \quad . \tag{55}$$

It is convenient at this stage to define the reduced spontaneous magnetization σ as the ratio of magnetization to its maximum value $M_o = Ng\mu_B S$, that is, from Eqs. (46) and (48)

$$\sigma = B_s\left(\frac{g\mu_B\,S\,H}{k_B T}\right) \tag{56}$$

It is easy to see that $\sigma \to 1$ as $T \to 0$ (from Eq. (51)). Substitution of Eqs. (40) and (55) into Eq. (56) leads to

$$\sigma = B_S\left(\frac{3}{S+1}\,\sigma\,\frac{T_c}{T}\right) \quad \text{for} \quad H_o = 0 \quad . \tag{57}$$

According to Eq. (50) at low temperatures $(\sigma \rightarrow 1)$, Eq. (57) becomes

$$\sigma = 1 - \frac{1}{S}\exp\left(-\frac{3}{S+1}\cdot\frac{T_c}{T}\right)$$

$$\cong 1 - \frac{1}{S}\left[1 - \frac{3}{S+1}\,\frac{T_c}{T}\right] \tag{58}$$

At $T = T_o$, this can be written as

$$\sigma = A_o + A_1 T_c \tag{59}$$

where

$$A_o = \frac{S-1}{S} \tag{60}$$

and where

$$A_1 = \frac{3}{S(S+1)\;T_o} \tag{61}$$

is a positive constant. It is, therefore, clear from Eq. (59) that an increase in σ corresponds to a higher Curie temperature.

2. MFT of Antiferromagnetism

In the present discussion, a simple magnetic structure will be considered, where the lattice of magnetic atoms can be subdivided into two equivalent, interpenetrating sublattices, A and B, such that A atoms have only B atoms as nearest neighbors and vice versa. Then if a negative exchange interaction $(J < 0)$ takes place between nearest neighbors, the sublattices A and B will be spontaneously magnetized antiparallelly. This is called the two-sublattice model.

Clearly two molecular fields $\overline{H}_{eA}$ and $\overline{H}_{eB}$ must now be considered to act on the sublattices A and B , respectively. Since A atoms interact only with B atoms and vice versa, equations similar to Eqs. (35) and (40) can be written as follows:

$$\overline{H}_{eA} = \frac{4pJ}{Ng^2\mu_B^2}\,\overline{M}_B = 2\xi\,\overline{M}_B \tag{62}$$

$$\overline{H}_{eB} = \frac{4pJ}{Ng^2\mu_B^2}\,\overline{M}_A = 2\xi\overline{M}_A \tag{63}$$

where $J < 0$ in both equations.

The total fields acting on A and B atoms are then

$$\overline{H}_A = \overline{H}_o + 2\xi\overline{M}_B \tag{64}$$

and

$$\overline{H}_B = \overline{H}_o + 2\xi\overline{M}_A \tag{65}$$

Similar calculation of Eqs. (42) to (56) leads to the reduced spontaneous magnetizations

$$\sigma_A = \frac{M_A}{\frac{1}{2}Ng\mu_B S} = B_s\left(\frac{g\mu_B S\,H_A}{k_B T}\right) \tag{66}$$

$$\sigma_B = \frac{M_B}{\frac{1}{2}Ng\mu_B S} = B_s\left(\frac{g\mu_B A\,H_B}{k_B T}\right)\ . \tag{67}$$

In order to determine the transition temperature, Eqs. (66) and (67) are solved simultaneously for the magnetizations in the high temperature region where

$$B_S(x) = \frac{S+1}{3S} x \quad . \tag{52}$$

One finds the susceptibility

$$\chi = \frac{M_A + M_B}{H_o} = \frac{C}{T - C\xi} \tag{68}$$

where

$$C\xi = \frac{2pJ\ S(S+1)}{3k_B} = T_c \tag{69}$$

is negative, since $J < 0$.

As $H_o = 0$, M_A and M_B in Eqs. (66) and (67) have non-zero solutions only when

$$T_c = C\xi < 0 \quad \text{and} \quad M_A = M_B \tag{70}$$

or

$$T_N = -C\xi > 0 \quad \text{and} \quad M_A = -M_B \quad . \tag{71}$$

It is easy to see that Eq. (71) is the situation for antiferromagnetism.

Below the Néel temperature as $H_o = 0$, the reduced spontaneous magnetizations can be obtained in the same procedure as in the ferromagnetic case,

$$\sigma_A = B_s \left(\frac{-3S}{S+1} \cdot \frac{\sigma_B T_N}{T}\right) \tag{72}$$

and

$$\sigma_B = B_s \left(\frac{-3S}{S+1} \cdot \frac{\sigma_A T_N}{T}\right) \tag{73}$$

The solution of Eqs. (72) and (73) is easily found to be

$$\sigma_s = B_s \left(\frac{3S}{S+1} \cdot \frac{\sigma_s T_N}{T}\right) \tag{74}$$

where $\sigma_s = \sigma_A = -\sigma_B$. Since $\sigma_s \to 1$ at low temperatures, Eq. (74) then becomes identical to Eq. (59) with T_c replaced by T_N ,

$$\sigma_s = A_o + A_1 T_N \tag{75}$$

where σ_s is the sublattice reduced spontaneous magnetization, and A_o and $A_1 > 0$ are as defined in Eqs. (60) and (61). It should be noted that an exact relation which holds between σ and T_c holds also between σ_s and T_N .

C. The Bloch Theory of Electrical Resistivity

According to the Matthiessen rule$^{(41)}$ the total electrical resistivity ρ in a reasonably pure metal is due to both residual or impurity resistivity ρ_i and lattice resistivity ρ_L , and can be written as

$$\rho(T) = \rho_i + \rho_L(T) \tag{76}$$

where ρ_i is independent of temperature.

However, in a well-annealed, nominally-pure sample in which scattering contributions from vacancies, dislocations and isotopes are negligible, ρ_i is mainly due to foreign impurity atoms. The residual resistivity ρ_i for low concentration impurities is generally small compared with $\rho_L(T)$ except at low temperatures where ρ_L approaches zero. As temperature increases, ρ_i remains constant while ρ_L rises rapidly owing to the electron-phonon interaction. When an electron interacts with a phonon of frequency ν , an energy $h\nu$ is exchanged. Based on the Debye approximation, the phonon density varies as T^3 at low temperatures. Furthermore, since only lower frequency phonons can be excited at these low temperatures, the corresponding low momenta indicate that the conduction electrons will be scattered through small angles of order T/θ_D where θ_D is the Debye temperature. For small angles, the effect of this scattering on the resistivity depends on the square of the angle T^2/θ_D^2 . Hence at low temperatures the total resistivity $\rho(T)$ can be expressed by $\rho_i + AT^5$ where A is a positive constant.

At temperatures $T >> \theta_D$, the effect of the quantization of the lattice vibrations is less significant since $h\nu$ is much smaller than $k_B\theta_D$, and the classical conditions become dominant. The available phonons, therefore, increase in proportion to temperature. Consequently, the probability of electron scattering is proportional to T . Hence at $T >> \theta_D$, $\rho(T) = \rho_i + BT$ where B is a positive constant.

To express the entire temperature variation of the electrical resistivity in a simple metal, the following equation may be written$^{(41)}$

$$\rho(T) = \rho_i + \frac{k}{\theta_R^2} T \, G(\frac{\theta_R}{T}) \tag{77}$$

where $G(\theta_R/T)$ is the Grüneisen-Bloch equation,

$$G(z) = \frac{4}{z^4} \int_0^z \frac{s^5 ds}{(e^s-1)(1-e^{-s})} \quad , \tag{78}$$

and where θ_R is a temperature characteristic of the solid's lattice resistance in the same way as the Debye temperature θ_D is a characteristic of the lattice specific heat.

When k and θ_R are suitably chosen, Eqs. (77) and (78) are found to represent the experimental temperature variation of the resistivity of a wide selection of metals rather well. The important consequence that follows immediately is that because of its comparative simplicity, the Grüneisen-Bloch equation provides a valuable tool for analyzing the experimental data. It should be pointed out, however, that its success is surprising insofar as the assumption on which it is based might be thought to limit its use to no more than idealized simple metals with Debye phonon spectra and spherical Fermi surfaces. What is more, Umklapp processes were completely neglected(42).

IV. EXPERIMENTAL RESULTS AND DATA ANALYSIS

A. X-Ray Diffraction

1. Crystal Structure of the Alloy System

The $(Fe_{100-x}Mn_x)_5Si_3$ alloys crystallize in the $D8_8$ structure$^{(2)}$. The $D8_8$ or Mn_5Si_3 type structure has 16 atoms per unit cell and has the space group symmetry $P6_3/mcm^{(1,2)}$ in which Me (metal atoms or Fe and Mn in this case) have two crystallographically inequivalent sites. The Me_I atoms in 6(g) site form tetrahedrons with their symmetry axis perpendicular to the basal plane, and the Me_{II} atoms in 4(d) site surrounded by tetrahedrons of Si form linear chains in the direction of the c-axis. A (001)-projection of an Me_5Si_3 unit cell is shown in Fig. 5. The atomic coordinates for the Me_5Si_3 lattice$^{(1)}$ are shown in Table I.

2. Lattice Constants and Their Anomalies

The Debye-Scherrer x-ray diffraction spectra of all alloys $(Fe_{100-x}Mn_x)_5Si_3$ with $x = 0,10,20,\cdots,100$ indeed show a pattern characteristic of a $D8_8$ structure. Determination of the lattice parameters of such a hexagonal crystal structure involves the iteration of the following two equations$^{(23)}$:

$$a = \frac{\lambda}{2\sin\theta}\left[\frac{4}{3}(h^2 + hk + k^2) + \frac{\ell^2}{(c/a)^2}\right]^{1/2} \tag{79}$$

and

$$c = \frac{\lambda}{2\sin\theta}\left[\frac{4}{3}\left(\frac{c}{a}\right)^2 (h^2 + hk + k^2) + \ell^2\right]^{1/2} \tag{80}$$

where $\lambda = 2.29092\text{Å}$ is the wavelength of Cr Kα radiation, and θ is the Bragg angle corresponding to $(hk\ell)$ diffracted line. A computer

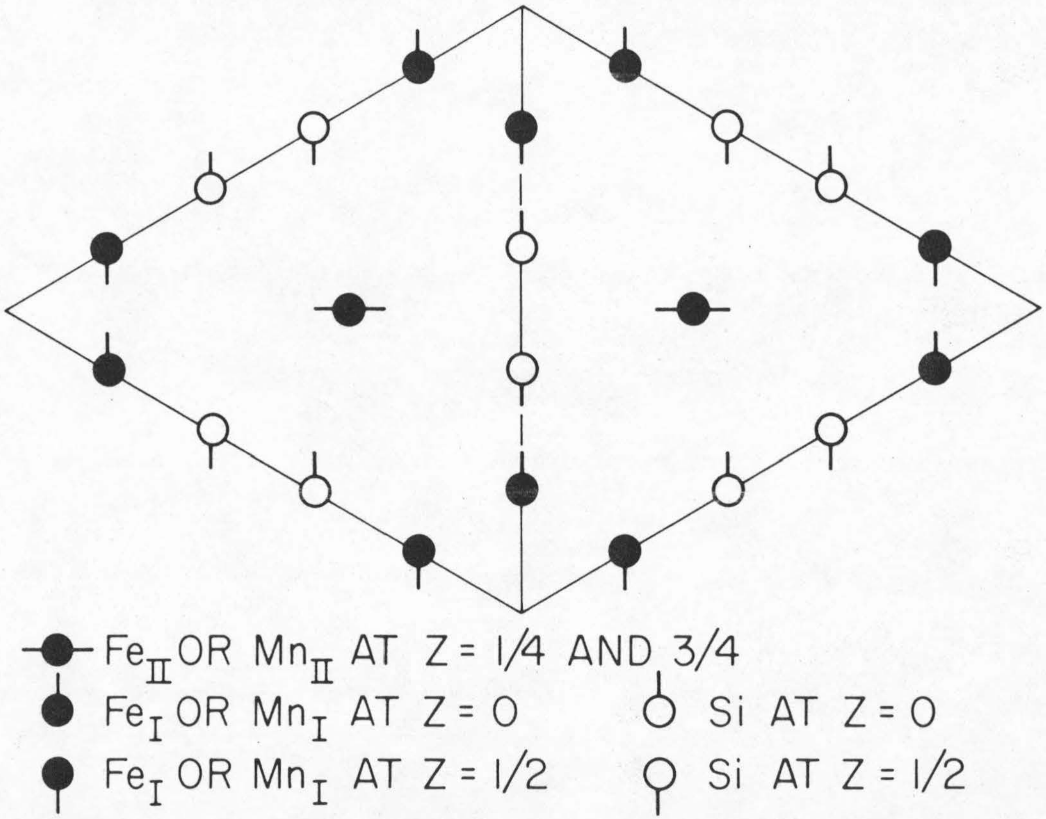

Fig. 5. Structure of Me_5Si_3 projected to the basal plane.

TABLE I

Atomic coordinates* of the Me_5Si_3 lattice

Atom	Coordinates					
6 Me_I in 6(g)	u,u,o	$o,\bar{u},o$	$\bar{u},o,o$	$\bar{u},\bar{u},\frac{1}{2}$	$o,u,\frac{1}{2}$	$u,o,\frac{1}{2}$
4 Me_{II} in 4(d)	$\frac{1}{3},\frac{2}{3},\frac{1}{4}$	$\frac{2}{3},\frac{1}{3},\frac{1}{4}$	$\frac{1}{3},\frac{2}{3},\frac{3}{4}$	$\frac{2}{3},\frac{1}{3},\frac{3}{4}$		
6 Si in 6(g)	v,v,o	$o,\bar{v},o$	$\bar{v},o,o$	$\bar{v},\bar{v},\frac{1}{2}$	$o,v,\frac{1}{2}$	$v,o,\frac{1}{2}$

---

*u = 0.23a and v = 0.60a

program was written first to calculate the (a,c) values for each (hkℓ) line using equations (1) and (2). It then least-squares fits a and c values against the Nelson-Riley function$^{(43)}$ $f_{NR} = \frac{\cos^2\theta}{\sin\theta} + \frac{\cos^2\theta}{\theta}$, and extrapolates them to $\theta = 0$ as the desired lattice parameters, a and c. Figures 6 and 7 show the lattice constants a and c, respectively, of $(Fe_{100-x}Mn_x)_5Si_3$ as functions of alloy composition (empty circles). It is clear that Vegard's law has been violated in both of these curves. Furthermore, Fig. 6 indicates that lattice parameter a increases with Mn concentration at a constant rate until $x = 22.5$ where the rate of increase per Mn concentration slows down by 51.9%; while the slope of lattice parameter c increases even more sharply at $x = 50$ by 112.6% as shown in Fig. 7. These lattice constant results are in good agreement with those reported in Ref. 2, but not at all with those in Ref. 20 which are also plotted as solid points in Figs. 6 and 7.

3. Identification of a Second Phase in the Fe-Rich Alloys

From the Fe-FeSi phase diagram in Fig. 8, the intermetallic compound $Fe_5Si_3(\eta)$ is in fact a high temperature phase, stable only between 825° and 1030°C $^{(22)}$. This is unlike the case for Mn_5Si_3 which is a congruently melted intermetallic compound$^{(22)}$. A closer examination of the x-ray diffraction spectrum of the Fe_5Si_3 compound indicates definite broadening of certain low angle lines, in particular, the (211) line shown with an arrow in Fig. 9b compared with the corresponding line in the Mn_5Si_3 diffraction pattern in Fig. 9e. In Fig. 9c, the (211) line on the $(Fe_{90}Mn_{10})_5Si_3$

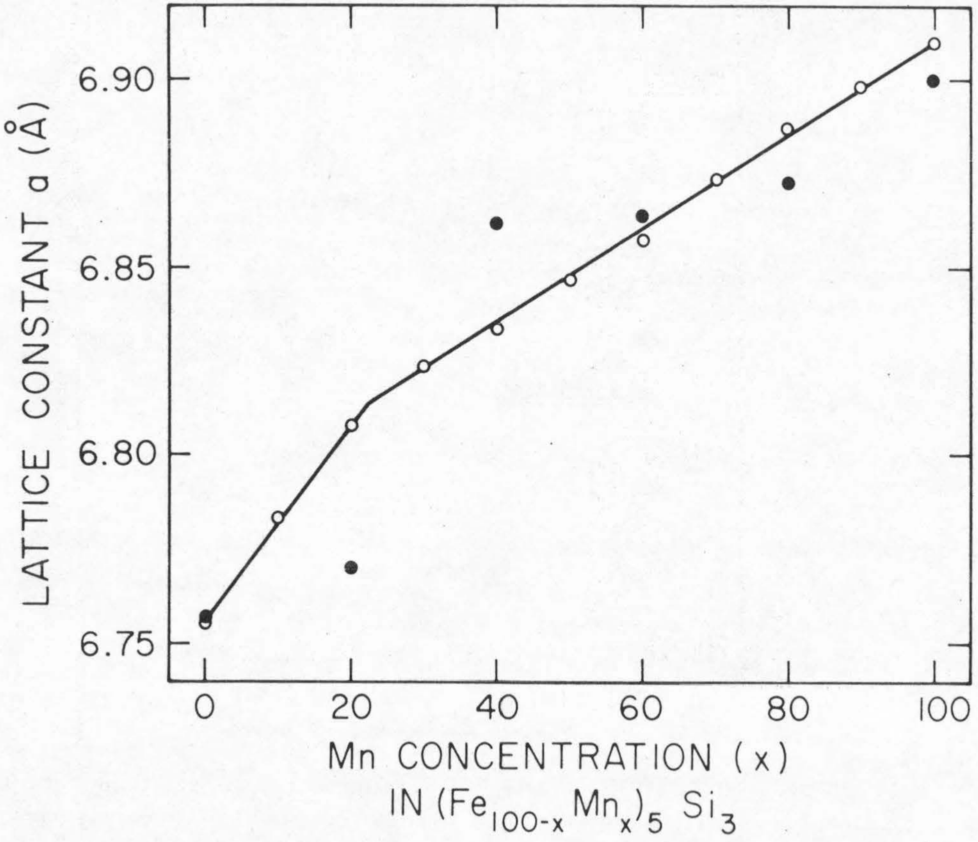

Fig. 6. Lattice constant a of the $(Fe_{100-x}Mn_x)_5Si_3$ alloys. Filled circles (●) are data reported in Ref. 20.

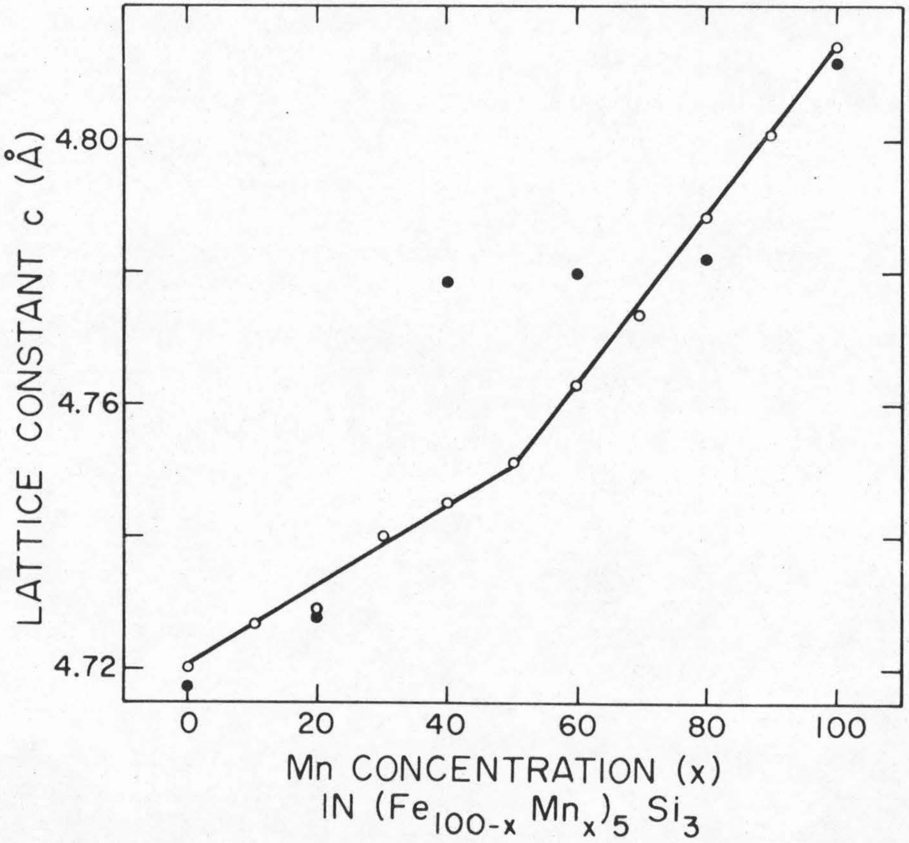

Fig. 7. Lattice constant c of the $(Fe_{100-x}Mn_x)_5Si_3$ alloys. Filled circles (●) are data reported in Ref.[20].

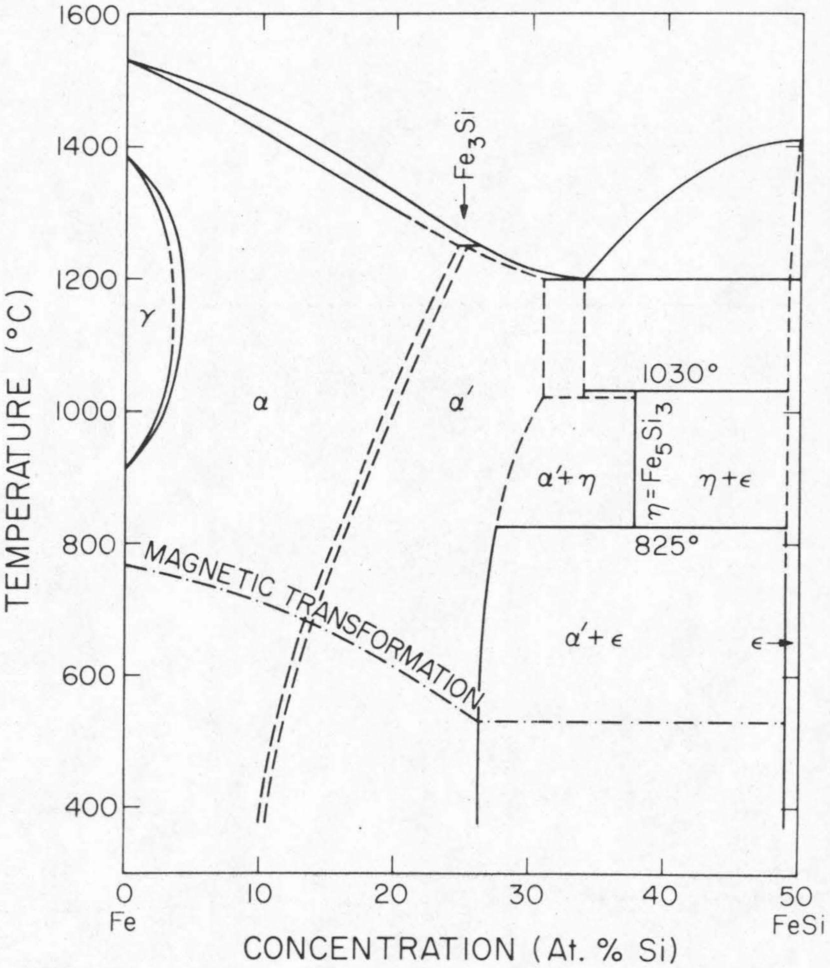

Fig. 8. Partial phase diagram of the Fe-Si system.

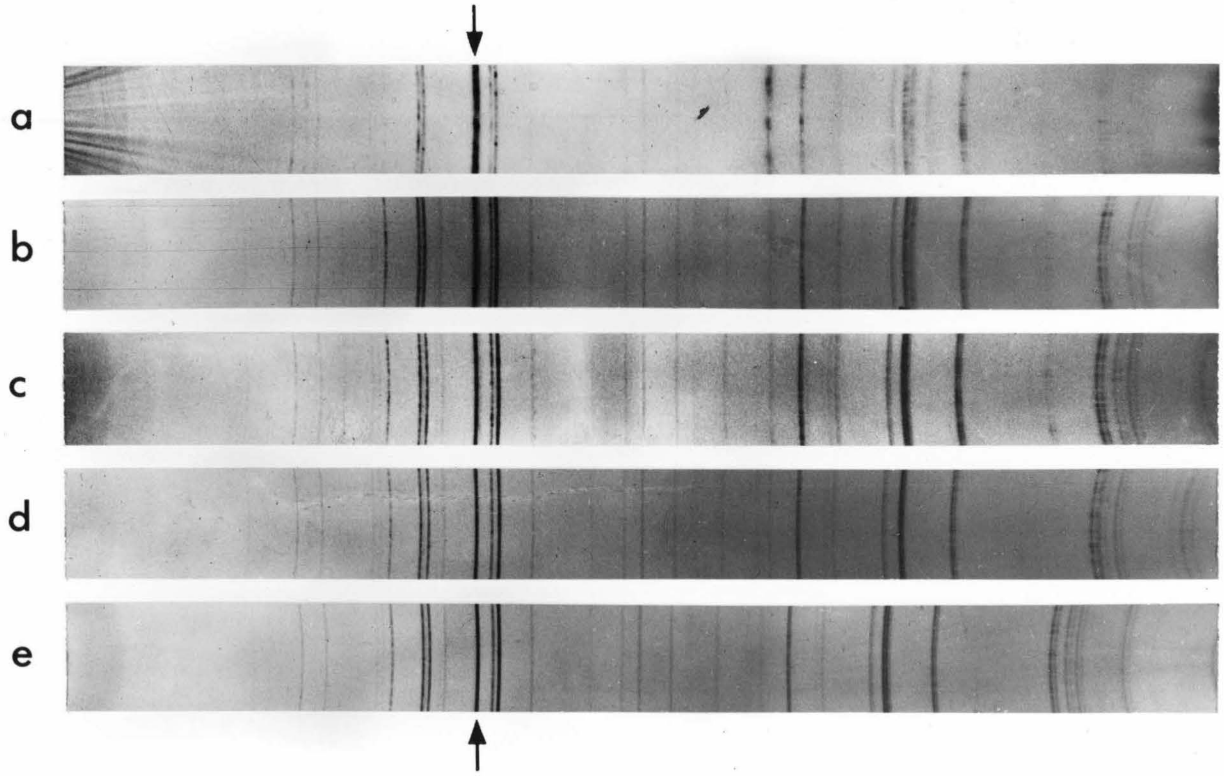

Fig. 9. Debye-Scherrer diffraction patterns of (a) $(\eta + \alpha')$ - $Fe_{67}Si_{33}$, (b) η - Fe_5Si_3, (c) $(Fe_{90}Mn_{10})_5Si_3$, (d) $(Fe_{70}Mn_{30})_5Si_3$, and (e) Mn_5Si_3.

diffraction pattern exhibits a weaker but still noticeable broadening. The (211) line broadening completely disappears in the $(Fe_{70}Mn_{30})_5Si_3$ spectrum (Fig. 9d). This suggests that a second phase may exist even in the quenched Fe-rich alloys. Figure 8 indicates that this second phase might be either the α' or ε phase or a combination of both α' and ε.

In order to identify the existing second phase, alloys of $Fe_{67}Si_{33}$, $Fe_{54}Si_{46}$ and FeSi were then made, which were annealed at 950°C for 10 days to form the $(\alpha' + \eta)$, $(\eta + \varepsilon)$ and the ε phases, respectively. In addition, a two-phased $(\alpha' + \varepsilon)$ alloy containing 37.5 at.% Si was obtained by annealing a portion of the Fe_5Si_3 alloy at 750°C for 10 days. The prolonged-exposure (70 hrs) x-ray diffraction technique, as described in Chapter II, was applied to all samples concerned. These included the $(\alpha' + \eta)$-$Fe_{67}Si_{33}$, $(\eta + \varepsilon)$-$Fe_{54}Si_{46}$, ε-FeSi, $(\alpha' + \varepsilon)$-$Fe_{62.5}Si_{37.5}$, η-Fe_5Si_3, $(Fe_{90}Mn_{10})_5Si_3$, $(Fe_{80}Mn_{20})_5Si_3$, $(Fe_{70}Mn_{30})_5Si_3$, $(Fe_{50}Mn_{50})_5Si_3$ and Mn_5Si_5 alloys. After reduction the diffraction patterns exhibit distinctive details of the lines as shown in Figs. 9 and 10. These diffraction spectra indicate that at the Bragg angle of (211) reflection, $2\theta = 70.026°$, there co-exist a sharp line in ε-FeSi diffraction pattern (Fig. 10a) and a much diffused line in the $(\alpha' + \varepsilon)$-$Fe_{62.5}Si_{37.5}$ spectrum (Fig. 10b). It is interesting to note that the corresponding line of particular interest is rather sharp and narrow in the spectrum of $(\eta + \varepsilon)$-$Fe_{54}Si_{46}$ (Fig. 10e), while it is much more broadened in the case of $(\eta + \alpha')$-$Fe_{67}Si_{33}$ (Fig. 10c). This leads one to believe that the diffused background of the (211) line in the Fe_5Si_3 diffraction pattern is indeed due to the

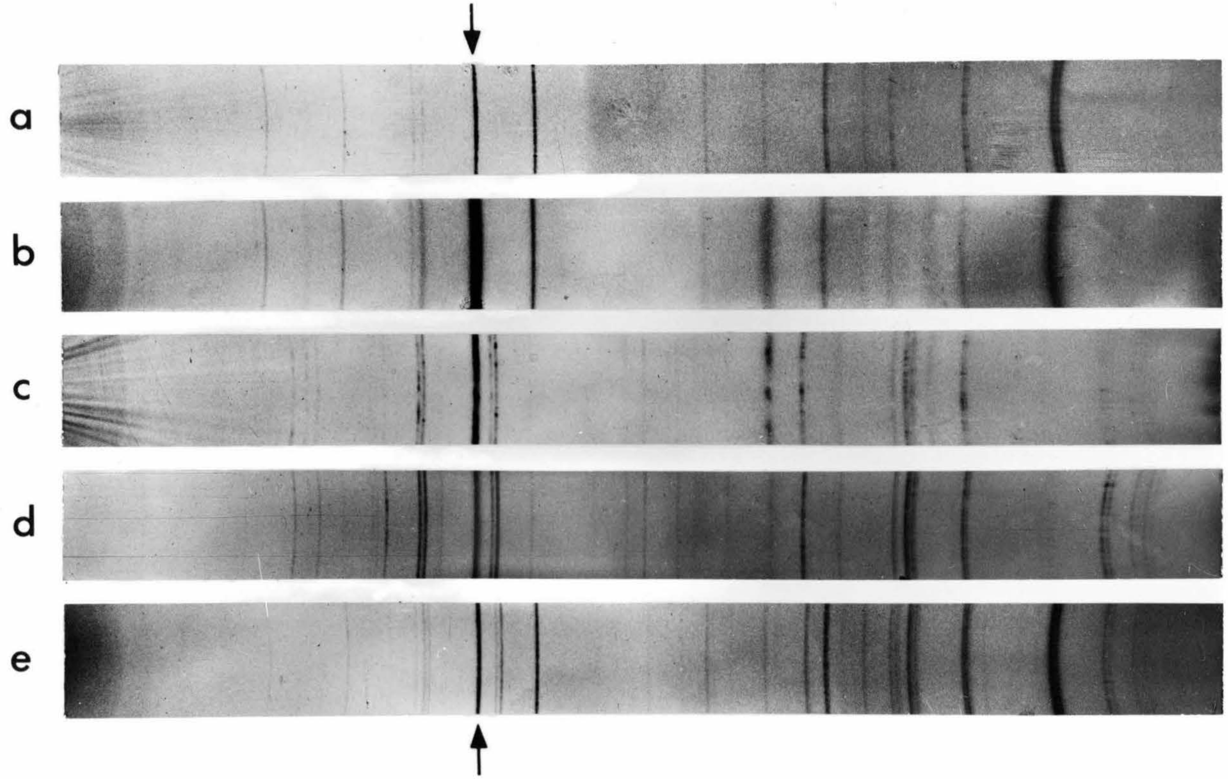

Fig. 10. Debye-Scherrer diffraction patterns of (a) ε - FeSi, (b) $(\alpha' + \varepsilon)$-$Fe_{62.5}Si_{37.5}$, (c) $(\eta + \alpha')$-$Fe_{67}Si_{33}$, (d) η-Fe_5Si_3, and (e) $(\eta + \varepsilon)$-$Fe_{54}Si_{46}$.

contribution of the small amount of the α' phase. The amount of the α' phase in Fe_5Si_3 was estimated as 10-20%. Furthermore, Fig. 9 shows that the α' phase decreases as Mn concentration increases, and it appears to vanish at composition $x = 30$.

Attempts were made to eliminate the α' phase in the Fe-rich alloys. These included the prolonged annealing time up to a month, the technique of solid state quenching, variation of annealing temperature (between 825° and 1030°C), and introduction of 0.2 - 0.5 at.% carbon as the structure stabilizing agent(18).

All of these efforts to stabilize the $D8_8$ structure in the Fe-rich $(Fe_{100-x}Mn_x)_5Si_3$ alloys were made in vain. One finally just has to live with it.

B. Mössbauer Effect

In Fig. 11, the room temperature Mössbauer absorption spectra for the $(Fe_{100-x}Mn_x)_5Si_3$ alloys are shown. All alloys except for $x = 0$ and 10 exhibit features of non-magnetic splitting. For $T = 77^oK$ and 423^oK, the Mössbauer spectra of the alloys are shown, respectively, in Figs. 12 and 13.

It is clear from these figures that all alloys are in the paramagnetic state at $T = 423^oK$ and, on the other hand, all but for $x = 90$ show magnetic hyperfine splitting at $T = 77^oK$. It can be seen from Fig. 11 that as the Mn concentration x decreases from $x = 90$ the spectrum deviates gradually from its symmetrical quadrupole doublet. For higher Fe concentration, the appearance of a second quadrupole component becomes evident. Figures 14, 15, and 16 show

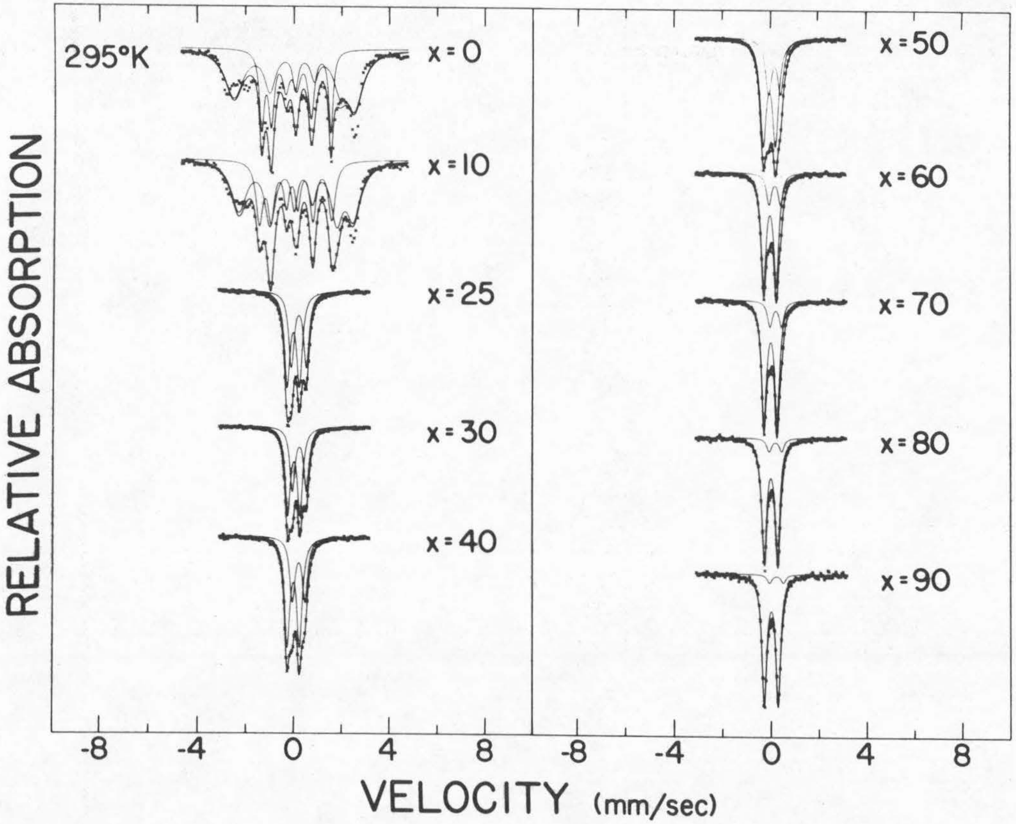

Fig. 11. Mössbauer spectra of the $(Fe_{100-x}Mn_x)_5Si_3$ alloys at 295°K

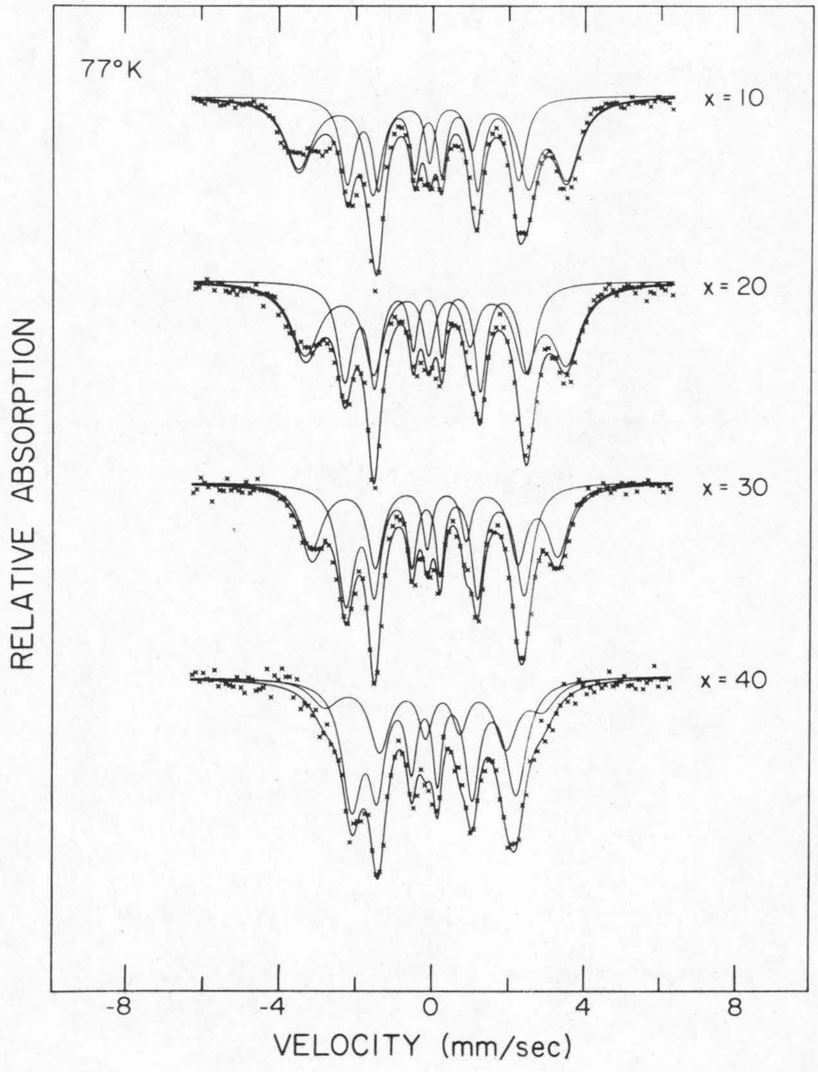

Fig. 12. Mössbauer spectra of the $(Fe_{100-x}Mn_x)_5Si_3$ alloys at 77°K

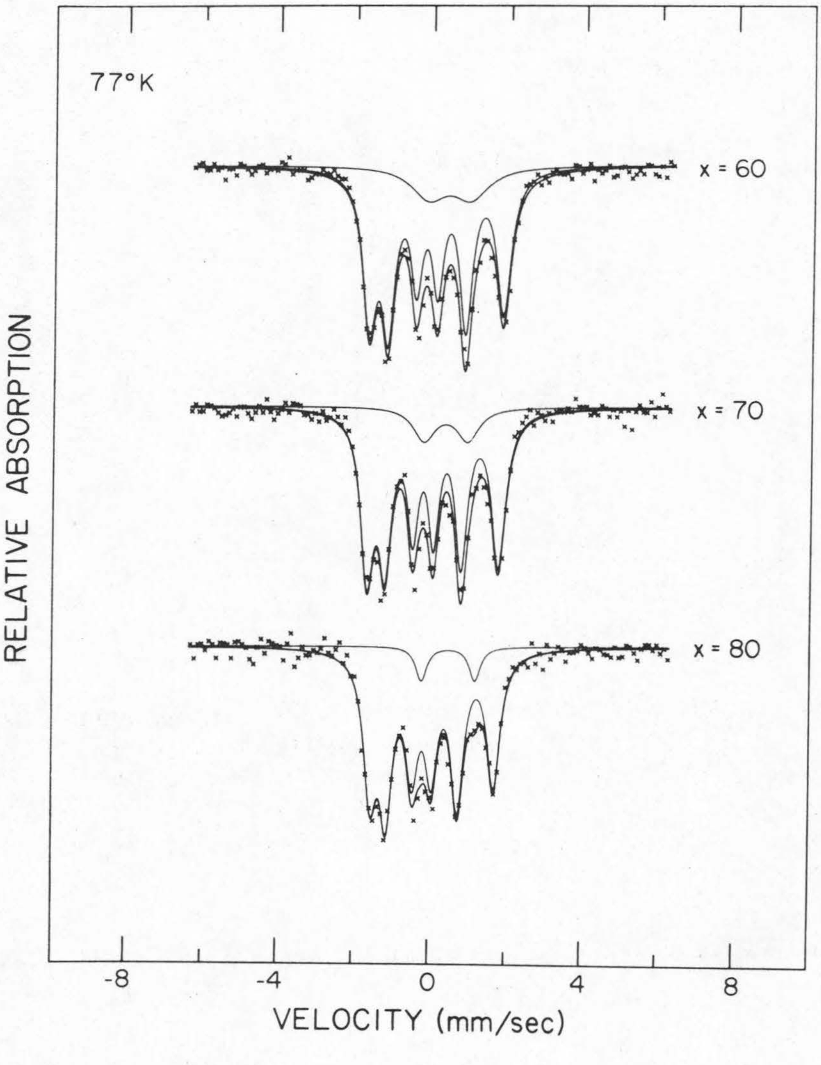

Fig. 12 (continued). Mössbauer spectra of the $(Fe_{100-x}Mn_x)_5Si_3$ alloys at 77°K.

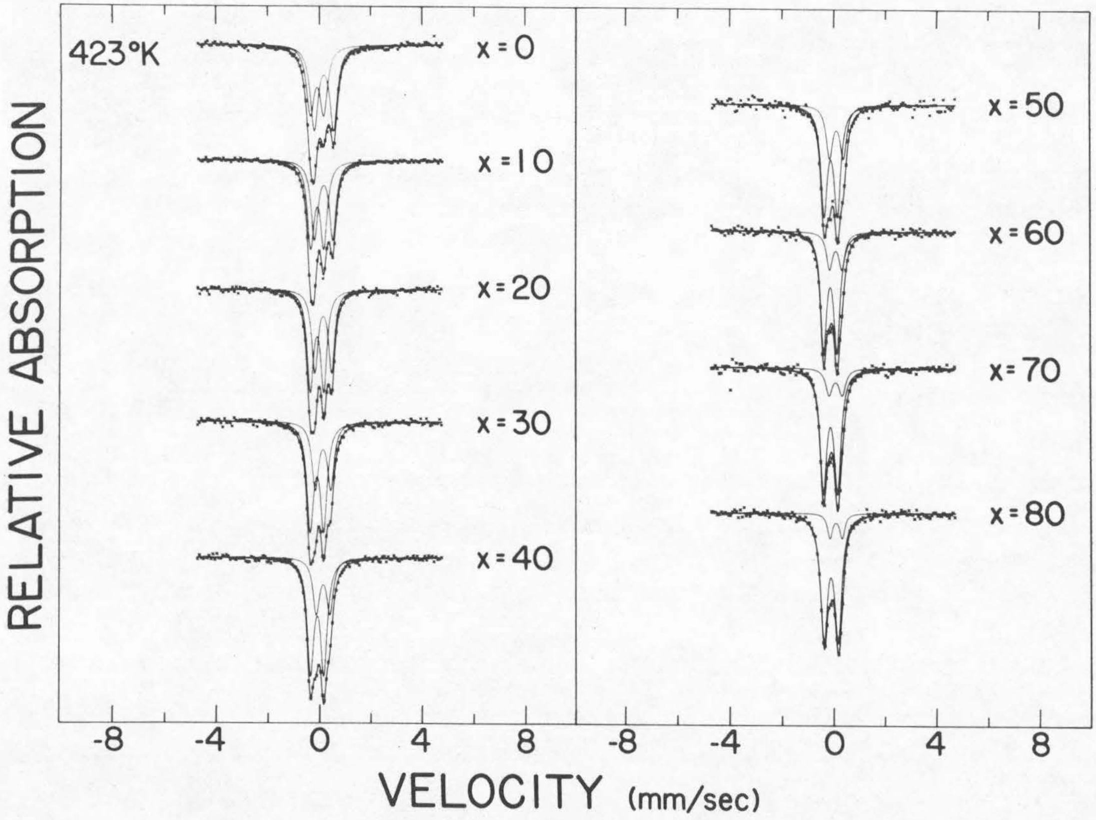

Fig. 13. The Mössbauer spectra of the $(Fe_{100-x}Mn_x)_5Si_3$ alloys at 423°K.

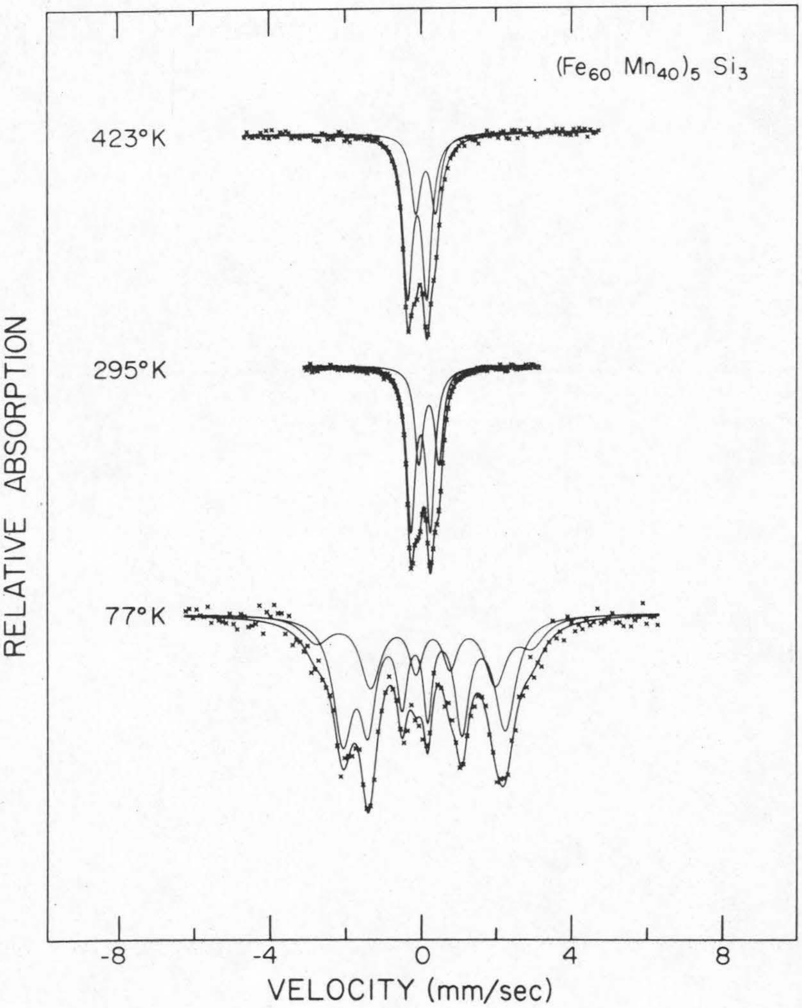

Fig. 14. Temperature dependence of the Mössbauer spectrum for the $(Fe_{60}Mn_{40})_5Si_3$ alloy .

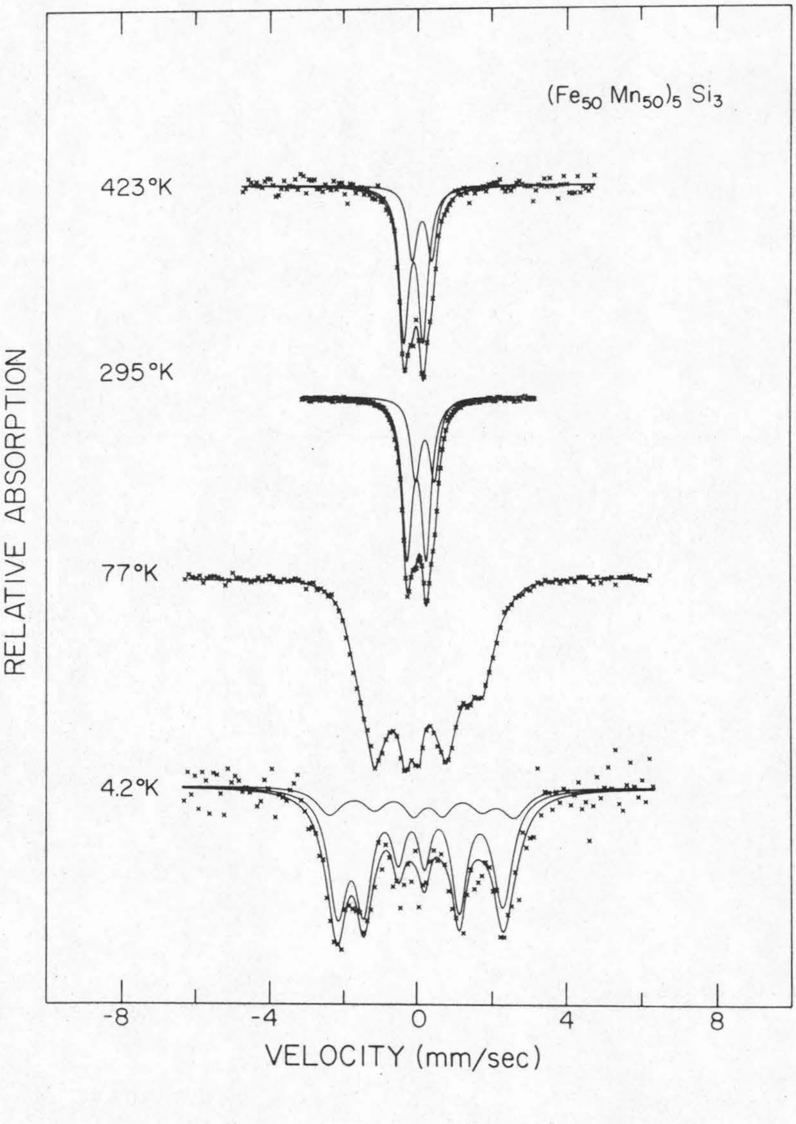

Fig. 15. Temperature dependence of the Mössbauer spectrum for the $(Fe_{50}Mn_{50})_5Si_3$ alloy.

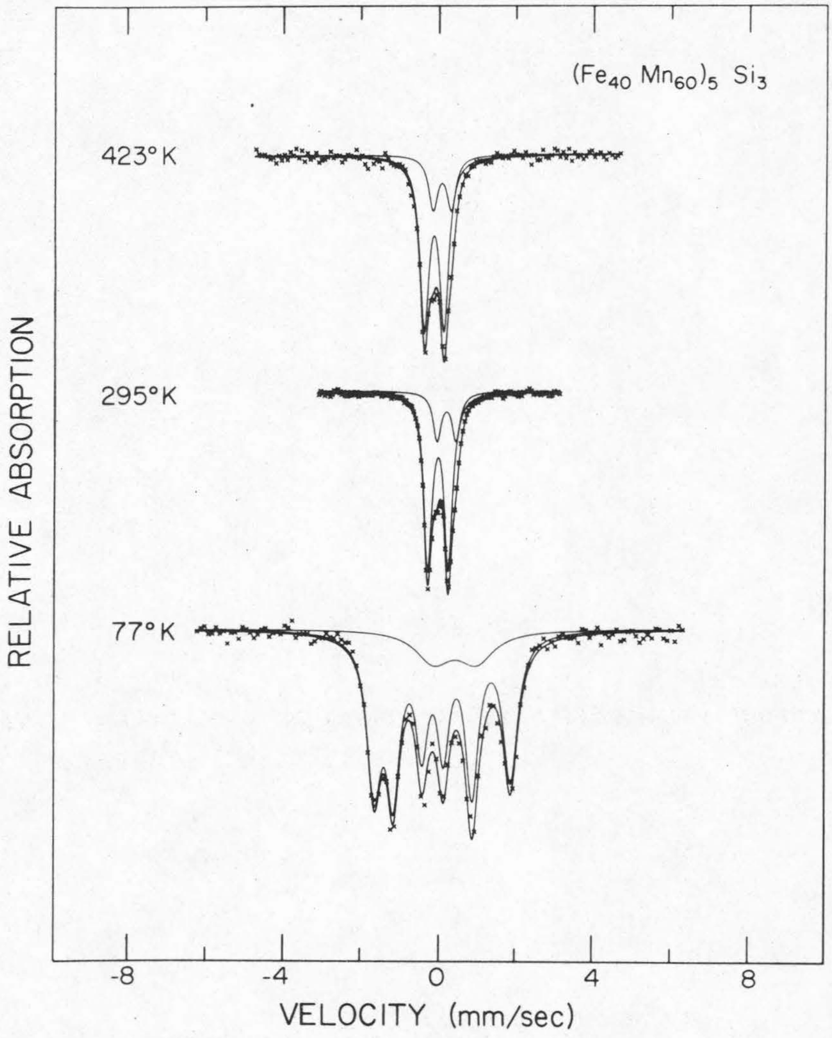

Fig. 16. Temperature dependence of the Mössbauer spectrum for the $(Fe_{40}Mn_{60})_5Si_3$ alloy.

Mössbauer spectra as functions of temperature for the alloys $(Fe_{60}Mn_{40})_5Si_3$, $(Fe_{50}Mn_{50})_5Si_3$ and $(Fe_{40}Mn_{60})_5Si_3$, respectively.

As the results of Mössbauer effect are known to reflect the structural environment of the isotope, the crystal structure and its symmetry described in part A of this chapter can provide a certain guide to the fitting of the Mössbauer spectrum. The fact that Fe atoms occupy two inequivalent sites suggests that a two-site approximation might be adopted as a fitting scheme. This means that the observed absorption spectrum may be analyzed as the superposition of two components contributed from Fe_I and Fe_{II} . Since the Fe atoms in a hexagonal lattice have lower than a three-fold symmetry, it would be reasonable in general to expect the existence of a quadrupole splitting.

The Mössbauer absorption spectra were analyzed through the use of a computer program(44) which least-squares fits the data points to the theoretical function with respect to the type of interaction. The line shape was assumed to be Lorentzian. As can be seen in Figs. 11-16, generally all spectra were fitted reasonably well with two sites. However, fitting the outer peaks of the Fe_5Si_3 spectra at 77°K and 295°K seems to present some difficulty, and this appears to become less serious in the case of $(Fe_{90}Mn_{10})_5Si_3$ spectra.

1. Room Temperature Results

Magnetic hyperfine splittings combined with quadrupole interactions have been observed in alloys for $x \doteq 0$ and 10 (Fig. 11). In particular, the room temperature spectrum of $(Fe_{80}Mn_{20})_5Si_3$ appears to verge towards a magnetic transition, and the temperature is apparently not low enough for the spectrum to show well resolved hyperfine splittings. The fact that only electric quadrupole splittings are present in alloys for $x = 25,30,40,\cdots,90$ indicates that their magnetic transition temperatures are below 295°K.

The Fe_5Si_3 Mössbauer spectrum consists of two different hyperfine splittings (hfs). The ratio of the area under the larger hfs to that of the smaller one is 6:4. In view of the fact that absorption intensities are directly proportional to the number of Fe atoms in sites, it is easy to correlate the contribution from Fe_I with the larger isomer shift corresponding to the larger hfs, and the contribution from Fe_{II} with the smaller isomer shift. Since the isomer shift is usually a smoothly varying function of alloy composition, the contribution from the two different sites may be easily distinguished with the aid of their isomer shifts which in the present case are appreciably different.

The computer-analyzed parameters of the room temperature Mössbauer spectra are tabulated in Table II. Isomer shift and quadrupole splitting are plotted against Mn concentration in Figs. 17 and 18, respectively. It is particularly interesting to note the compositional variation of the relative intensity which at first increases slowly until the composition $x = 50$ where it begins to increase exponentially as shown in Fig. 19. This immediately suggests a preferential substitution between Fe and Mn atoms (i.e., Fe_I by Mn atoms or Mn_{II} by Fe atoms).

TABLE II

Computer analyzed Mössbauer parameters measured at T = 295°K

Composition	Site	δ(mm/sec)	ΔE_Q(mm/sec)	H_{hf}(kOe)	Intensity	W or W_o (mm/sec)	α
Fe_5Si_3	I	.92 ±.004	-.470 ±.007	155.9 ±.3	.757 ±.008	.241 ±.018	1.006 ±.127
	II	-.037 ±.001	.206 ±.003	89.2 ±.1	.505 ±.005	.373 ±.014	.240 ±.021
$(Fe_{90}Mn_{10})_5Si_3$	I	.194 ±.004	-.320 ±.007	148.1 ±.3	.708 ±.019	.249 ±.022	.827 ±.125
	II	-.037 ±.003	.141 ±.005	93.2 ±.2	.453 ±.015	.268 ±.015	.231 ±.066
$(Fe_{75}Mn_{25})_5Si_3$	I	.212 ±.001	.633 ±.002		.479 ±.004	.283 ±.007	
	II	-.022 ±.001	.519 ±.001		.590 ±.004	.283 ±.002	
$(Fe_{70}Mn_{30})_5Si_3$	I	.212 ±.001	.594 ±.002		.414 ±.003	.266 ±.002	
	II	-.020 ±.001	.519 ±.001		.560 ±.004	.266 ±.002	
$(Fe_{60}Mn_{40})_5Si_3$	I	.203 ±.002	.540 ±.002		.407 ±.002	.279 ±.003	
	II	-.017 ±.001	.523 ±.001		.677 ±.006	.279 ±.003	
$(Fe_{50}Mn_{50})_5Si_3$	I	.197 ±.001	.512 ±.001		.383 ±.003	.317 ±.002	
	II	-.023 ±.001	.517 ±.001		.735 ±.004	.317 ±.002	
$(Fe_{40}Mn_{60})_5Si_3$	I	.193 ±.004	.404 ±.005		.242 ±.008	.261 ±.003	
	II	-.015 ±.001	.531 ±.001		.868 ±.011	.261 ±.003	
$(Fe_{30}Mn_{70})_5Si_3$	I	.202 ±.005	.493 ±.008		.194 ±.009	.254 ±.003	
	II	-.011 ±.001	.552 ±.001		.914 ±.012	.254 ±.003	
$(Fe_{20}Mn_{80})_5Si_3$	I	.197 ±.013	.531 ±.017		.106 ±.013	.255 ±.004	
	II	-.006 ±.001	.563 ±.002		.944 ±.017	.255 ±.004	
$(Fe_{10}Mn_{90})_5Si_3$	I	.211 ±.016	.591 ±.024		.068 ±.010	.245 ±.003	
	II	-.004 ±.001	.584 ±.001		.973 ±.013	.245 ±.003	

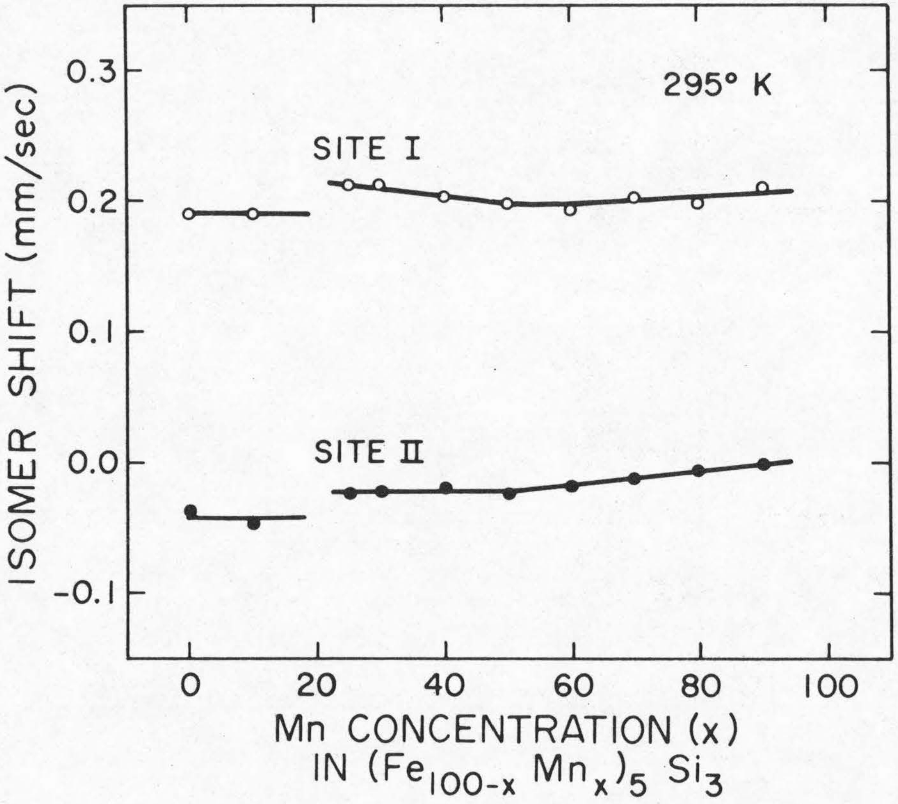

Fig. 17. Composition dependence of the isomer shift at room temperature.

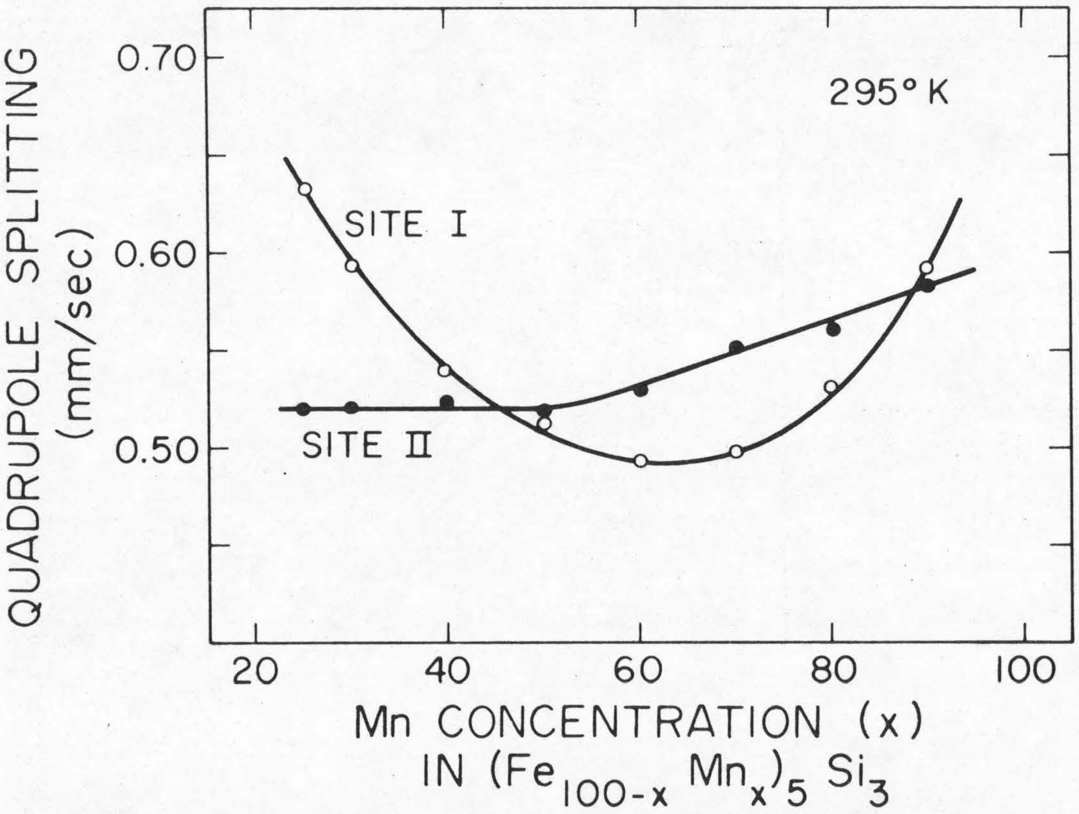

Fig. 18. Composition dependence of quadrupole splitting at room temperature.

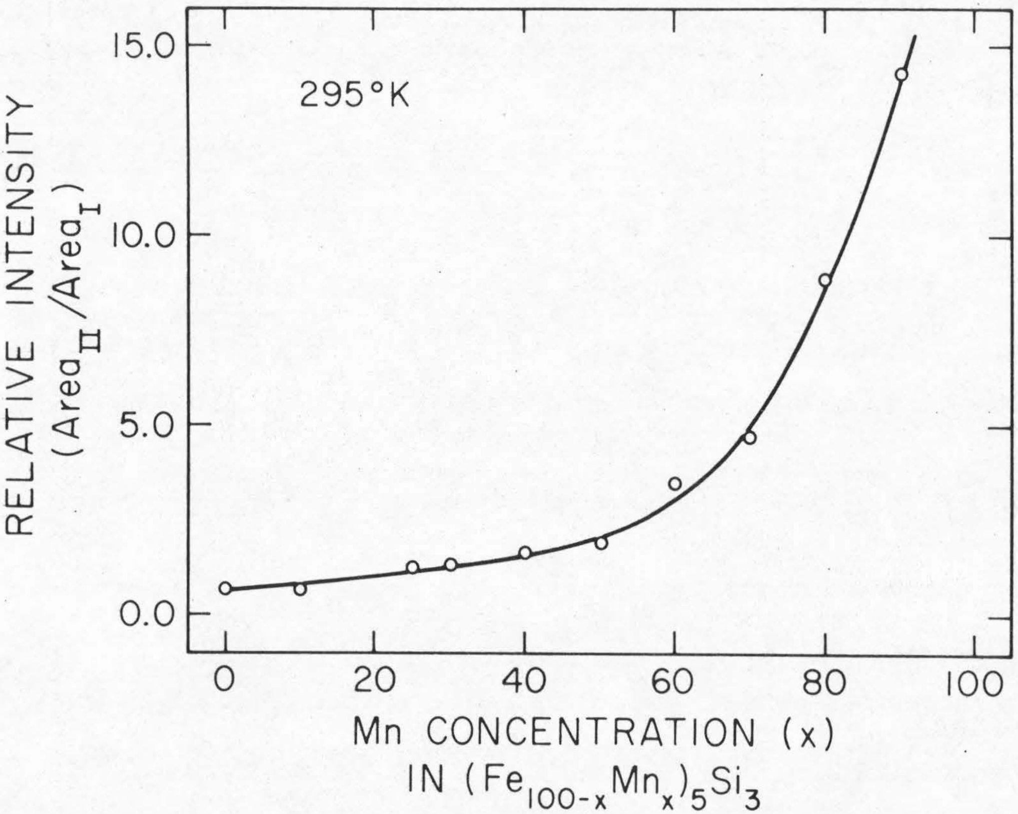

Fig. 19. Composition dependence of the relative intensity of spectra due to two inequivalent sites at room temperature.

2. Low Temperature Results

At $T = 77^{o}K$, the Mössbauer spectra of all alloys for $0 \leq x \leq 80$ exhibit hyperfine splitting, except for $x = 50$ where $(Fe_{50}Mn_{50})_5Si_3$ spectrum just begins to split magnetically, which suggests that this alloy should undergo a magnetic transition not far below this temperature.

As shown in Fig. 2, a hyperfine spectrum in a thin Fe foil may be fitted well with six Lorentzian peaks of equal width. In the case of a disordered alloy, however, the Fe atoms do not occupy just a few but, in the microscopic reality, an infinite number of sites. This in fact is the limiting case for the Fe atoms when substituted by the Mn atoms in the $(Fe_{100-x}Mn_x)_5Si_3$ lattice. In view of this, the hyperfine splitting in a two-site approximation would necessarily need to be modified such that each of the two hfs is a superposition of a great number of sites. To a first approximation, their isomer shifts and quadrupole splittings are both assumed all equal. The net effect of this is that the outer peaks of the hfs are more broadened than the inner ones. In this spirit, an additional parameter called alpha (α) factor may be usefully introduced in fitting the magnetic spectra. The α factor is defined in such a way that $W_i = W_o(1 + \alpha E_i)$ where W_i is the linewidth of the absorption peak at the Doppler velocity $V = E_i$, and W_o is the effective width at $V = 0$. The results of fitting are shown in Fig. 12, and the Mössbauer parameters are tabulated in Table III.

The isomer shift, quadrupole splitting and the linewidth of Fe_I are presented in Figs. 20-22 as functions of Mn concentration.

TABLE III

Computer analyzed Mössbauer parameters measured at T = 77°K

Composition	Site	δ(mm/sec)	ΔE_Q(mm/sec)	H_{hf}(kOe)	Intensity	W_o or W (mm/sec)	α
Fe_5Si_3	I	.225 ± .005	-.502 ± .007	226.0 ± .3	.690 ± .010	.225 ± .202	1.001 ± .088
	II	-.076 ± .005	.125 ± .004	120.5 ± .3	.461 ± .015	.291 ± .016	.220 ± .052
$(Fe_{90}Mn_{10})_5Si_3$	I	.213 ± .003	-.467 ± .006	220.4 ± .3	.684 ± .012	.228 ± .018	.770 ± .092
	II	-.080 ± .002	.127 ± .004	140.2 ± .2	.476 ± .010	.285 ± .012	.225 ± .038
$(Fe_{80}Mn_{20})_5Si_3$	I	.229 ± .008	-.363 ± .016	216.0 ± .8	.674 ± .035	.308 ± .050	.550 ± .153
	II	-.049 ± .005	.299 ± .011	150.9 ± .5	.473 ± .026	.216 ± .033	.531 ± .170
$(Fe_{70}Mn_{30})_5Si_3$	I	.231 ± .008	-.309 ± .008	204.2 ± .8	.587 ± .009	.297 ± .041	.510 ± .148
	II	-.036 ± .004	.243 ± .008	147.6 ± .4	.565 ± .009	.209 ± .024	.601 ± .150
$(Fe_{60}Mn_{40})_5Si_3$	I	.210 ± .038	-.236 ± .072	180.0 ± .3	.398 ± .067	.372 ± .131	.488 ± .424
	II	-.032 ± .009	.245 ± .019	136.5 ± 1.0	.659 ± .058	.247 ± .050	.763 ± .297
$(Fe_{50}Mn_{50})_5Si_3$	I			98.0 ± 2.0			
	II			69.0 ± 2.0			
$(Fe_{40}Mn_{60})_5Si_3$	I	.421 ± .072	1.111 ± .084		.184 ± .037	1.118 ± .199	
	II	-.019 ± .004	.250 ± .007	110.0 ± .3	.906 ± .031	.368 ± .027	.135 ± .068
$(Fe_{30}Mn_{70})_5Si_3$	I	.428 ± .046	1.152 ± .077		.127 ± .028	.694 ± .135	
	II	-.017 ± .004	.253 ± .008	107.8 ± .4	.921 ± .028	.340 ± .025	.173 ± .077
$(Fe_{20}Mn_{80})_5Si_3$	I	.527 ± .039	1.416 ± .074			.368 ± .142	
	II	-.022 ± .007	.270 ± .013	101.5 ± .6	1.023 ± .035	.411 ± .042	.020 ± .095

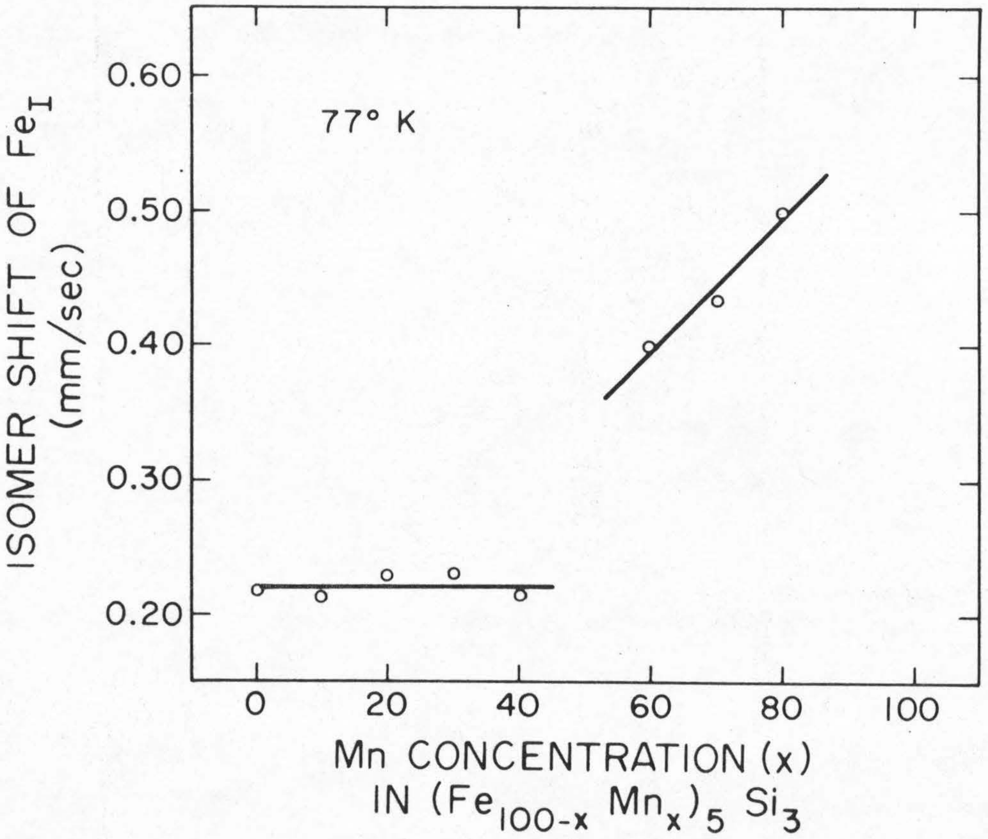

Fig. 20. Composition dependence of the isomer shift of Fe^{57} in 6(g) site measured at liquid-nitrogen temperature.

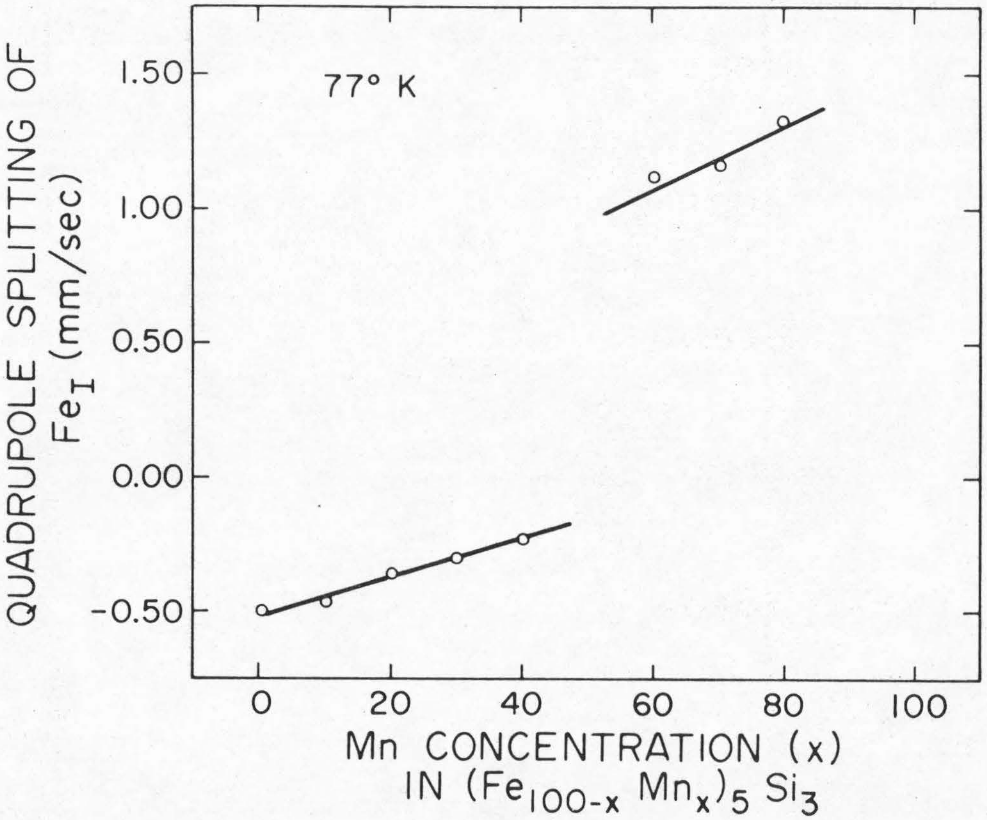

Fig. 21. Composition dependence of quadrupole splitting of Fe^{57} in 6(g) site at liquid-nitrogen temperature.

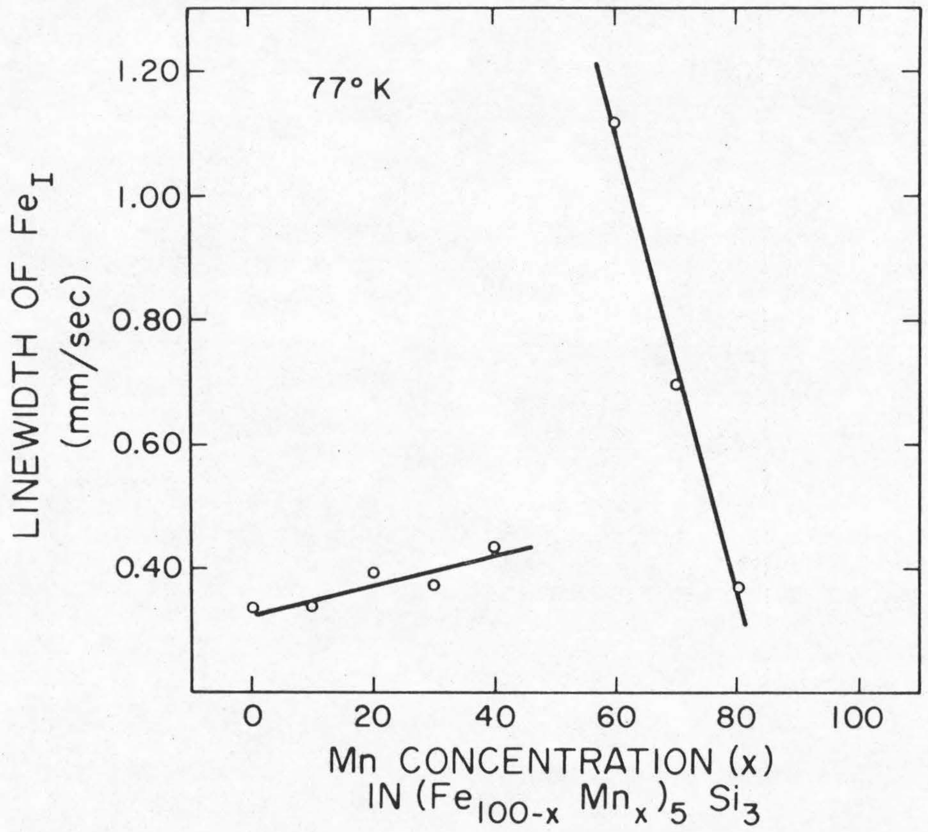

Fig. 22. Composition dependence of the spectrum linewidth of Fe^{57} in 6(g) site at liquid-nitrogen temperature.

The relative intensity at $T = 77^{\circ}K$ shown in Fig. 23 exhibits no substantial deviation from that measured at $T = 295^{\circ}K$ (Fig. 19). Figure 24 shows composition dependence of magnetic hyperfine fields H_{hf} at $T = 77^{\circ}K$. It is interesting to note that H_{hf_I} due to Fe_I decreases as composition x increases and becomes zero at $x \geq 51.5$, and $H_{hf_{II}}$ due to Fe_{II} shows a minimum at $x = 50$. Also, the α-factor is plotted in Fig. 25 as a function of Mn concentration.

3. High Temperature Results

All high temperature absorption spectra were well fitted by a two-site approximation. Mössbauer parameters are listed in Table IV.

C. Magnetization Measurements

Magnetization of the alloys in the applied field ranging from 0 to 7.3 kG is measured at various temperatures between $4.2^{\circ}K$ and $300^{\circ}K$. Composition dependence of magnetization M with $H_{appl} = 7.3$ kG measured at $77^{\circ}K$ and $4.2^{\circ}K$ is shown, respectively, in Figs. 26 and 27. For each alloy measured, its magnetization M at different field strengths is plotted against temperature and its reciprocal susceptibility $1/\chi$ is determined from the M-H_{appl} slope as a function of temperature. Figure 28 shows a typical antiferromagnetic feature of the temperature dependence of $1/\chi$ for the Mn_5Si_3 compound, in which a sharp minimum is observed at $T = 62^{\circ}K$. It is well understood that this minimum in the $1/\chi$ versus T curve is attributed to the Neél temperature of the sample. Similar minima are also observed in the reciprocal susceptibility versus temperature curves for the alloys $x = 90, 80, 70$, and 60, and their corresponding Neél points are listed

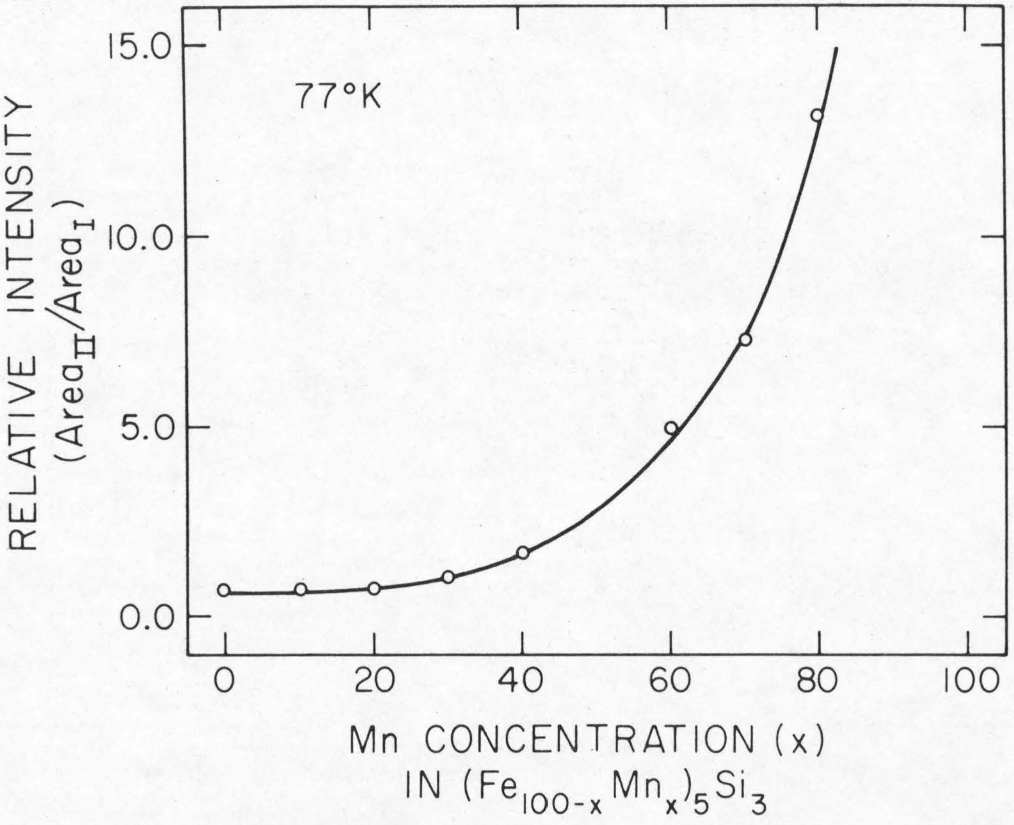

Fig. 23. Composition dependence of the relative intensity of spectra due to two inequivalent sites at liquid-nitrogen temperature.

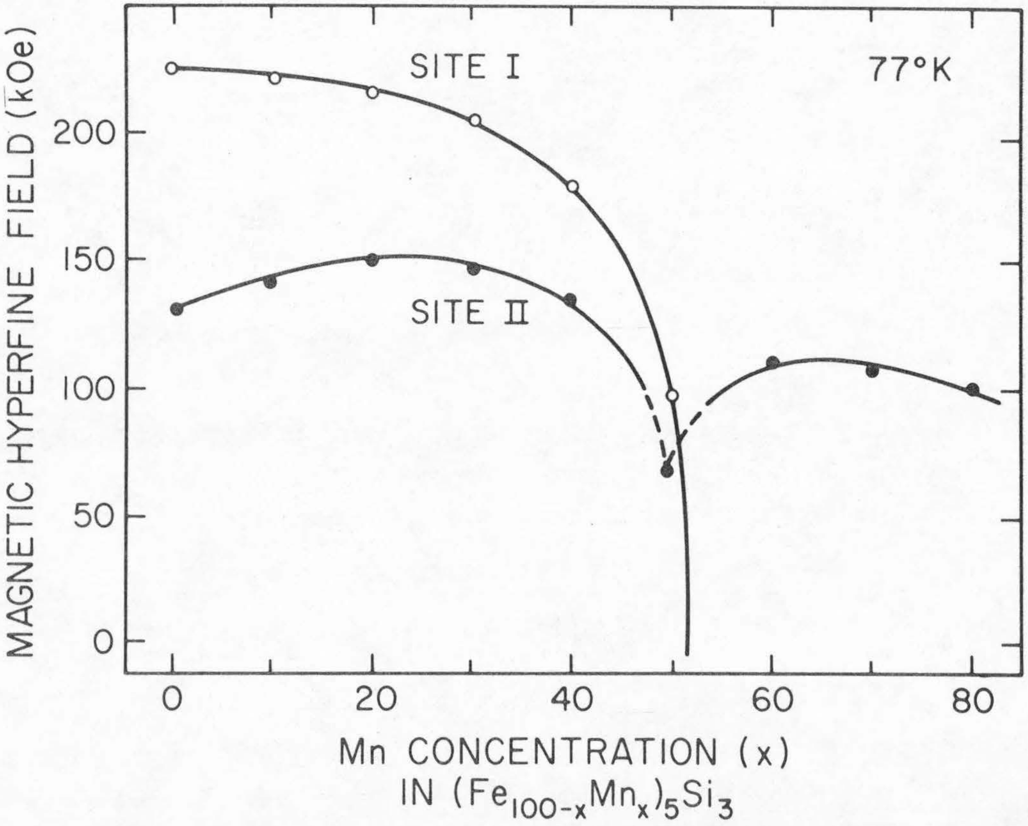

Fig. 24. Composition dependence of magnetic hyperfine field at liquid-nitrogen temperature.

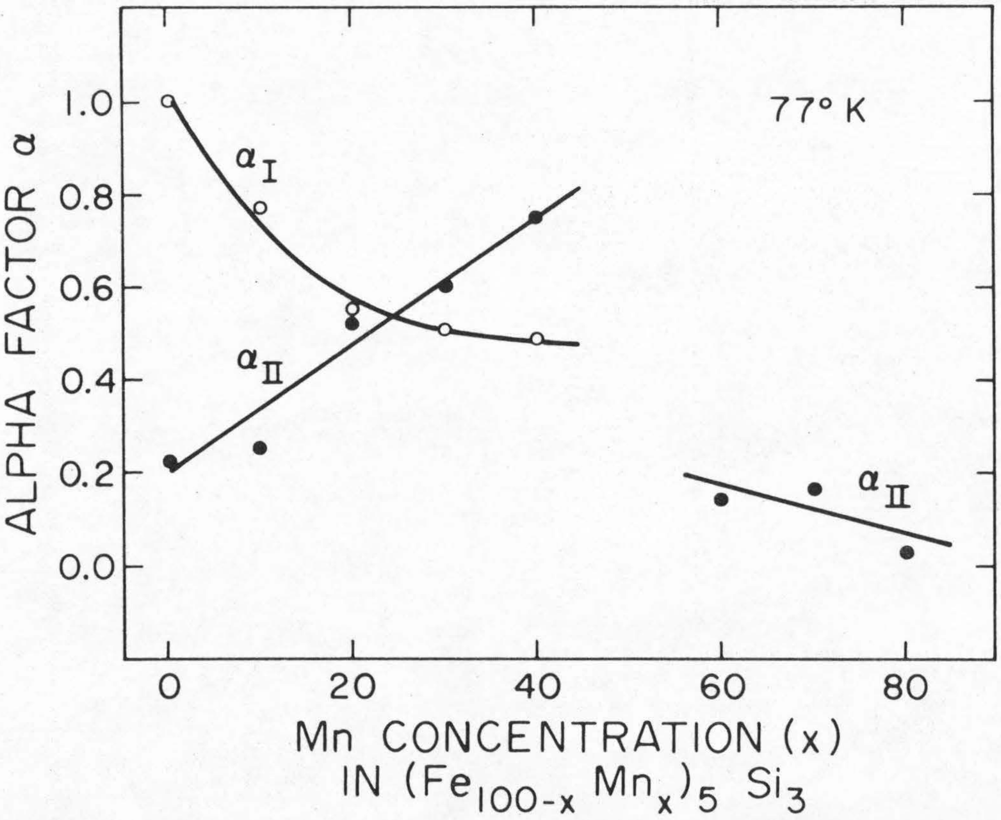

Fig. 25. Composition dependence of the line-broadening α-factor of hyperfine splitting at liquid-nitrogen temperature.

TABLE IV

Computer analyzed Mössbauer parameters measured at T = 423°K

Composition	Site	δ(mm/sec)	ΔE_Q(mm/sec)	Intensity	W(mm/sec)
Fe_5Si_3	I	.143 ±.003	.754 ±.005	.548 ±.012	.361 ±.008
	II	-.124 ±.005	.513 ±.009	.436 ±.009	.361 ±.008
$(Fe_{90}Mn_{10})_5Si_3$	I	.133 ±.003	.713 ±.004	.503 ±.008	.316 ±.006
	II	-.113 ±.003	.501 ±.005	.545 ±.007	.316 ±.006
$(Fe_{80}Mn_{20})_5Si_3$	I	.130 ±.003	.650 ±.005	.478 ±.010	.293 ±.006
	II	-.112 ±.003	.518 ±.004	.293 ±.010	.293 ±.006
$(Fe_{70}Mn_{30})_5Si_3$	I	.126 ±.006	.600 ±.007	.422 ±.014	.314 ±.008
	II	-.106 ±.004	.519 ±.005	.665 ±.016	.314 ±.008
$(Fe_{60}Mn_{40})_5Si_3$	I	.123 ±.007	.533 ±.009	.328 ±.017	.309 ±.009
	II	-.100 ±.004	.513 ±.004	.674 ±.021	.309 ±.009
$(Fe_{50}Mn_{50})_5Si_3$	I	.112 ±.013	.529 ±.016	.345 ±.030	.310 ±.016
	II	-.110 ±.007	.518 ±.008	.711 ±.037	.310 ±.016
$(Fe_{40}Mn_{60})_5Si_3$	I	.108 ±.014	.469 ±.018	.232 ±.024	.293 ±.011
	II	-.105 ±.004	.513 ±.005	.770 ±.031	.293 ±.011
$(Fe_{30}Mn_{70})_5Si_3$	I	.097 ±.022	.502 ±.025	.193 ±.039	.316 ±.013
	II	-.102 ±.006	.547 ±.005	.882 ±.047	.316 ±.013
$(Fe_{20}Mn_{80})_5Si_3$	I	.078 ±.012	.485 ±.014	.223 ±.026	.318 ±.008
	II	-.108 ±.004	.548 ±.003	.888 ±.031	.318 ±.008

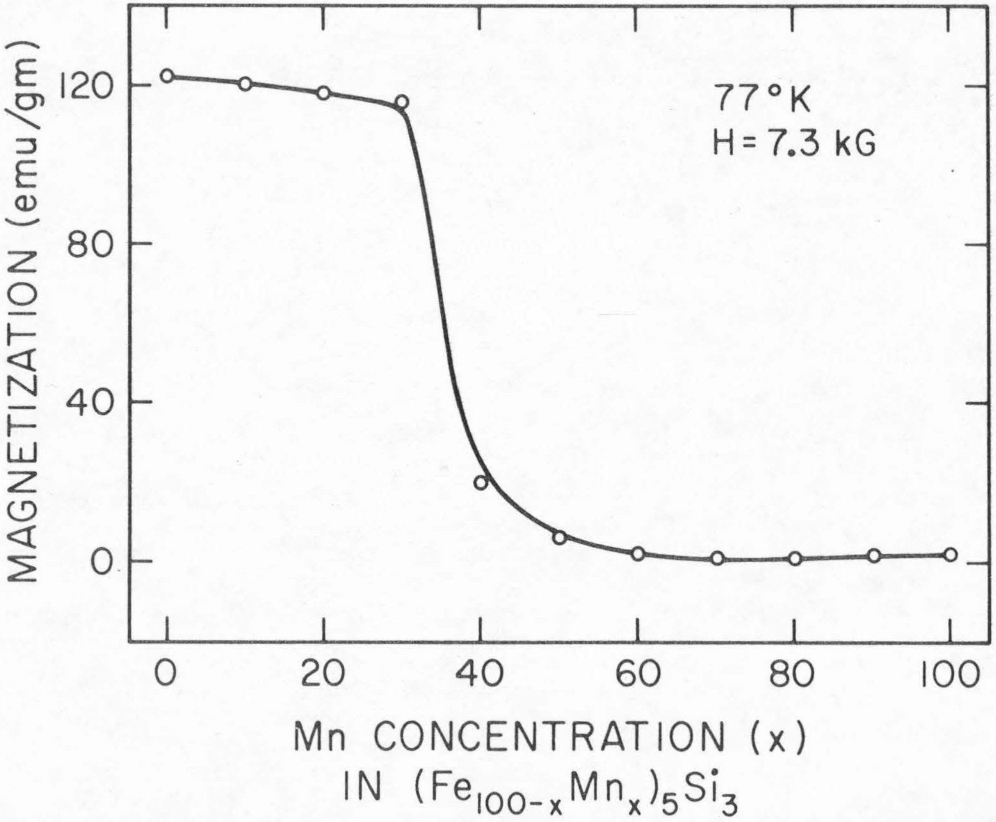

Fig. 26. Composition dependence of magnetization with $H_{appl} = 7.3$ kG at liquid-nitrogen temperature.

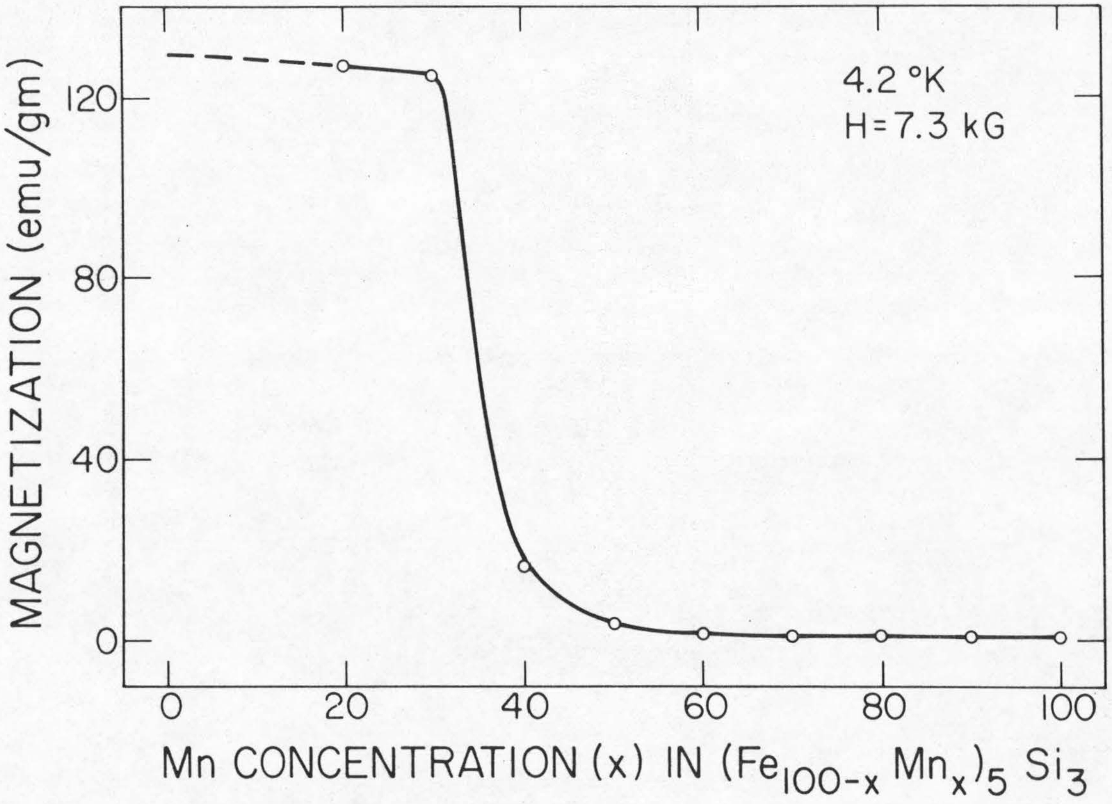

Fig. 27. Composition dependence of magnetization with $H_{appl} = 7.3$ kG at liquid-helium temperature.

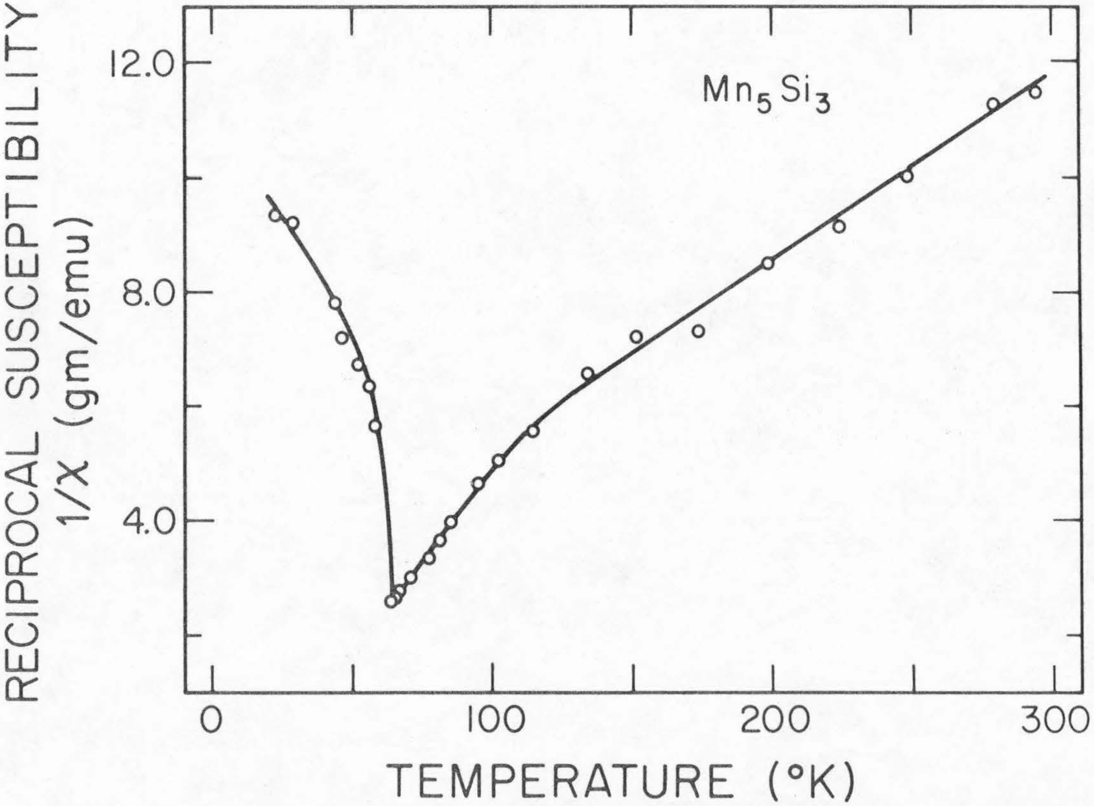

Fig. 28. Temperature dependence of reciprocal susceptibility for the Mn_5Si_3 compound.

in Table V.

Alloys for $x = 10,20,30$ and 40 show significant ferromagnetic saturation in the isothermal field dependence of their magnetization curves. The Curie points of the $(Fe_{60}Mn_{40})_5Si_3$ and $(Fe_{70}Mn_{30})_5Si_3$ alloys are found to be $T_c = 198.5^\circ K$ and $T_c = 252.0^\circ K$, respectively. A typical magnetization M versus temperature curve for the $(Fe_{70}Mn_{30})_5Si_3$ alloy is shown in Fig. 29. Samples for $x = 0,10$ and 20 have their ferromagnetic transition above room temperature which the present apparatus is not capable of detecting.

It is interesting to observe a very much broadened minimum (from 10° to $90^\circ K$) in the reciprocal susceptibility $1/\chi$ versus temperature curve for the $(Fe_{50}Mn_{50})_5Si_3$ alloy shown in Fig. 30 with the temperature variation of magnetization M at $H_{appl} = 7.3$ kG.

D. Curie Temperature

The present magnetometer is designed to operate at and below room temperature, and is sufficient in measuring the Curie points ($T_c < 300^\circ K$) of samples $x = 30$ and 40. However, results of the room temperature Mössbauer experiment, as described in part B, indicate that alloys for $x = 0,10$ and 20 undergo a magnetic transition above or near room temperature. These "high temperature" Curie points have been obtained by the inductance bridge technique as explained in Chapter II. The results are tabulated in Table VI. A typical inductance bridge output versus temperature curve for Fe_5Si_3 is shown in Fig. 31. The range of ferromagnetic transition measured by this technique is typically 2°-$5^\circ K$. The magnetic transition temperatures determined by both inductance bridge technique and magnetization measurements are presented in

TABLE V

Neel temperature of $(Fe_{100-x}Mn_x)_5Si_3$ alloys corresponding to composition x = 50, 60, 70, 80, 90 and 100

Alloy	Néel temperature $T_N(^oK)$
$(Fe_{50}Mn_{50})_5Si_3$	$30.0^o \pm 3.0^o$
$(Fe_{40}Mn_{60})_5Si_3$	$88.0^o \pm 1.0^o$
$(Fe_{30}Mn_{70})_5Si_3$	$85.0^o \pm 1.0^o$
$(Fe_{20}Mn_{80})_5Si_3$	$86.0^o \pm 1.0^o$
$(Fe_{10}Mn_{90})_5Si_3$	$73.0^o \pm 1.0^o$
Mn_5Si_3	$62.0^o \pm 1.0^o$

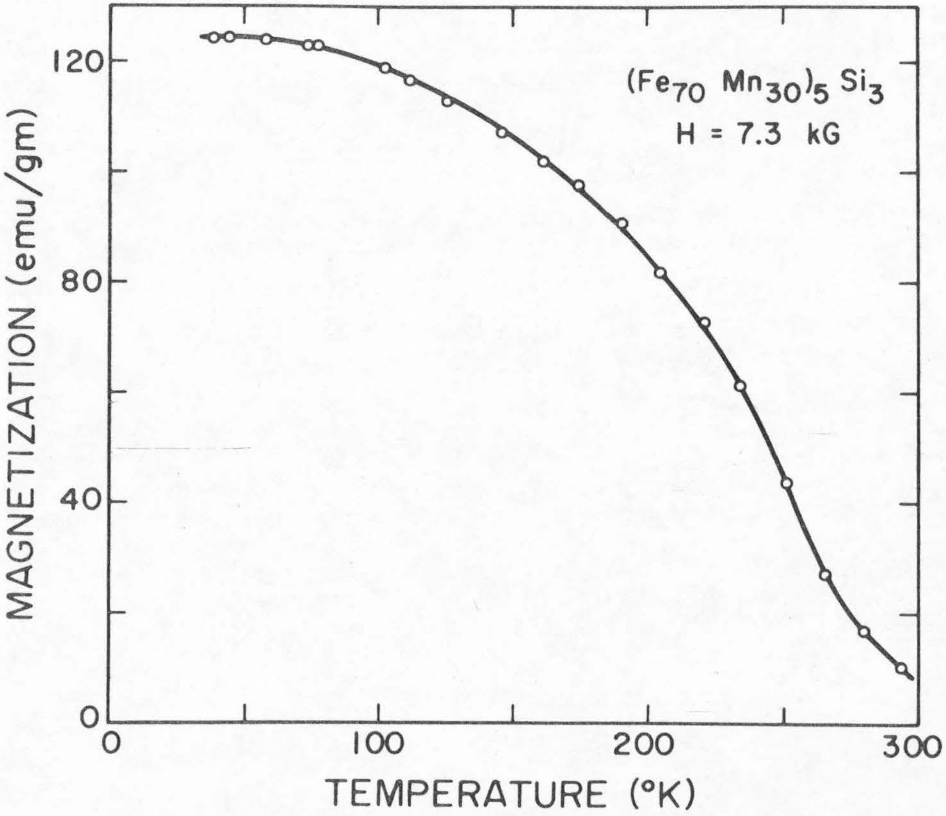

Fig. 29. Temperature dependence of magnetization with an applied field of 7.3 kG for the $(Fe_{70}Mn_{30})_5Si_3$ alloy.

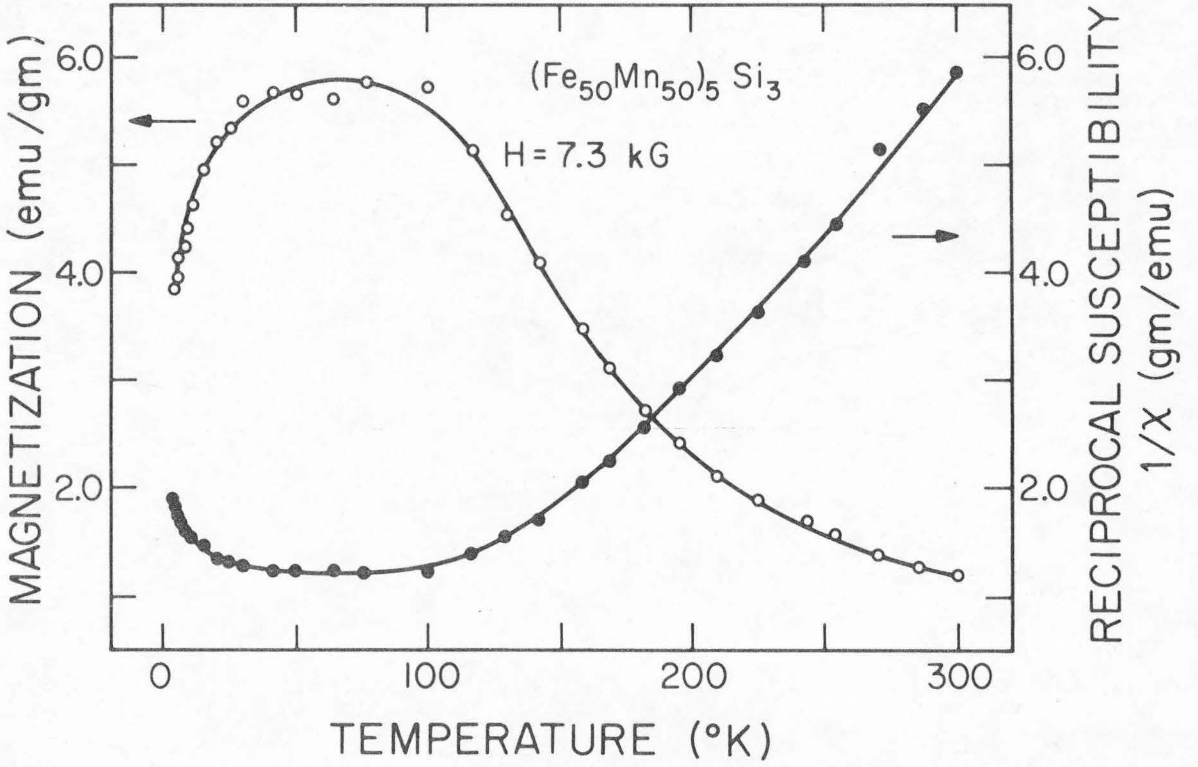

Fig. 30. Temperature dependence of magnetization with an applied field of 7.3 kG and reciprocal susceptibility for the $(Fe_{50}Mn_{50})_5Si_3$ alloy.

TABLE VI

Curie temperature of $(Fe_{100-x}Mn_x)_5Si_3$ alloys corresponding to composition x = 0,10,15,20,25,30,40 and 50

Alloy	Curie temperature T_c (°K)
Fe_5Si_3	$367.0^o \pm 0.5^o$
$(Fe_{90}Mn_{10})_5Si_3$	$349.5^o \pm 0.5^o$
$(Fe_{85}Mn_{15})_5Si_3$	$335.0^o \pm 0.5^o$
$(Fe_{80}Mn_{20})_5Si_3$	$314.8^o \pm 0.5^o$
$(Fe_{75}Mn_{25})_5Si_3$	$288.0^o \pm 0.5^o$
$(Fe_{70}Mn_{30})_5Si_3$	$252.0^o \pm 0.5^o$
$(Fe_{60}Mn_{40})_5Si_3$	$198.5^o \pm 1.5^o$
$(Fe_{50}Mn_{50})_5Si_3$	$78.0^o \pm 3.0^o$

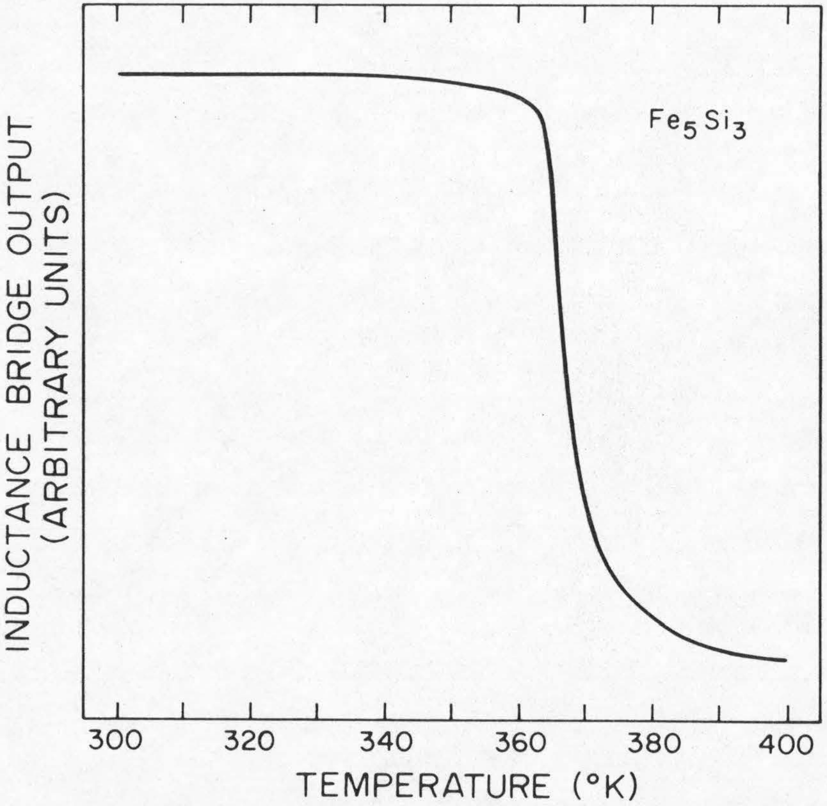

Fig. 31. Inductance bridge output vs. temperature for the Fe_5Si_3 compound.

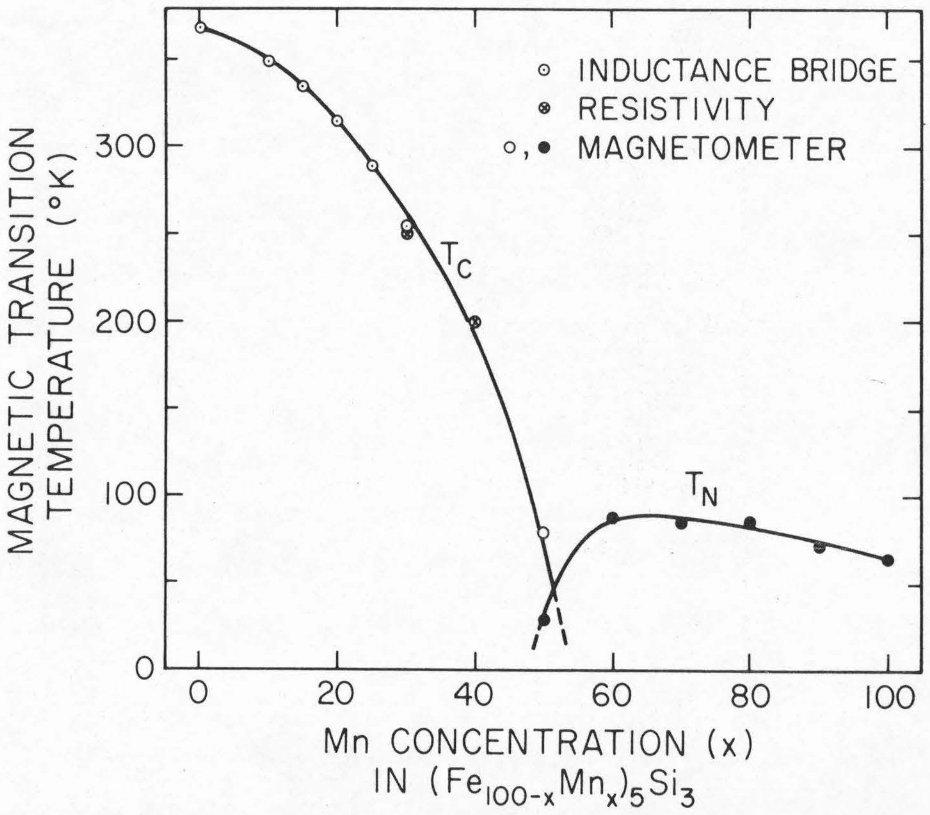

Fig. 32. Composition dependence of Curie and Néel temperatures.

Fig. 32 as functions of composition.

E. Electrical Resistance

The relative resistance $R(T)/R(300^oK)$ for the intermetallic compound Fe_5Si_3 is plotted as a function of temperature from 4^oK to 300^oK in Fig. 33. The temperature variation appears to follow reasonably well the Bloch-Grüneisen model. At high temperatures (above 70^oK), $R(T)/R(300^oK)$ of Fe_5Si_3 varies linearly with temperature. The coefficient of T is approximately $3.824 \times 10^{-2} (^oK)^{-1}$. Between 35^oK and 60^oK, the temperature variation obeys a T^5 law. Similar $R(T)/R(300^oK)$ versus T curves are observed in the $(Fe_{100-x}Mn_x)_5Si_3$ alloys for $x = 30$ and 40, except that a change of slope is evident for $x = 30$ and 40. The temperature corresponding to these slope changes are found to be quite close to the Curie points for these alloys as stated earlier. Figures 34 and 35 show the relative resistance $R(T)/R(300^oK)$ for $(Fe_{70}Mn_{30})_5Si_3$ and $(Fe_{60}Mn_{40})_5Si_3$, respectively.

The relative resistance versus temperature curves exhibit a drastic change as the Mn concentration x increases through $x = 50$. At this composition, $R(T)/R(300^oK)$ shows a well defined minimum at approximately $T = 35^oK$ (Fig. 36). As composition x increases further, more pronounced resistive minima can be seen (Figs. 37-39). It should be noted that the temperature corresponding to all these $R(T)/R(300^oK)$ minima (T_{min}) is very close to the Neél temperatures reported from the magnetization measurements. Furthermore, the relative resistance (for $x = 50$, 60, 70 and 90) varies approximately linearly with T at high temperatures, and quadratically just below

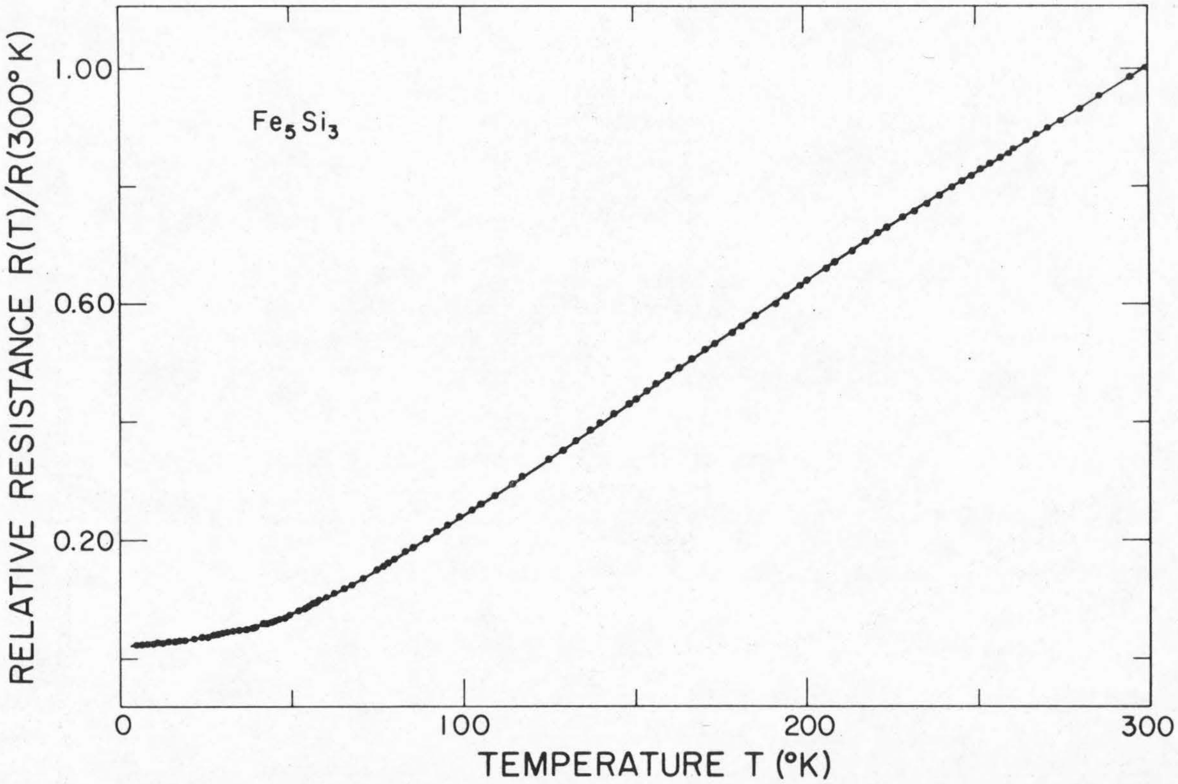

Fig. 33. Temperature dependence of relative resistance for the Fe_5Si_3 compound.

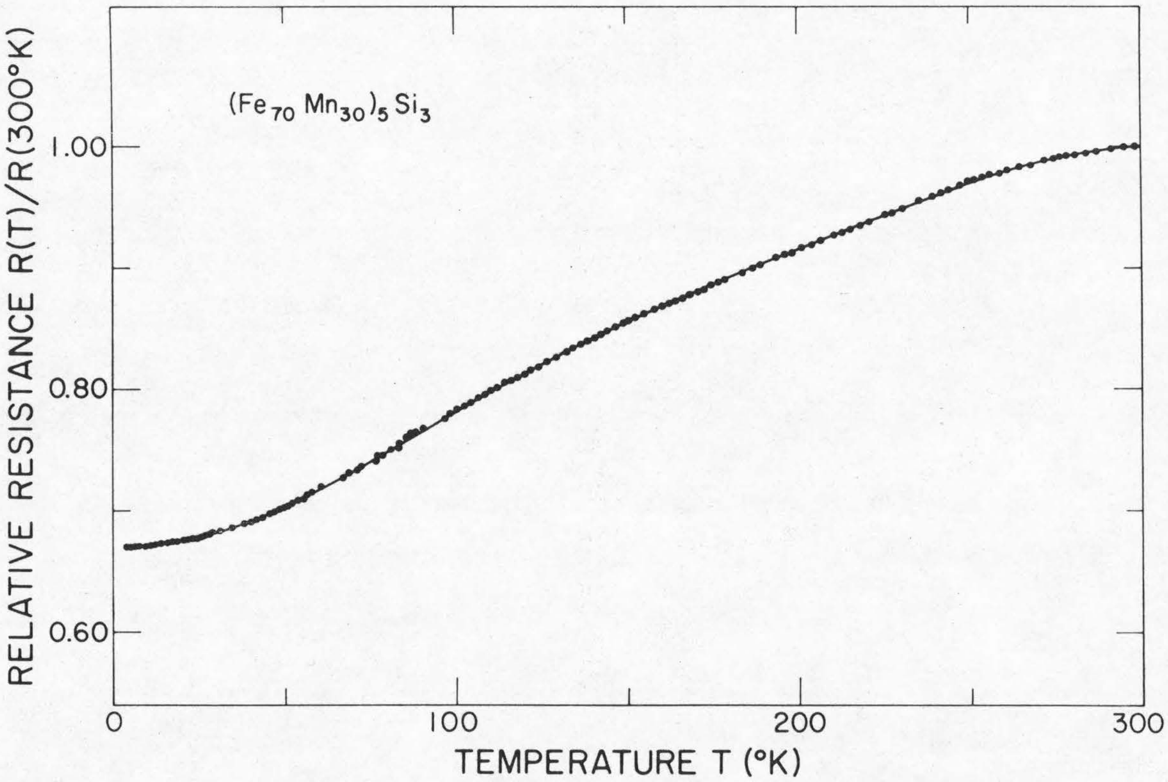

Fig. 34. Temperature dependence of relative resistance for the $(Fe_{70}Mn_{30})_5Si_3$ alloy.

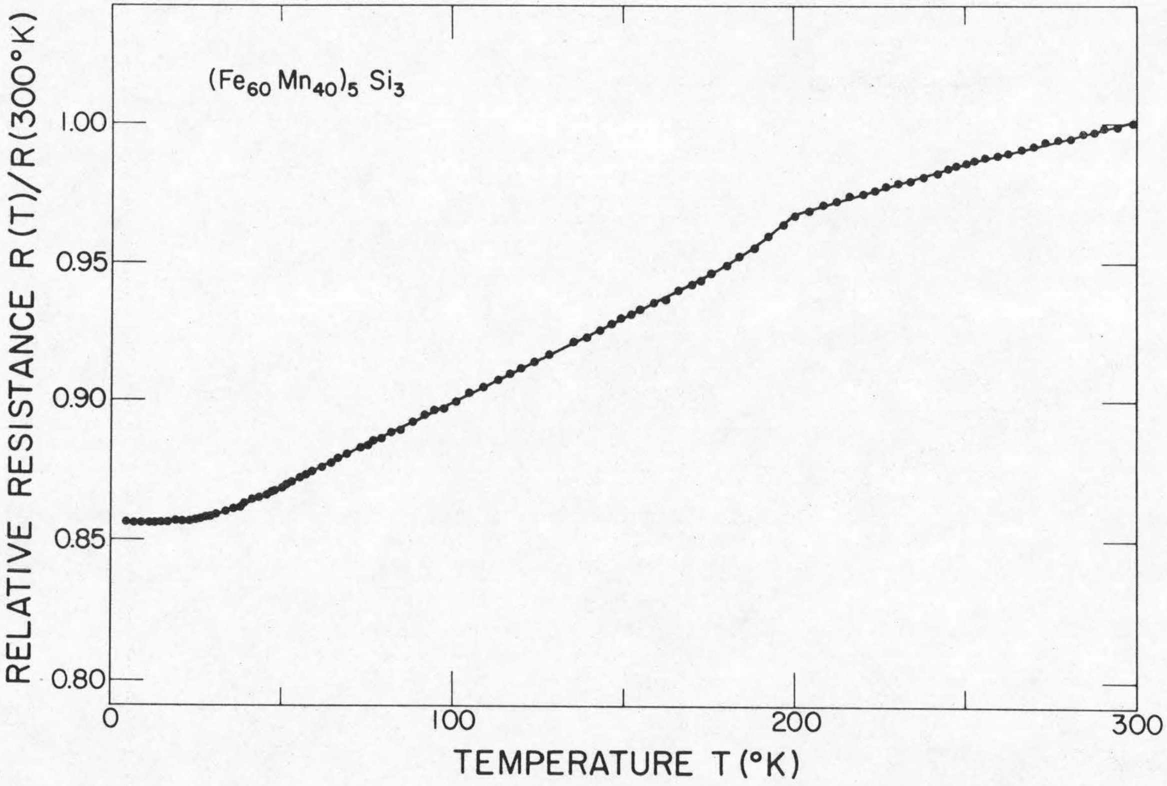

Fig. 35. Temperature dependence of relative resistance for the $(Fe_{60}Mn_{40})_5Si_3$ alloy.

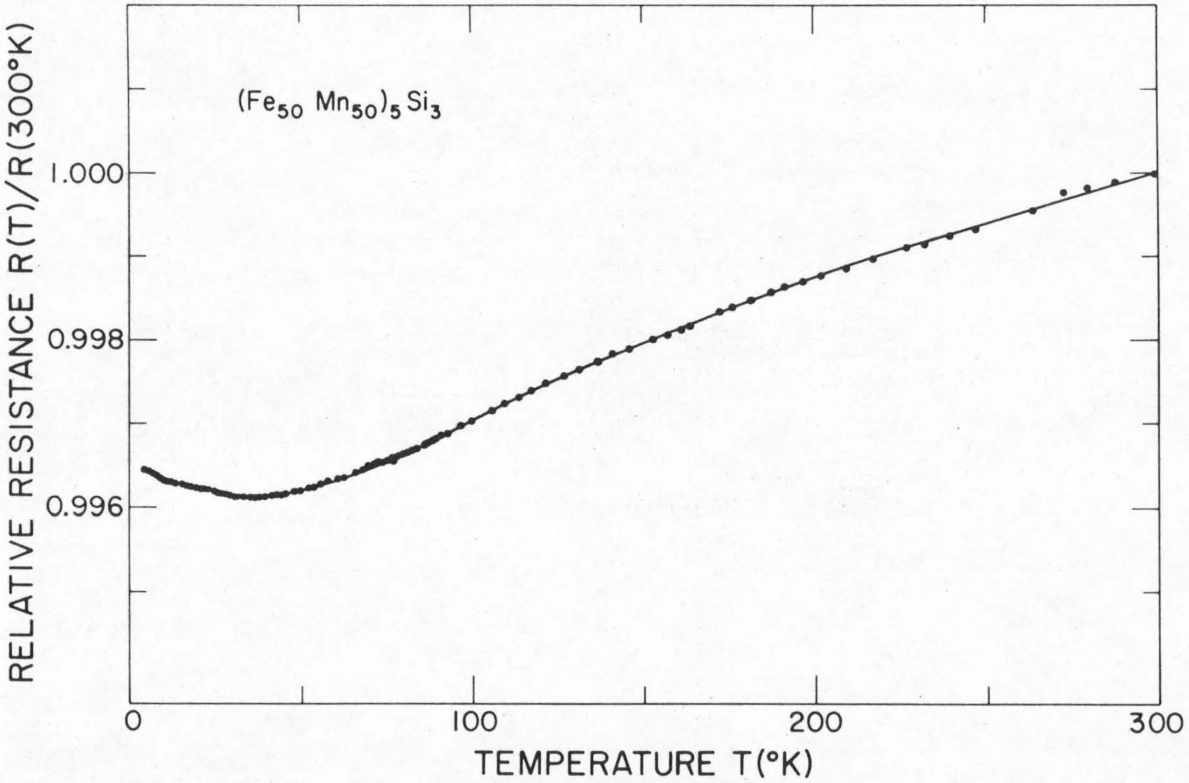

Fig. 36. Temperature dependence of relative resistance for the $(Fe_{50}Mn_{50})_5Si_3$ alloy.

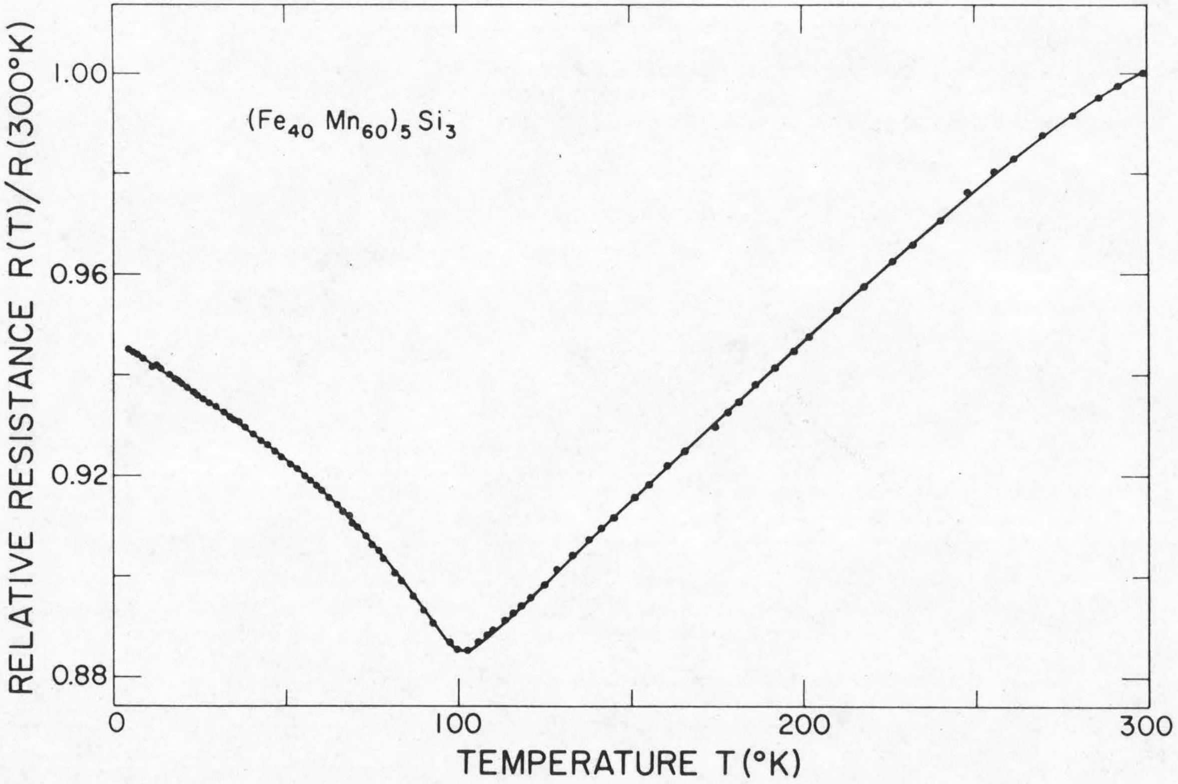

Fig. 37. Temperature dependence of relative resistance for the $(Fe_{40}Mn_{60})_5Si_3$ alloy.

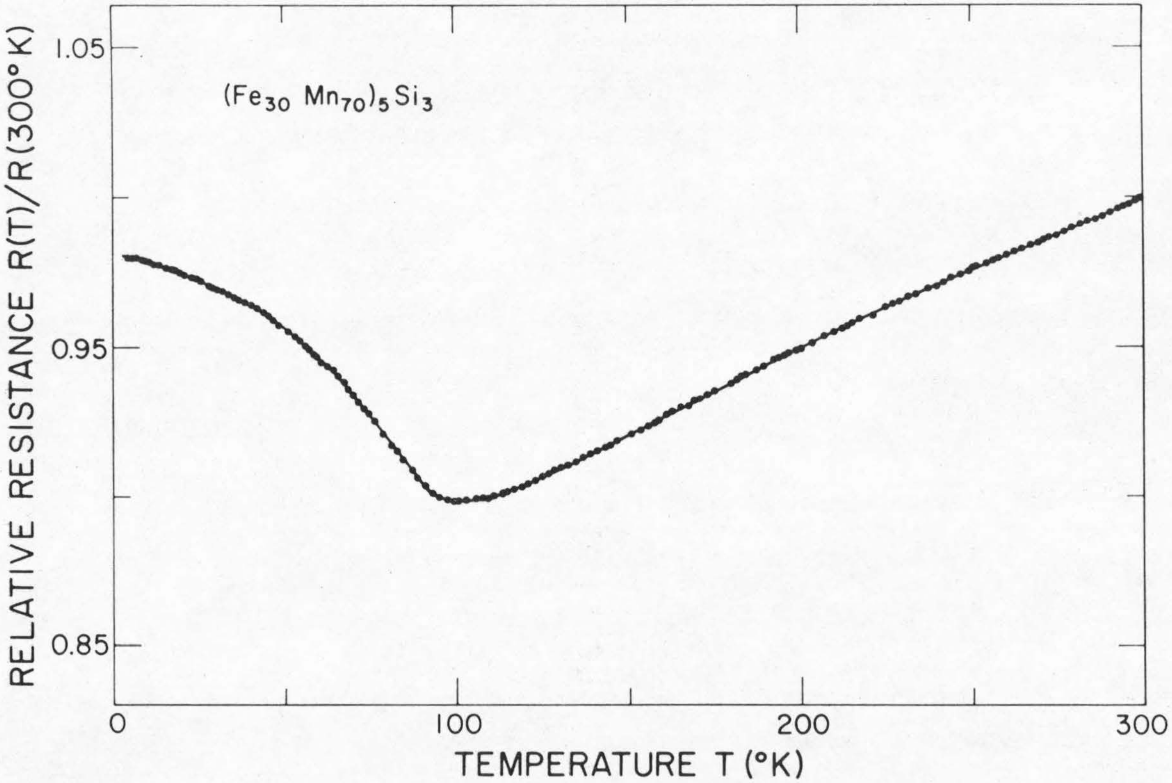

Fig. 38. Temperature dependence of relative resistance for the $(Fe_{30}Mn_{70})_5Si_3$ alloy.

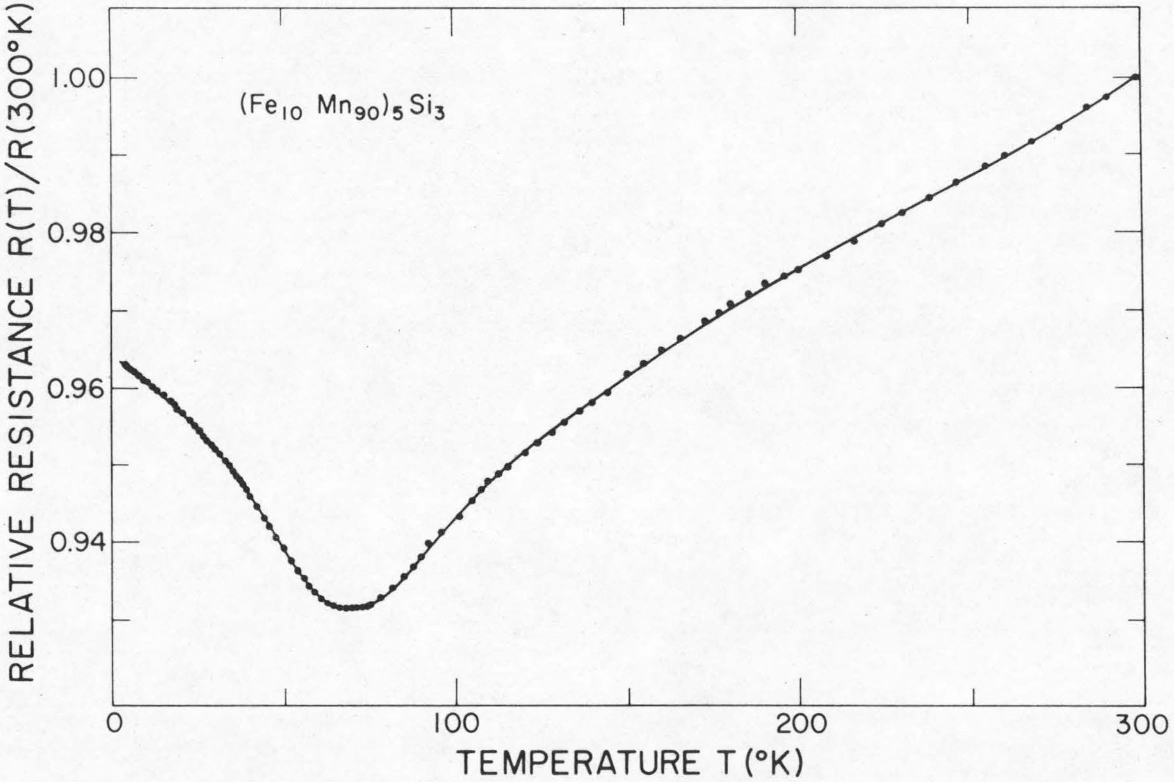

Fig. 39. Temperature dependence of relative resistance for the $(Fe_{10}Mn_{90})_5Si_3$ alloy.

T_{min} . A typical $R(T)/R(300^{o}K)$ versus T^2 curve for $x = 70$ is shown in Fig. 40.

As can be seen in Fig. 41, the relative resistance of Mn_5Si_3 as a function of temperature exhibits a rather interesting feature. In the high temperature region $R(T)/R(300^{o}K)$ varies very slowly with temperature, while at low temperatures (between $4.2^{o}K$ and $25^{o}K$) the resistance ratio declines sharply with decreasing temperature. A gradual transition is seen to take place around $T = 60^{o}K$. It is noted that this "transition" temperature is quite close to the Néel point of the compound ($T_N = 62^{o}K$) as determined from the earlier measurements.

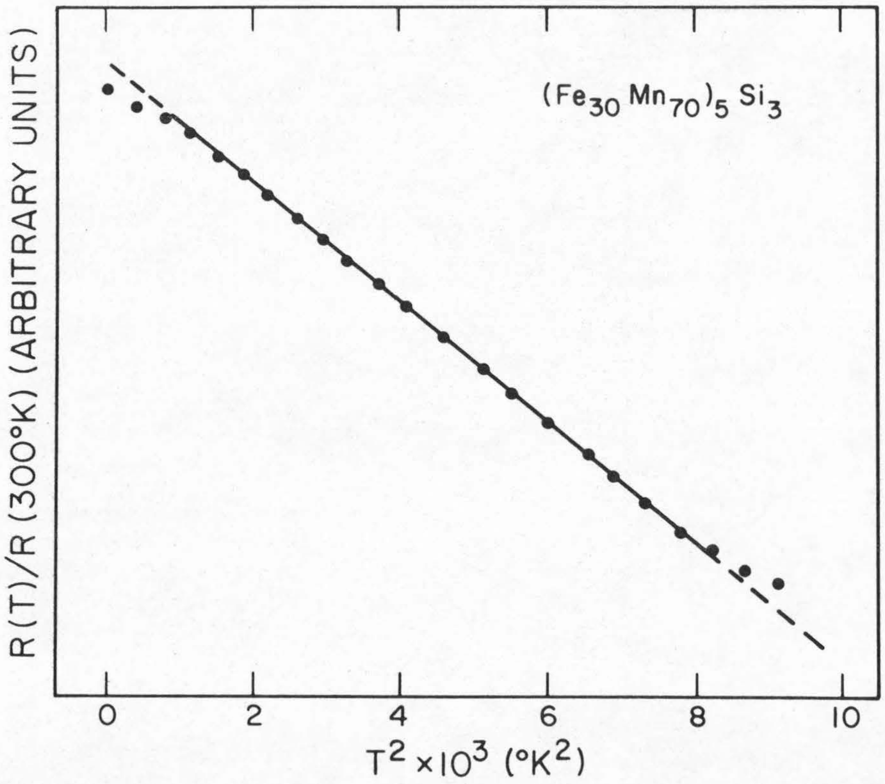

Fig. 40. T^2 dependence of the relative resistance for the $(Fe_{30}Mn_{70})_5Si_3$ alloy.

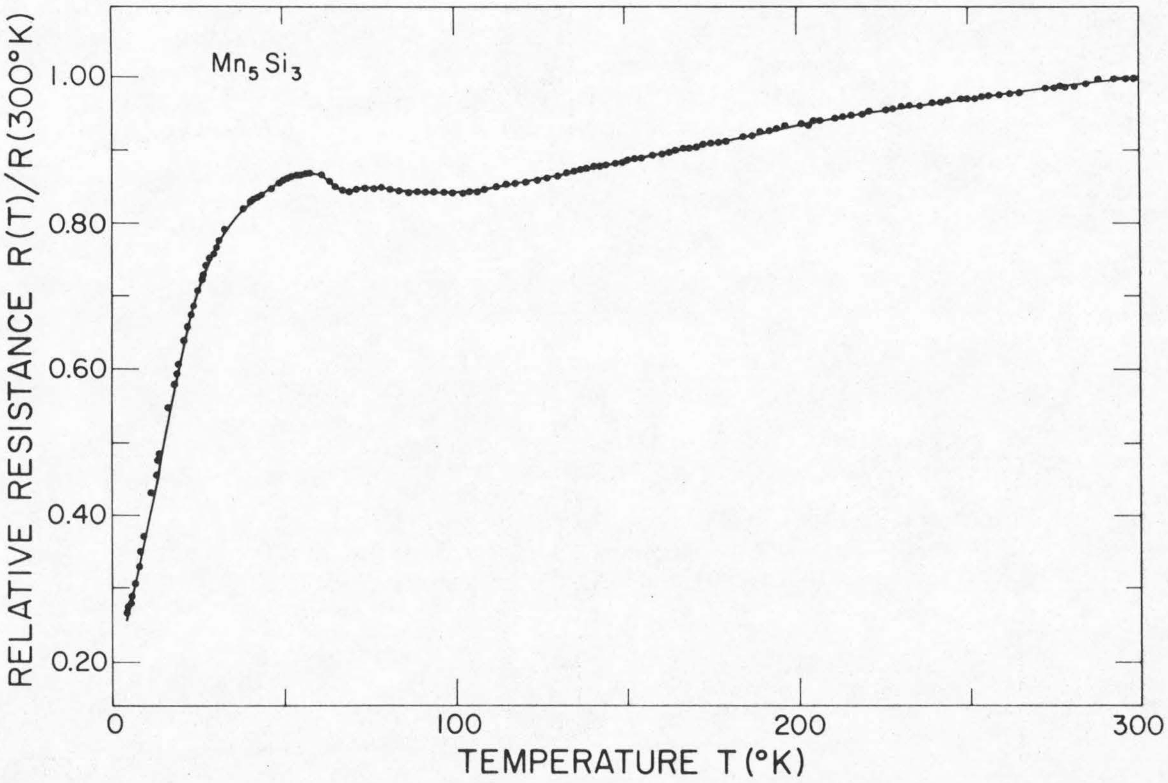

Fig. 41. Temperature dependence of relative resistance for the Mn_5Si_3 compound.

V. DISCUSSION

A. Stability of Fe_5Si_3 and the Existence of Complete Fe_5Si_3-Mn_5Si_3 Solid Solution

Discrepancies in experimental results are often due to improper techniques of the sample preparation. The Laves phase Fe_2Ti is a good example where failure to eliminate the oxygen impurity from Fe_2Ti can cause the sample to behave like a paramagnet, a ferromagnet or an antiferromagnet according to the oxygen content(45). As for the Fe_5Si_3-Mn_5Si_3 system, alloy preparation is also of great importance. As mentioned earlier, for example, second phases such as $MnAl_6$ and MnAl can result from the alumina crucible technique used in Ref. 20. This is supported by the evidence of the reported lattice parameters which, plotted as filled circles in Figs. 6 and 7, do not show a continuous variation of alloy composition. Consequently, the experimental results obtained from these samples are questionable.

1. Evidence of Second Phase

As described in the previous chapter, about 10-20% of α' phase has been identified in the Fe_5Si_3 compound. As the Mn concentration is increased, the α' phase in the $(Fe_{100-x}Mn_x)_5Si_3$ alloys decreases and it is completely unobservable when $x = 30$. Furthermore, much effort in an attempt to eliminate the α' phase in the iron-rich alloys was made in vain. Strictly speaking, therefore, the answer to the question, "Do the intermetallic compounds Fe_5Si_3 and Mn_5Si_3 form a single-phased solid solution at room temperature?" is negative. The reason for this experimental finding can be accounted for by the simple fact that the intermetallic compound Fe_5Si_3 is an equilibrium-phase only at high temperatures between 825°C and 1030°C (Fig. 8). The nature seems to be such that the rate of α' formation in these iron-rich alloys is so fast that α' phase cannot possibly be suppressed by the limited rate of quenching. Therefore, all experiments(16-18,20) performed on the Fe_5Si_3 or the iron-rich $(Fe,Mn)_5Si_3$ alloys must in principle be given reconsideration in view of the perturbations due to the presence of the α' phase in these alloys.

2. Mössbauer Spectrum Fitting and the α Factor

a. Mössbauer spectrum fitting

It has been observed in Fig. 11 that all the room temperature Mössbauer spectra are excellently fitted with a two-site approximation except those in the Fe-rich region. A closer examination of the fitting of these Fe-rich spectra indicates that the contribution due to absorption of the Fe_{II} atoms in the 4(d) site shows an excellent fitting to a single hyperfine splitting while the contribution from Fe_I in 6(g) is in fact due to a number of hyperfine fields of different magnitudes. If such is true, it is then of no surprise that a perfect fitting is not obtainable with a two-site approximation. To justify the point that the Fe atoms may actually situate at more than two sites in the Fe_5Si_3 lattice in which there are only two crystallographic sites, one may well remember the fact discussed earlier that a second phase (α') does indeed exist in the Fe-rich $(Fe,Mn)_5Si_3$ alloys. It has been previously reported that Fe_I covalently bonded to the neighboring Si atoms in the 6(g) site and the Fe_{II} atoms in the 4(d) site form metallic bonded chains$^{(17,20)}$. This is consistent with the near neighbor distances in Table VII of which detailed discussions will be presented later. In view of the relatively weaker bonding among atoms in the 6(g) site, it is perfectly reasonable that the crystallographic distortion of the atoms in the 6(g) site by the presence of the α' phase is much more probable than that of the metallic chains in the 4(d) site. This distortion of the Fe_I atoms and their environments, therefore, gives rise to a reality of multi-Fe_I sites which in turn contribute to the resultant complicated Mössbauer spectrum of the Fe_5Si_3 compound. This explains the difficulty in the Mössbauer spectrum fitting of Fe_5Si_3 with a two-site approximation. However, the fitting improves as the Mn concentration increases as can be seen in Fig. 11. This is consistent with the fact that the content of α' phase in the $(Fe_{100-x}Mn_x)_5Si_3$ alloys decreases with increasing Mn concentration. The fact that the complete solid solution of the intermetallic compounds Fe_5Si_3 and Mn_5Si_3 does not exist at low temperatures indicates that the same argument may be applied to account for the fitting difficulty of the low temperature Mössbauer absorption spectra in the Fe-rich region. This is evident in Fig. 12.

b. The α factor

As described in Chapter IV, the α factor is defined such that $W_i = W_o(1 + \alpha E_i)$, where W_i is the linewidth of the absorption peak at the Doppler velocity $V = E_i$ and W_o is the effective linewidth at $V = 0$. Since the Fe atoms in the $(Fe,Mn)_5Si_3$ alloys have in fact many sites, the hyperfine splitting of each site in a two-site model is

TABLE VII

Near neighbor distances (d) and fractional change in volume $\frac{V_I - V_{II}}{V_{II}}$ for several alloys. d^* is the weighted average of the underlined d distances.

		Fe_5Si_3			$(Fe_{90}Mn_{10})_5Si_3$			$(Fe_{50}Mn_{50})_5Si_3$			Mn_5Si_3		
Atomic Sites	Neighbors	d (A)	d* (A)	V_{eff} (A^3)	d (A)	d* (A)	V_{eff} (A^3)	d (A)	d* (A)	V_{eff} (A^3)	d (A)	d* (A)	V_{eff} (A^3)
Me_I in 6(g)	2 Si	2.349			2.358			2.381			2.403		
	1 Si	2.500			2.509			2.533			2.557		
	2 Si	2.625	2.547	8.651	2.629	2.555	8.733	2.645	2.577	8.960	2.674	2.602	9.224
	2 Me_I	2.691			2.702			2.728			2.753		
	4 Me_I	2.826			2.831			2.850			2.880		
Me_{II} in 4(d)	2 Me_{II}	2.360			2.363			2.376			2.402		
	6 Si	2.377	2.372	6.987	2.385	2.379	7.049	2.405	2.398	7.220	2.428	2.421	7.430
Si in 6(g)	2 Me_I	2.349			2.358			2.381			2.403		
	4 Me_{II}	2.377			2.385			2.405			2.428		
	1 Me_I	2.500	2.439	7.596	2.510	2.447	7.673	2.533	2.467	7.861	2.557	2.491	8.093
	2 Me_I	2.625			2.629			2.645			2.674		
	2 Si	2.719			2.725			2.742			2.771		
$\frac{V_I - V_{II}}{V_{II}}$				0.24			0.24			0.24			0.24

considered to a first approximation as the superposition of a distribution of hfs of equal isomer shift and quadrupole moment. For this purpose, the α factor is introduced as a spectrum fitting parameter. The α factor, however, does not have a physical meaning as a measure of broadening due to the multi-site effect. Nevertheless, it helps to understand the degree of disorder in an alloy. In Fig. 25, α_I and α_{II} due to Fe_I and Fe_{II}, respectively, reveal interesting compositional variations. It is easy to see that α_{II} in the Fe-rich region increases as Mn concentration increases owing to the finite probability of substitution of the Fe_{II} atoms by Mn, while the alloys studied tend to stabilize more in the $D8_8$ structure when approaching the Mn_5Si_3 composition, as indicated by the decreasing α_{II} with increasing Mn concentration in the Mn-rich region. The discontinuity in α_{II} near the composition $x = 50$ will be discussed later. The variation of α_I , on the other hand, represents a very significant effect. In spite of the fact that substitution of Fe_I by the Mn atoms would in principle increase the degree of disorder in the 6(g) site and would, therefore, cause α_I to increase with increasing Mn concentration, α_I is shown decreasing as Mn concentration increases. This may be understood by the following argument. Since the α' phase exists in the iron-rich alloys as is evident from results of the x-ray analysis (Figs. 9 and 10) the presence of the α' phase causes the disordering in the 6(g) site as shown in both the room temperature and liquid-nitrogen temperature Mössbauer spectra (Figs. 11 and 12). However, as mentioned earlier in this chapter, substitution of Fe_I by the Mn atoms helps to restore the alloys in the $D8_8$ structure. That is, the degree of disorder decreases as Mn concentration increases due to the decreasing presence of α' phase. α_I , therefore, decreases with increasing Mn concentration, and this dominates the increasing α_I effect due to incoming Mn atoms in the 6(g) site. As a result, α_I decreases as x increases. In other words, the Mn atoms that are introduced into the Fe_5Si_3 compound act partly as stabilizers of the Mn_5Si_3 type structure. This result is consistent with the fact that the Mn and Si atoms of the appropriate proportion crystallize in the $D8_8$ structure. It should be mentioned that the presence of the α' phase, of course, would definitely disturb the fitting based on a two-site approximation.

3. Stability of the $(Fe_{100-x}Mn_x)_5Si_3$ Alloy System

It is evident from the Fe-FeSi phase diagram (Fig. 8) that Fe_5Si_3 is a stable compound in a narrow high temperature range from 825°C to 1030°C. Therefore, there is no reason why a complete solid solution of the compounds Fe_5Si_3 and Mn_5Si_3 does not exist at high temperatures (between 825°C and 1030°C). The Mössbauer absorption spectra of all composition measured at $T = 423^\circ K$ show excellent fitting in two distinctive sites (Fig. 13). The fact that no difficulty was encountered in fitting the Fe-rich high temperature Mössbauer spectra in two sites suggests that a possible complete solid solution of $(Fe\text{-}Mn)_5Si_3$ alloys may even exist at temperatures as high as $T = 423^\circ K$. Although confirmation on this point would have to wait for the results of high temperature x-ray analysis, yet it is consistent enough with the fact that the $(Fe_{100-x}Mn_x)_5Si_3$ alloys tend to be more stable either as the temperature increases ($< 1030^\circ C$) or as Mn concentration increases.

B. Substitutional Preference and the Two-Site Model (TSM)

1. Relative Intensities

As described in Chapter IV, the relative absorption intensity due to Fe_{II} over Fe_{I} in the room temperature Mössbauer spectra (Fig. 19) increases slowly with increasing Mn concentration x until the composition for $x = 50$ where the ratio $Area_{II}/Area_{I}$ begins to increase exponentially with increasing x. The Mössbauer absorption intensity or the area under its spectrum is directly proportional to the product of the number of the Fe atoms (or strictly speaking Fe^{57}) and the corresponding probability of the recoilless absorption. At a constant temperature therefore, the relative intensity $Area_{II}/Area_{I}$ represents the ratio of the number of Fe atoms in site II to that in site I, if the recoilless absorption probability or f factor is the same for both sites. This suggests that in the low Mn concentration alloys there is a definite preference of Mn atoms for site I. If Mn atoms substituted randomly into the lattice, then the area ratio would be 4:6, independent of composition, since site I has six positions and site II only four.

Figure 23 shows the relative absorption intensity $Area_{II}/Area_{I}$ in the liquid-nitrogen temperature Mössbauer spectra as a function of Mn concentration. However, no substantial difference due to change in temperature is observed in values between $T = 295^{o}K$ and $T = 77^{o}K$. This indicates clearly that at temperature $T = 77^{o}K$ a saturation for both sites has well been reached in the f factor versus temperature curves, in view of the exponential dependence in temperature of the f factor. That is, in the Debye model for $T \ll \Theta_D$,

$$f = \exp\left[- \frac{E_r}{R_B \Theta_D} \left(\frac{3}{2} + \frac{\pi^2 T^2}{\Theta_D^2}\right) \right] \tag{6}$$

where Θ_D is Debye temperature and E_r is the recoil energy associated with the transition$^{(28)}$. It is thus established that at temperature $T = 77^{o}K$ the f factor is practically equal to 1 for both sites. Knowing that there are exactly 6 atoms in site I and 4 atoms in site II, one can determine from Fig. 23 or Table III the probable numbers of $Fe_I(p)$ and $Fe_{II}(q)$ atoms in the crystal lattice by solving the following two simultaneous equations (for p and q):

$$p + q = 10C_{Fe}$$

$$q/p = r \tag{81}$$

where the Fe concentration in $(Fe_{100-x}Mn_x)_5Si_3$ $C_{Fe} = (100-x)/100$ and r is given by the relative intensity $Area_{II}/Area_I$. Hence the number of Mn_I equals (6-p) and that of Mn_{II} (4-q). Numbers of Fe and Mn in each site are shown in Table VIII, in which a profound preferential substitution of Mn atoms is clearly indicated. It should be pointed out that the Debye model has been assumed in the present calculations.

The nature of the observed preferential occupation is not well understood. However, it is believed that this preferential occupation is not magnetic in origin, in view of the fact that it is also observed at room temperature where most alloys are in a paramagnetic state.

TABLE VIII

Average number of Fe and Mn atoms in each site of the $(Fe_{100-x}Mn_x)_5Si_3$ lattice (from Eq.(81) and data in Table III

Alloy	Number of Atoms			
	Fe_I	Mn_I	Fe_{II}	Mn_{II}
Fe_5Si_3	6.00	0	4.00	0
$(Fe_{90}Mn_{10})_5Si_3$	5.30	0.70	3.70	0.30
$(Fe_{80}Mn_{20})_5Si_3$	4.70	1.30	3.30	0.70
$(Fe_{70}Mn_{30})_5Si_3$	3.57	2.43	3.43	0.57
$(Fe_{60}Mn_{40})_5Si_3$	2.26	3.74	3.74	0.26
$(Fe_{50}Mn_{50})_5Si_3^*$	1.31	4.69	3.69	0.31
$(Fe_{40}Mn_{60})_5Si_3$	0.67	5.33	3.33	0.67
$(Fe_{30}Mn_{70})_5Si_3$	0.36	5.64	2.64	1.36
$(Fe_{20}Mn_{80})_5Si_3$	0.14	5.86	1.86	2.14
$(Fe_{10}Mn_{90})_5Si_3^*$	0.05	5.95	0.95	3.05
Mn_5Si_3	0	6.00	0	4.00

*Data for $(Fe_{50}Mn_{50})_5Si_3$ and $(Fe_{10}Mn_{90})_5Si_3$ are interpolated from Fig. 23.

2. The Two-Site Model (TSM)

The results discussed above can be summarized by establishing the following empirical rule for the atomic substitution:

In the $(Fe_{100-x}Mn_x)_5Si_3$ alloys, as Mn concentration x increases, the Mn atoms enter the 6(g) site (site I) first until site I is almost completely occupied at composition $x = 50$. At this composition, additional Mn atoms begin to substitute the all-Fe 4(d) site (site II). A schematic diagram (Table IX) may then be constructed for this alloy system.

C. The Lattice Constant Anomalies

The lattice parameters a and c of the $(Fe_{100-x}Mn_x)_5Si_3$ alloys were presented in Figs. 6 and 7. It was also mentioned in the previous chapter that both of these compositional dependent curves of a and c fail to follow Vegard's law(46) which allows only gradual change in the lattice constant curves. It is particularly interesting to note that both lattice parameters a and c exhibit a slope discontinuity when plotted against Mn concentration. Each of the lattice constant anomalies will be discussed in detail as follows:

1. Anomaly of Lattice Parameter a

a. Ferromagnetic transition

The interesting feature of the lattice parameter a versus Mn concentration curve shown in Fig. 6 is that it consists of two straight lines, both of positive slopes, which intersect with each other at the composition $x = 22.5$. The abrupt slope discontinuity in the vicinity

TABLE IX

The two-site model of Fe-Mn substitution in the $(Fe_{100-x}Mn_x)_5Si_3$ alloys

Mn Concentration (x)		0 - 50	50 - 100
Fe Concentration	Site I	decreases with increasing x	0
	Site II	100%	decreases with increasing x

of $x = 22.5$ amounts to a 51.9% decrease in the inreasing x direction. The fact that the $(Fe_{22.5}Mn_{77.5})_5Si_3$ alloy has a Curie temperature $T_c = 295^oK$ suggests that this lattice parameter anomaly is probably associated with the effect of the ferromagnetic transition. This may be understood as follows:

According to the Heisenberg model, as ferromagnetism results from the parallel alignment of the atomic spins, the exchange interaction $J(r)$ between neighboring magnetic atoms gives rise to a deepening of the magnetic energy levels by an amount of $-2pJ(r)S^2$ where J is a function of separation r of the magnetic atoms, S is the total spin quantum number and p is the number of nearest neighbors(47). The total energy of the alloy system can decrease further due to an increase in $J(r)$ as a result of the rearrangement of the atoms. In view of this, the lattice dimension increases or decreases depending on whether $\partial J/\partial r$ is positive or negative. The fact that the lattice parameter a decreases as the alloys transform from paramagnetic to ferromagnetic state indicates that J as a function of r is in the region where $\partial J/\partial r$ is negative. This implies that a small lattice spacing $(\propto r)$ corresponds to a large J. However, as predicted by the molecular field theory, J is directly proportional to the Curie temperature T_c, and from Eq. (55),

$$J = \frac{3k_B}{2pS(S+1)} T_c \quad . \tag{82}$$

Hence in the present case, as composition x decreases through $x = 22.5$ the lattice constant a declines substantially, since T_c increases with decreasing x (Fig. 32). It should also be pointed out that the lattice parameter c is not affected by the magnetic "transition" at x = 22.5 , however (Fig. 7). This will be explained in detail in the next section.

b. Magnetoanisotropy

It is interesting, however, to note the anisotropy of the lattice volume decrease due to ferromagnetic transition of the $(Fe_{77.5}Mn_{22.5})_5Si_3$ alloy at room temperature, in which only the basal lattice parameter a is caused to exhibit an abrupt change at x = 22.5 and the lattice constant c , on the other hand, is not affected by the corresponding phase transition. This can be seen clearly in Figs. 6 and 7. In order to try to understand this anisotropic phenomenon, a closer examination must be given to Table VII which shows the near neighbor distances for atoms in each site. These were calculated with information provided by the atomic coordinates (Fig. 5) and the corresponding lattice parameters a and c . The effective atomic volume V_{eff} in each site can be determined from the effective atomic diameter d^* which is the weighted average of the near neighbor distances of the closest "shell". Results in Table VII show that the effective volume of the metallic atom in 6(g), Me_I, is consistently 24% larger than that of Me_{II} and the latter is found to be appreciably smaller than the atomic volume of Fe or Mn determined from the lattice parameter of its pure metallic structure. In the case of the Fe_5Si_3 compound the effective atomic volume of Fe_{II} is 6.987 Å^3 which is 20% smaller than that of the pure α-Fe (8.389 Å^3), and the effective atomic volume of Mn_{II} (7.430 Å^3) in the compound Mn_5Si_3 is

15% smaller than that of the pure α-Mn (8.539 $Å^3$). It is suggested, therefore, by these appreciable atomic volume ratios that the bonding of the Me_{II} atoms in the 4(d) site of Me_5Si_3, which is in fact stronger than that in the α-Fe or α-Mn metal, is indeed of substantially higher strength than that of the Me_I atoms in the 6(g) site. Since, as described in Chapter IV, the Me_{II} atoms are tightly bonded chains extending along the c-axis, and Me_I together with the Si atoms may be thought of as filling the space accordingly in between the Me_{II} chains, any decrease in the lattice constant c would mean the compression of the Me_{II} chains. It is, therefore, evident that a volume decrease due to a magnetic phase transition is likely to cause a decrease only in the basal directions since the energy required to compress the already tightly bonded chains in the c-axis would be considerably larger than that required for a uniform compression in the basal directions. It is reasonable that in light of this a simultaneous change in slope of the lattice parameter c versus composition curve is not observed.

2. Anomaly of Lattice Parameter c

In Fig. 7, on the other hand, the lattice constant c versus Mn concentration x curve consists of two straight lines which intersect with each other at $x = 50$. It is interesting to note that the slope of the line in the low Mn concentration region is extraordinarily small compared with that in the region of high Mn concentration and the abrupt increase in slope at $x = 50$ is as high as 112.6%.

This anomaly of lattice parameter c appears to be similar to that on the lattice parameter a in the sense that they both exhibit a change in slope of the linear dependence on alloy composition, yet they are believed to be quite different in origin. To understand the anomalous behavior of lattice constant c , the two-site model is used. Based on the TSM, as the Mn concentration increases from $x = 0$ to $x = 50$, the substituting Mn atoms prefer to enter the site I, and the site II remains almost completely occupied by the Fe atoms. As a result, the lattice parameter c is only slightly increased since the tightly bonded Fe_{II} chains along the c-axis which essentially determines the lattice spacing c , stay unbroken in this composition range, and since the majority contribution of volume expansion due to the increasing number of Mn atoms (larger in volume than Fe) would naturally result in a sharp increase in the basal lattice parameter a . At $x = 50$, however, the Fe_{II} chains are beginning to break by the substituting Mn atoms entering the site II. In effect, the lattice constant c exhibits an abrupt increase at $x = 50$ due to the elongated Fe_{II}-Mn_{II} chains in the 4(d) site.

3. Slope of Lattice Constants a and c

In order to study the relative variation of the slopes of a(x) and c(x) curves, differential lattice constants $\Delta a(x) = a(x) - a(0)$ and $\Delta c(x) = c(x) - c(0)$ are defined, where x is the Mn concentration in the $(Fe_{100-x}Mn_x)_5Si_3$ alloys, and a(0) and c(0) are the lattice parameters of Fe_5Si_3. A plot of $\Delta a(x)$ and $\Delta c(x)$ against composition x is shown in Fig. 42. In essence, these are no different from the curves a(x) and c(x) shown in Figs. 6 and 7, respectively, except that they are uniformly shifted in the vertical direction so that only the net change of lattice parameters with respect to Mn concentration is

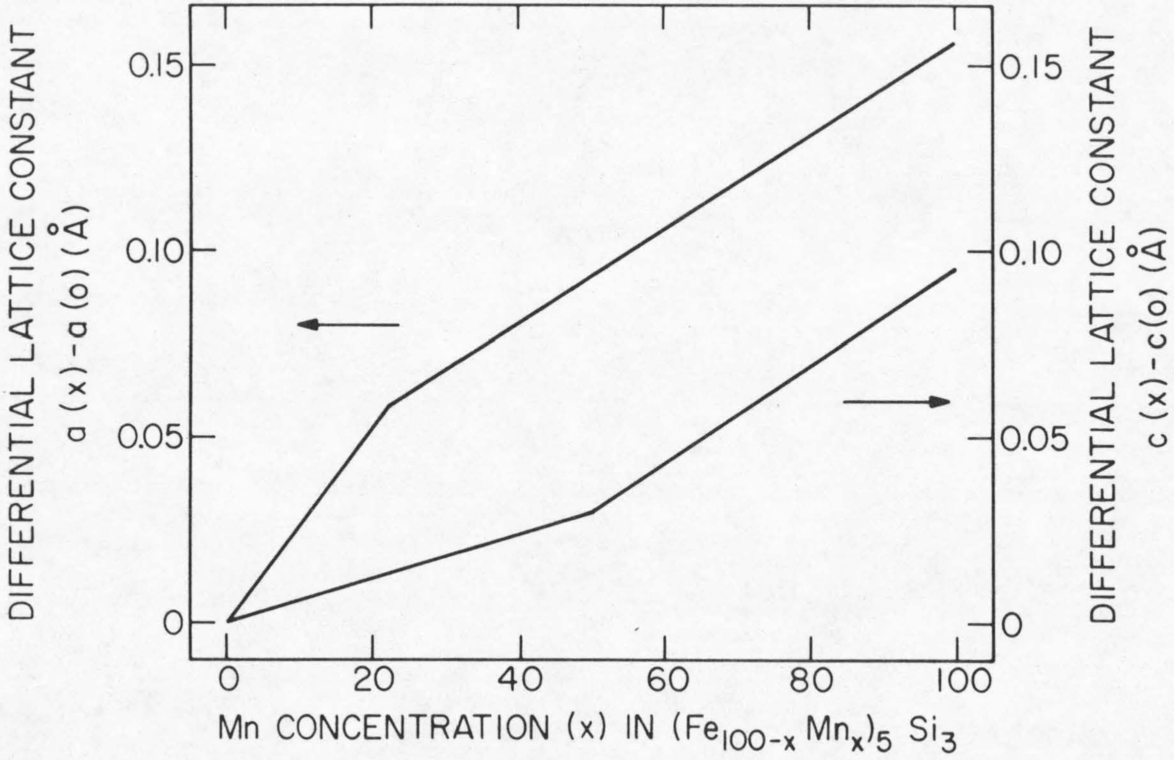

Fig. 42. Composition dependence of differential lattice constants a(x) - a(o) and c(x) - c(o).

shown. For the sake of convenience, slopes of all line segments are designated such that Sa_1 is the slope of $a(x)$ in the concentration range from $x = 0$ to $x = 22.5$, that is, $Sa_1 = Sa\ (x < 22.5)$, and such that $Sa_2 = Sa\ (x > 22.5)$, $Sc_1 = Sc\ (x < 50)$, and $Sc_2 = Sc\ (x > 50)$. Table X shows the slopes Sa_1, Sa_2, Sc_1, and Sc_2 determined from Fig. 42.

It is of interest to note from Fig. 42 or Table X as the Mn concentration x increases: a. $Sa_1 > Sa_2$, b. $Sc_1 \ll Sa_1$, and $Sc_1 \ll Sa_2$, and c. $Sc_2 = Sa_2$. These observations can be rationalized as follows.

a. $Sa_1 > Sa_2$

This is understood as an effect of the ferromagnetic phase transition which occurs at room temperature for the alloy with $x = 22.5$ (Fig. 32). This was already previously discussed in detail.

b. $Sc_1 \ll Sa_1$ and $Sc_1 \ll Sa_2$

As was also described in the discussion of anomaly of lattice parameter c, according to TSM the Mn atoms prefer to substitute Fe_I in the 6(g) site as Mn concentration increases from $x = 0$ to $x = 50$. Within this range of composition, an anisotropic volume change predominantly in basal directions is due to the fact that almost no Mn atoms enter site II causing the Fe_{II} chains to expand in the direction of the c-axis. However, small increments of c would nevertheless occur in view of the volume expansion of site I due to the substituting Mn atoms.

TABLE X

Slope of differential lattice parameters $\Delta a(x)$ and $\Delta c(x)$ determined from Fig. 42

	Slope (Å/at.% Mn)
$Sa_1(x < 22.5)$	0.0026
$Sa_2(x > 22.5)$	0.0012
$Sc_1(x < 50)$	0.0006
$Sc_2(x > 50)$	0.0012

c. $Sc_2 = Sa_2$

Calculations of the near neighbor distances shown in Table VII indicate that for all alloys the distance from the Fe_{II} to the six neighboring Si atoms (2.377 Å for Fe_5Si_3) is practically equal to that of the two nearby Fe_{II} atoms (2.360 Å for Fe_5Si_3). This is in excellent agreement with the results reported both by Amark et al.(1) and by Aronsson(4), but does not agree with the statement that Fe atoms in 4(d) are <u>far</u> from the Si atoms as reported by Lecocq(17) who gave no figures. Results of the present work suggest that to a first approximation the site II is essentially spherical. Since lattice constants a and c are directly proportional to the interatomic distances $d(Me_{II}\text{-}Si)$ and $d(Me_{II}\text{-}Me_{II})$, respectively, as x increases the lattice would expand uniformly in <u>both</u> basal (a) and vertical (c) directions if all Mn atoms are to enter the 4(d) site. According to the theory of TSM, indeed a great majority number of the substituting Mn atoms would enter the 4(d) site as Mn concentration increases from $x = 50$ to $x = 100$. Thus the slopes Sa_2 and Sc_2 are practically equal for $x > 50$.

D. The Mössbauer Effect

For the purpose of convenience, the composition dependence of hyperfine fields at $T = 77^oK$ will be treated later in detail, together with other magnetic properties. The present discussion will be limited to relative intensity, isomer shift and quadrupole splitting.

1. Relative Intensity

The relative intensity (Figs. 19 and 23), deduced from the Mössbauer absorption spectra, plays an extremely important role throughout the present work. As has been discussed, the average number of Fe and Mn atoms present in each site of a given alloy can be determined from this absorption ratio $\text{Area}_{II}/\text{Area}_{I}$. This leads to the establishment of the two-site model which has been used to explain a lattice parameter anomaly and later on will be shown useful in understanding other experimental results. Similar, but not as pronounced, effect of preferential occupation is also found in the Laves phase $(Fe_{1-x}Mn_x)_2Ti$ alloys(48). The relative intensity has clearly been proved a highly powerful technique capable of distinguishing Fe atoms, for instance, at even different crystallographic sites.

2. Isomer Shift

It is interesting to note the fact that at room temperature isomer shifts δ of both sites as functions of composition show a jump (0.025 mm/sec) as composition increases from $x = 20$ to $x = 25$ (Fig. 17). This corresponds to the composition where the magnetic hyperfine splittings vanish in the Mössbauer spectra as shown in Fig. 11. This sharp increase in δ indicates a corresponding decrease in charge density at the nucleas as the alloys transform from the ferromagnetic to paramagnetic state. A similar discontinuity in δ of the opposite direction (decreasing sharply as it undergoes a transition from the ferromagnetic to paramagnetic state) has also been observed for metallic iron(26). The isomer shift anomaly in Fe has been interpreted as arising from a shift in the Fermi level which can be obtained from a band structure calculation(49). However, as pointed out by Alexander, et al. in Ref. 49, the phonon-magnon interaction at the Curie temperature can also lead to a discontinuity in isomer shift. This mechanism may possibly account for the observed isomer shift anomalies at composition near $x = 22.5$.

Another interesting feature shown in Fig. 17 is that the isomer shifts associated with site II are substantially smaller than that of site I. This is probably due to the fact that throughout the entire alloy composition the effective atomic volume at site II is much smaller than that at site I and the latter is comparable to the atomic volume of the metallic Fe. Since reducing atomic volume can cause the "compression" of the 4s-electron wavefunction which in turn gives the consequence of increasing s electron density at the nucleus, the isomer shift decreases. Pound, et al.(50) have made an accurate measurement of the pressure dependence of isomer shift of iron, and the result obtained is

$$\frac{\Delta\delta}{\Delta P} = (-7.98 \pm 0.31) \times 10^{-5} \text{ cmsec}^{-1}\text{kbar} \qquad (83)$$

Converting Eq. (83) to volume using the compressibility of iron at low pressure $(-\Delta V/V_o \Delta P = 5.95 \times 10^{-4} \text{kbar}^{-1})$, Pipkorn and others(51) obtained

$$\frac{\Delta\delta}{\Delta\left(\frac{V}{V_o}\right)} = 1.34 \text{ mm/sec} \qquad (84)$$

If $(V/V_o) = 0.19$ (V_o being taken as the effective atomic volume at site I), $\Delta\delta$ corresponding to the volume change is then

$\Delta\delta_V = 0.25$ mm/sec . As can be seen in Fig. 17, this agrees reasonably well with the observed result that on the average δ_{II} is less than δ_I by $\Delta\delta_{obs} = 0.22$ mm/sec .

Furthermore, Si, with four valence electrons ($3s^2$ $3p^2$), is a well-known electron donor and it is quite reasonable to assume that there is a transfer of electrons from Si to Fe and Mn in the present case. This is consistent with the fact that the magnetic moment of Fe in Fe_5Si_3 is smaller than that of pure iron. In view of a band picture, practically all electrons contributed by Si fill the d-band of Fe (and Mn). Since increasing the d-electron density decreases the electronic charge density at the nucleus due to shielding effect, a positive increase in isomer shift then results. However, as pointed out by Wertheim, et al.$^{(52)}$, an increase of 0.2 electrons in the 3d shell of Fe should lead to a decrease in hyperfine field H_{hf} of about 26 kOe . Since $H_{hf_I} = 156$ kOe and $H_{hf_{II}} = 89$ kOe for Fe_5Si_3, as compared to 330 kOe for metallic Fe, the resulting increase of iron 3d electrons due to Si is 1.34 electrons for Fe_I and 1.85 electrons for Fe_{II}. This means that the corresponding increase of isomer shift caused by Si electron transfer is slightly more for Fe_{II} than for Fe_I, which in turn brings δ_{II} closer to δ_I . Hence this may account for the small discrepancy between the expected $\Delta\delta_V$ (= 0.25 mm/sec) due to volume difference and the observed isomer shift difference $\Delta\delta_{obs}$ (= 0.22 mm/sec).

The fact that the isomer shift is roughly a constant of composition reflects the similar electronic configurations of Fe and Mn atoms. However, a small change of slope does in fact occur in both δ_I and

δ_{II} at composition corresponding to $x = 50$. According to the TSM approximation, as Mn concentration x increases through $x = 50$, Mn atoms begin occupying site II, whereas the rate of occupation in site I per Mn concentration decreases sharply at $x = 50$. This might cause the electrons transferred from Si to redistribute among Fe and Mn atoms and hence affect the isomer shifts.

At the liquid-nitrogen temperature on the other hand, the isomer shift of Fe_I exhibits a large discontinuity at $x = 50$ as shown in Fig. 20. This is apparently caused by the ferro- and paramagnetic "transition" near composition $x = 50$. As will be discussed later in detail, at $T = 77^oK$ magnetic spins of Fe_I interact among themselves ferromagnetically in alloys corresponding to $x > 50$ and site I becomes nonmagnetic for $x < 50$ where 6(g) site is almost completely occupied by Mn_I according to the two-site model. The large increase in δ_I at $x = 50$ is probably due to the nonlinear temperature dependence of isomer shift (which increases with decreasing temperature)(53) and the effect due to onset of antiferromagnetism (near $x = 50$) in the 4(d) site (see later discussion). The latter is believed to be the cause of sharp increase of δ_I for compositions $x > 50$.

3. Quadrupole Splitting

It is extremely difficult to interpret the compositional variation of quadrupole splittings owing to the fact that the alloy cannot be assumed strictly ionic so that it is unclear what charge to associate with a lattice point. This becomes very much more complicated when alloying is taking place in a complex structure like

$(Fe_{100-x}Mn_x)_5Si_3$. Furthermore, the lattice sum determined by x-ray diffraction turns out to be very sensitive to small changes in the position of the ions which in reality do occur. In view of this, understanding of quadrupole splitting as a function of alloy composition is limited to being even less promising than qualitative.

However, the constant quadrupole splitting $\Delta E_{Q_{II}}$ of Fe_{II} at room temperature for $x \leq 50$ (Fig. 18) may be understood in terms of the TSM approximation. As Mn concentration x increases from $x = 0$ to $x = 50$, the Fe_{II} atoms are not disturbed by the effect of alloying. Since the nearest neighbors of Fe_{II} are $2Fe_{II}$ and 6Si which vary neither in position nor in concentration, the crystal field experienced by Fe_{II} remains essentially unaltered and consequently the quadrupole splitting is constant. As x further increases from $x = 50$, Fe_{II} begins to be substituted at random by Mn atoms causing a slight disorder (since Si are unperturbed throughout the whole composition range) in Fe_{II}'s environment. Consequently $\Delta E_{Q_{II}}$ shows a slight increase as x increases from $x = 50$.

The ΔE_{Q_I} curve with a broad minimum at approximately $x = 60$ (Fig. 18) suggests an ordering of some type taking place at this composition. In order to better understand this however, a more sound theory is yet expected.

At $T = 77^oK$, Fe_I is ferromagnetic at composition $x < 50$, and becomes nonmagnetic at composition $x > 50$ as shown in Fig. 12. The pronounced difference in ΔE_{Q_I} between $T = 295^oK$ and $T = 77^oK$ for $x < 50$ is probably due to a temperature dependent angle between the direction of magnetic hyperfine field and the symmetry axis. It is reasonable that quadrupole splitting increases with increasing Mn concentration for $x < 50$, since disorder in 6(g) increases with increasing Mn concentration x according to TSM. At the critical composition $x = 50$ the anomalous increase is believed to be caused by magnetic transition from an ordered to a disordered state. It should be noted that for composition $x > 50$ quadrupole splittings at $T = 77^{o}K$ are found to be unusually larger than those measured at $T = 295^{o}K$.

E. Magnetism in the Fe_5Si_3-Mn_5Si_3 Alloy System

As was seen previously, the two-site model plays an extremely important role in the discussion of experimental findings in both lattice constants and the Mössbauer parameters. It has been proved useful because it is simple and fundamental. Therefore, it can be expected that the TSM will help to understand some of the magnetic properties as well, since magnetism results basically from interaction among the atomic spins which in turn depend directly on the environment and its magnetic nature.

1. Hyperfine Fields and Transition Temperatures

The Curie temperature T_c and hyperfine field H_{hf} are both determined from measurements in the absence of an external field, and it is, therefore, meaningful to study one with respect to the other. On the other hand, the magnetization shown in Figs. 26 and 27 is measured in the presence of an applied field $H = 7.3$ kG, and the magnetization so obtained would not be quite the same as the atoms' own spontaneous magnetization M which by definition is the magnetic moment in zero external field. However, the magnetization versus composition curves in Figs. 26 and 27 may still serve as a qualitative indication of the magnetic state of the alloys.

a. Hyperfine fields and Curie temperatures

As described in Chapter III, the magnetic hyperfine splitting arises from the interaction of the nuclear magnetic dipole moment with the magnetic field due to the atoms' own electrons. According to Marshall and others$^{(54)}$ all the factors contributing to the magnetic field at the nucleus are proportional to the magnetic moment of the parent atom. Therefore, a plot of the hyperfine field and magnetization should have identical variation in temperature, and this has been experimentally shown to an excellent approximation$^{(55,56)}$. Hence, the hyperfine field and magnetization at a constant temperature of an alloy system plotted against composition should also exhibit identical variation.

In view of the fact that there exist in the alloys two separate hyperfine fields H_{hf_I} and $H_{hf_{II}}$ associated with sites I and II, an average of both hf fields must be used in order to relate the hf field to the average magnetization in the alloy as a whole. This averaged hf field H_{ah} has to result from H_{hf_I} and $H_{hf_{II}}$ with the weighing factors being the numbers of Fe atoms in each site. Since the hf field is a vector quantity, addition of hf fields must, therefore, be carried out using the law of cosine. According to Johnson$^{(18,57)}$, spins of Fe_I and Fe_{II} align parallelly with each other in the Fe_5Si_3 lattice. Furthermore, the two-site model predicts that the angle between $\overline{H}_{hf_I}$ and $\overline{H}_{hf_{II}}$ should not change in the Fe-rich region for the following argument: As Mn concentration increases, the Mn atoms substitute only Fe_I in 6(g) site. Since Mn_I-Mn_I distances are large relative to those of Fe_I-Mn_I and Fe_I-Fe_I (and the average Fe_I-Fe_I interaction is much stronger than that of Fe_I-Mn_I), the probability for an Fe_I to realign with a Mn_I is considered negligible. This would leave the direction of both hf fields essentially unaltered. Therefore, it is reasonable to assume for the moment that the angle between $\overline{H}_{hf_I}$ and $\overline{H}_{hf_{II}}$ be zero for all alloys corresponding to $x \leq 50$. Hence the average hf field H_{ah} can be determined from

$$H_{ah} = C_{Fe}\left(\frac{A_I H_{hf_I}}{A_I + A_{II}} + \frac{A_{II} H_{hf_{II}}}{A_I + A_{II}}\right)$$

$$= \frac{C_{Fe}}{A_I + A_{II}} (A_I H_{hf_I} + A_{II} H_{hf_{II}}) \qquad (85)$$

where C_{Fe} is the Fe concentration, and A_I and A_{II} are the spectrum intensities due to sites I and II, respectively. The reduced average hf field at $T = 77^oK$, together with the reduced Curie point, is plotted as a function of Mn concentration in Fig. 43.

Based on the molecular field theory, the reduced magnetization σ of a ferromagnet is proportional to its Curie temperature as described in Eq. (59)

$$\sigma = A_o + A_1 T_c \qquad (59)$$

where A_1 is a positive constant as given in Eq. (61). It follows

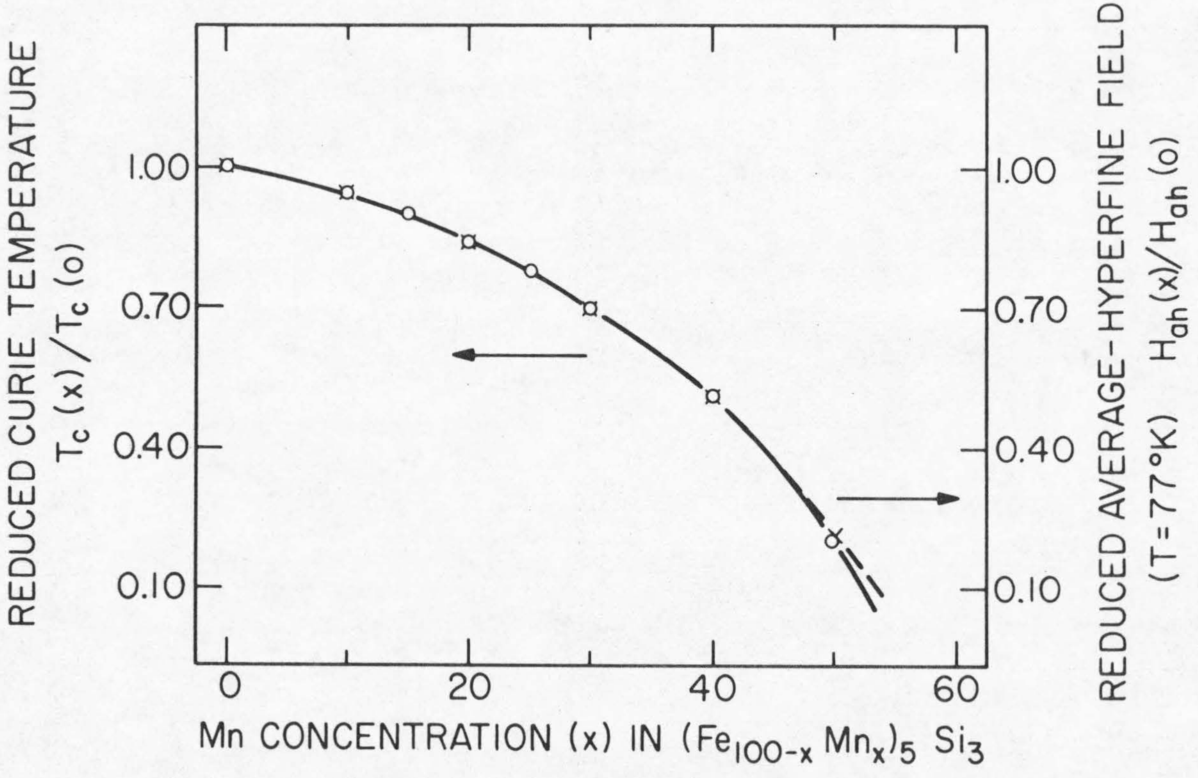

Fig. 43. Composition dependence of reduced Curie temperature $T_c(x)/T_c(o)$ and reduced average-hyperfine field at 77°K, $H_{ah}(x)/H_{ah}(o)$.

from the above discussion that the reduced averaged hyperfine field $H_{ah}(x)/H_{ah}(0)$ is proportional to the corresponding Curie point.

Figure 43 shows excellent agreement in the compositional variation of $H_{ah}(x)/H_{ah}(0)$ with $T_c(x)/T_c(0)$ except in the region of composition near $x = 50$. This indeed justifies the assumption predicted by TSM that the angle between the spins in site I and site II remains unaltered as Mn atoms gradually substitute into the Fe_5Si_3 lattice.

However, the reduced average-hf field can be seen slightly above the $T_c(x)/T_c(0)$ curve as Mn concentration approaches $x = 50$. On the basis of molecular field approximation this may be interpreted by the following argument: Since the parallel arrangement was assumed for spins of Fe_I and Fe_{II} throughout the calculations of averaged hf field, the resultant H_{ah} automatically takes on its maximum possible magnitude. Therefore, the fact that the "effective hf field" as determined by its Curie point is in fact smaller than the calculated H_{ah} suggests that the spin of Fe_I forms an angle with that of Fe_{II}. This may be readily understood in terms of the two-site model. As Mn concentration x increases from $x = 0$ to $x = 50$, only Fe_I atoms are substituted by Mn. Near the composition corresponding to $x = 50$ the minority occupant of the 6(g) site Fe_I atoms interact with their neighboring Mn_I, and as a result the spins of the Fe_I atoms deviate from their original orientation. At $x = 50$, for example, the ratio of the resultant hf field to the maximum hf field $R = 0.96$ leads to an angle $\theta \overset{\sim}{=} 32^o$ between Fe_I and Fe_{II} spin directions.

b. Hyperfine fields and Néel temperatures

Results of magnetic measurements indicate that alloys corresponding to $x \geq 50$ exhibit antiferromagnetic transitions at the low temperature, and this is evident from Fig. 32 where T_N is shown as a function of alloy composition. Therefore, well defined hyperfine splittings observed in alloys for $x = 60$, 70 and 80 at $T = 77^{\circ}K$ are consistent with the fact that the Néel temperatures for these alloys are all above the liquid-nitrogen temperature. Accordingly, the hyperfine field in these alloys should be proportional to their sublattice magnetization(47,58). Furthermore, it is interesting to note that the hyperfine field $H_{hf_{II}}$ and T_N both follow the same general variation with composition. This can be accounted for using the molecular field theory.

In a generalized molecular field theory, exchange interactions with more distant neighbors should be taken into consideration and it is essential to subdivide a given lattice into many sublattices according to their neighboring distances. The molecular field coefficient ξ, as described in Chapter III, is therefore an $n \times n$ matrix where n is the number of sublattices. Such complicated analysis may become unnecessary, however, and without loss of generality a two-sublattice model may be adopted instead. This can be justified by the fact that in view of the structure of the Me_5Si_3 lattice the Me_{II} chains are "shielded" along the c-axis by the Si tetrahedrons, and the Me_{II}-Me_I interactions may be considered negligible compared with the interactions among Me_{II} atoms along each linear chain and, therefore, that the Me_5Si_3 lattice may be approximated magnetically by a one-dimensional arrangement of antiparallel spins.

Based on the two-sublattice model of the molecular field theory, it is predicted that the Néel temperature T_N is proportional to the absolute value of exchange interaction J and, therefore, the magnetization of the two sublattices. This has been illustrated in Eq. (75),

$$\sigma_s = A_o + A_1 T_N \quad , \qquad (75)$$

where σ_s is the sublattice magnetization and A_1 is a positive constant (Eq. (61)). Since the hyperfine field of these antiferromagnetic alloys ($x \geq 50$) is proportional to the corresponding sublattice magnetization, a direct proportionality is, therefore, established between the Néel temperature T_N and the hyperfine field. From Figs. 24 and 32, it is evident that H_{hf} (for $x \geq 50$) and T_N vary consistently with composition.

c. Composition dependence of T_N and H_{hf} ($x \geq 60$)

It should be noted that the Néel temperature T_N, unlike T_c, varies rather gradually with alloy composition, and that no substantial change in T_N is observed even when 40% of the total Mn content in Mn_5Si_3 is substituted by Fe atoms. It may help to understand this by use of the two-site model.

As Fe concentration increases, according to TSM, the Mn_{II} atoms in 4(d) site are substituted by the Fe atoms. This means that the Mn_{II} chains are being "broken" as Fe atoms take place in the 4(d) site of the Mn_5Si_3 lattice. However, the Mössbauer spectra for the Mn-rich alloys show no hyperfine splittings corresponding to 6(g) site even below the bulk Néel temperatures. This indicates that the Me_I atoms in 6(g), being paramagnetic(59,60) contribute zero net magnetic moment in view of the Marshall's equation(54). Hence magnetically these alloys (for $x \geq 60$) are in effect substantially no different from Mn_5Si_3, since these Mn-rich $(Fe,Mn)_5Si_3$ alloys may be viewed approximately as "clusters" of Mn_5Si_3 compound. It thus follows that the Néel temperature does not exhibit substantial variation with Fe concentration in the Mn-rich region.

2. Intermediate Magnetic State

It should be pointed out that alloys near the composition $x = 50$ have been overlooked in the past(20). However, results of the present study have revealed that this is indeed an interesting composition, and therefore it should deserve special attention.

First of all, it is important to note that near this composition site I is almost filled with the substituting Mn and a substantial number of Mn atoms begin to occupy site II as Mn concentration x increases (Fig. 23). As a result, the Fe_{II} chains begin to "break" (Fig. 5) near $x = 50$ as Mn atoms are introduced into the lattice. In the two-site model, it is this composition that divides the substituting rule in two parts (Table IX).

Secondly, it is at this composition where the lattice parameter c versus composition curve exhibits a 112.6% increase in slope (Fig. 7). This has been explained in terms of the TSM.

Thirdly, also near $x = 50$ the hf field H_{hf_I} decreases sharply with increasing x and vanishes at about $x = 52$ (Figs. 12 and 24). The fact that Mössbauer spectra of alloys for $x > 52$ show no hyperfine splittings at a temperature $T < T_N$ indicates that 6(g) site contributes zero net moment(28,54) and therefore is in paramagnetic state even below the bulk Néel points. Composition dependence of $H_{hf_{II}}$, on the other hand, exhibits a sharp minimum at $x = 50$ (Fig. 24). According to the TSM, for $x < 50$ the 6(g) site is completely occupied by the Fe atoms and since Fe_{II} atoms are "shielded" from Fe_I and Mn_I by Si atoms, the Fe_{II}-Mn_I interaction is negligible compared with that between Fe_{II} atoms in the same site. Therefore, site II remains ferromagnetic for $x < 50$. It has been described earlier that as Mn atoms begin to occupy site II at $x = 50$ (according to TSM) antiferromagnetism becomes evident in site II (for $x > 50$). Hence this interesting minimum in $H_{hf_{II}}$ suggests that a transition between the ferro- and antiferromagnetic states may take place in 4(d) site at $x = 50$. Similar anomalies at $x = 50$ can be seen in several Mössbauer parameters such as α_{II} (Fig. 25) quadrupole splitting of Fe_I (Fig. 21), isomer shift of Fe_I (Fig. 20) and linewidth of Fe_I (Fig. 22) all at $T = 77^oK$.

Fourthly, it is interesting to note that both transition temperatures T_c and T_N decrease sharply as composition $x = 50$ is approached from either side, and also near this composition T_c and T_N curves intersect each other (Fig. 32). Furthermore, a T_c and a T_N are both observed in the $(Fe_{50}Mn_{50})_5Si_3$ alloy (Figs. 30 and 32). All these suggest that a gradual but definite magnetic transition occurs in the alloys near x = 50 . In part this may be justified by the earlier results that the directions of the Fe_I and Fe_{II} spins appear to deviate from each other as Mn concentration increases to x = 50 . This is believed to account partly for the ferrimagnetism in these alloys as a whole.

Finally, and again at x = 50 , the temperature variation of relative resistance $R(T)/R(300^oK)$ appears to deviate from its normal behavior as in the Fe-rich alloys (Figs. 35 and 36). As x increases a more pronounced relative resistance anomaly becomes evident (Figs. 37-39). This will be discussed later in detail.

In summary, x = 50 is a composition of transition.

3. The Magnetic Structure of Mn_5Si_3

Unlike the case of a ferromagnetic compound, the spin structure of an antiferromagnetic lattice can sometimes be very sophisticated(22), and the degree of complication generally increases with the size of the unit cell as well as the number of sublattices in each unit cell. In the present case of the Mn_5Si_3 compound, there are 16 atoms and two sublattices per unit cell, and it is easy to see the complication of its magnetic structure.

Lander and others(19) proposed a spin model for Mn_5Si_3 which consists essentially of three antiparallel spin pairs all in the basal plane. One of the three pairs is located at (1/3, 2/3, z) and (-1/3, -2/3, z) in the 4(d) site with the antiparallel spins directed perpendicular to the line joining these two points. The other two oppositely directed spin pairs are situated in the 6(g) site in which there are six positions available. This leaves two Mn_I atoms in the 6(g) site with zero magnetic moment. According to Lander et al., in the same 6(g) site only four Mn_I atoms carry magnetic moment and the other two Mn_I atoms are non-magnetic. However, this is not physical in view of the fact that all six Mn_I atoms in the 6(g) site are crystallographically equivalent or indistinguishable$^{(23)}$.

However, results of the present work show that the 6(g) site contributes zero hyperfine field for $x > 50$. This suggests that the relaxation in 6(g) site is so fast that each Mn_I atom probably carries an average of zero magnetic moment and the only antiferromagnetic contribution to Mn_5Si_3 is due to the antiparallel ordering of its Mn_{II} spins in the 4(d) site.

It should be pointed out, however, that no effort was made to propose a new spin model and results of the present work should only serve as hints in determination of a more realistic magnetic structure for the antiferromagnetic Mn_5Si_3 compound.

4. Magnetic States

To conclude the discussion of magnetic properties of the Fe_5Si_3-Mn_5Si_3 system, the sublattice magnetic states relative to alloy composition are summarized in Table XI.

It is particularly interesting to note the magnetic states in relation to the two-site model. That is, as Fe_I are being substituted by Mn atoms (from $x = 0$ to $x = 50 - \varepsilon$), both sites are ferromagnetic; as Mn atoms begin to occupy the 4(d) site ($x = 50 \pm \varepsilon$), the Fe_{II} chains are "broken" and the 4(d) site exhibits ferrimagnetism, whereas

TABLE XI

Magnetic state in 6(g) and 4(d) sites of the $(Fe_{100-x}Mn_x)_5Si_3$ alloys

Alloy Composition	Fe-rich region x < 50	$x = 50 \pm \varepsilon^*$	Mn-rich region x > 50
6(g) (Site I)	ferromagnetic	ferromagnetic	paramagnetic
4(d) (Site II)	ferromagnetic	ferrimagnetic	antiferromagnetic

$^*\varepsilon$ is a small number.

the 6(g) site remains in the same magnetic state; as Mn atoms further substitute Fe_{II} (from $x = 50+\varepsilon$ to $x = 100$) the 4(d) site transforms into the antiferromagnetic state while the 6(g) site is nonmagnetic.

F. Electrical Resistance

As pointed out earlier, it was extremely difficult to prepare samples of regular dimensions (uniform cross-section) due to the unusual brittleness of these alloys. Consequently, the absolute electrical resistivities cannot be determined with satisfactory accuracy. For this reason, analysis of electrical resistance throughout the present work has been carried out in terms of the relative resistance with respect to its room temperature value $R(300^{\circ}K)$. Despite the fact just mentioned, the relative resistance $R(T)/R(300^{\circ}K)$, being numerically identical to the corresponding relative resistivity $\rho(T)/\rho(300^{\circ}K)$, nevertheless provides valuable insight with regard to the electrical properties of the alloys studied.

1. Fe-Rich Alloys

a. Residual and lattice resistances

It is clear from the general temperature dependence of the relative resistance for the Fe-rich alloys (Figs. 33-35) that the total $R(T)/R(300^{\circ}K)$ (for $x < 50$) can be written similarly to Eq. (76),

$$\frac{R(T)}{R(300^{\circ}K)} = \frac{R_i}{R(300^{\circ}K)} + \frac{R_L(T)}{R(300^{\circ}K)} \tag{86}$$

where the impurity term $R_i/R(300^oK)$ is independent of temperature and the lattice contribution $R_L(T)/R(300^oK)$ varies with temperature in approximately the same way for all alloys. $R_i/R(300^oK)$ arises from scattering of the electron waves by impurity atoms which disturb the periodicity of the lattice and therefore increases rapidly with increasing Mn concentration. $R_i/R(300^oK)$ can be determined by extrapolating $R(T)/R(300^oK)$ to $T = 0^oK$. $R_L(T)/R(300^oK)$ due to thermal vibration of the lattice depends greatly on temperature and vanishes as temperature approaches $T = 0^oK$.

b. Temperature variation

Temperature variation of $R_L(T)/R(300^oK)$ in Eq. (86) is found to agree well with the Bloch-Grüneisen relation$^{(42)}$,

$$\frac{R_L(T)}{R(300^oK)} = \frac{k}{\theta_R^2} TG(\frac{\theta_R}{T}) \qquad (87)$$

where k is a constant, θ_R is a temperature characteristic of the solid's lattice resistance in the same way as is the Debye temperature θ_D characteristic of the lattice specific heat, and

$$G(z) = \frac{4}{z^4}\int_0^z \frac{s^5 ds}{(e^s-1)(1-e^{-s})} \qquad (78)$$

which approaches 1 for $z \ll 1$ and is proportional to z^{-4} for $z \gg 1$. In the case of Fe_5Si_3 (Fig. 33), the lattice resistance ratio $R_L(T)/R(300^oK)$ varies as T^5 at temperatures between $T = 40^oK$ and $T = 55^oK$ and becomes directly proportional to T at high temperatures $T > 75^oK$. As for the $(Fe_{70}Mn_{30})_5Si_3$ alloy, the T^5 law is followed in the temperature range from $T = 10^oK$ to $T = 30^oK$ and the linear T dependence occurs at $T > 155^oK$ (Fig. 34).

However, a gradual discontinuity occurs in the linear portion of the $R(T)/R(300^oK)$ slope for both $(Fe_{70}Mn_{30})_5Si_3$ and $(Fe_{60}Mn_{40})_5Si_3$ alloys. These slope discontinuities take place at $T = 252^oK$ for $x = 30$ and at $T = 199^oK$ for $x = 40$, which are consistent with the Curie temperatures determined from results of the inductance bridge and magnetic measurements, respectively. The general feature of temperature variation of the relative resistance around these critical temperatures resembles that of a typical ferromagnetic iron around its Curie point$^{(61)}$.

The electrical resistance curves of the $(Fe_{60}Mn_{40})_5Si_3$ and $(Fe_{70}Mn_{30})_5Si_3$ alloys (Figs. 34 and 35), shown with a change in slope at $T = T_c$, indicate that the resistance is relatively large at temperatures above T_c and drops significantly below T_c where the Bloch-Grüneisen relation may be applied to express its temperature variation. This, as in a typical ferromagnet such as Gd or Fe, is due to the spin-disorder scattering where electron waves are scattered by the thermally disordered spins thereby resulting in a large almost-temperature-independent resistance at temperatures above T_c, and where the spins are magnetically ordered below T_c, and hence $R(T)/R(300^oK)$ drops substantially. Since all Fe-rich alloys are ferromagnetic possessing localized moments, a change in slope of $R(T)/R(300^oK)$ is believed to occur at $T = T_c$ for alloys corresponding to $x = 0$, 10 and 20 which was not observed owing to the fact that the resistance measurements above room temperature were not carried out.

c. Debye characteristic temperature θ_R

The characteristic temperature θ_R determined by fitting $\rho(T)$ to the Bloch-Grüneisen relation (Eq. (77)) is generally found slightly different from the Debye temperature θ_D (62). The explanation for this is the following. In the derivation of Eq. (77), Bloch made several assumptions (63-65). First and foremost, was the neglecting of Unklapp processes, and Ziman (66), in carrying out a numerical calculation using a suitably defined function for U processes, found that in the case of the electrical resistivity the result of his computation was essentially the same as Eq. (77) except that the effective θ_R was then slightly less than the Debye (specific heat) temperature. The second approximation took place in the variation trail function, and Kohler (67,68) and Sondheimer (69) have demonstrated with true variation calculations that Eq. (77) is correct at all temperatures, although near $T = 0.1\ \theta_R$ the Bloch-Grüneisen formula overestimates $\rho(T)$ by about 10 percent. In spite of these approximations among others, the discrepancies between θ_R and θ_D are nevertheless generally fairly small (62).

In order to determine the characteristic temperature θ_R, a simple useful formula may be deduced from Eq. (87). At high temperatures, as $T \to \infty$, $G(\theta_R/T_h) \to 1$ and

$$\frac{R(T_h)}{R(300^{o}K)} \longrightarrow \frac{kT_h}{\theta_R^2} \quad . \tag{88}$$

But at low temperatures $(T < 0.1\ \theta_R)$, $G(\theta_R/T_\ell) \to 497.6(\frac{T_\ell}{\theta_R})^4$ so that

$$\frac{R(T_\ell)}{R(300^\circ K)} \longrightarrow \frac{497.6\ k}{\theta_R^6} T_\ell^5 \quad . \tag{89}$$

With k and θ_R assumed constant from one temperature region to the other, θ_R can be written in terms of its resistance ratio as follows:

$$\theta_R = T_\ell \left[497.6 \frac{T_\ell}{T_h} \cdot \frac{R(T_\ell)}{R(T_h)} \right]^{1/4} \quad . \tag{90}$$

The characteristic temperatures θ_R for Fe_5Si_3, $(Fe_{70}Mn_{30})_5Si_3$ and $(Fe_{60}Mn_{40})_5Si_3$, for example, are $\theta_R = 237.5^\circ K$, $\theta_R = 54^\circ K$, and $\theta_R = 45.8^\circ K$, respectively. It should be noted that θ_R decreases rapidly as Mn concentration x increases.

2. Mn-Rich Alloys

a. Antiferromagnetic Brillouin zone and its effect on electrical resistance

For a ferromagnetic metal, the periodicity exhibited by the magnetic ordering at temperature $T < T_c$ is identical to that of its crystal lattice provided a constant structure is preserved throughout the temperature range of interest. For an antiferromagnet, on the other hand, the periodicity of the exchange field will change at the transition and in fact will increase as temperature decreases through T_N since there exists more than one magnetic sublattice. Furthermore, the antiferromagnetic Brillouin zones, whose boundaries are defined by the energy gaps or the discontinuities in the dispersion relation E(k), appear to lie inside the normal Brillouin zones of the crystal lattice. These magnetic superzone boundaries are believed to have a profound effect on the electrical resistance, since the conduction electrons can be scattered not only by impurities and phonons but also by any disorder in the ionic magnetic moments. It has been pointed out that due to this effect the antiferromagnetic metals might exhibit electrical resistivity phenomena which are never present in the ferromagnets (70,71).

b. The resistive anomaly in Mn_5Si_3

As described earlier and also can be seen from Fig. 41, the temperature variation of electrical resistance in Mn_5Si_3 is extremely abnormal. In view of the fact that the intermetallic compound Mn_5Si_3 is structurally identical to Fe_5Si_3 in which the temperature-dependent electrical resistance was shown to behave ideally as in a smple metal below T_c, the resistive anomaly observed in Mn_5Si_3 therefore cannot be accounted for by the mechanism due only to electron-phonon interactions, and additional contributions must be taken into consideration.

Figure 41 has revealed an interesting fact that a relative minimum of $R(T)/R(300^\circ K)$ occurs near the Néel temperature of the compound and as temperature decreases the relative resistance, after reaching a gradual maximum at $T = 56^\circ K$, drops extremely rapidly. This apparently suggests that the anomalous temperature dependence of $R(T)/R(300^\circ K)$ in Mn_5Si_3 results from its antiferromagnetism.

The observed resistance anomaly in Mn_5Si_3 may be explained in terms of two contributions in addition to those due to impurity and electron-phonon interactions. The first contribution arises from the spin-disorder mechanism. As in a ferromagnet such as Gd, the resistance of the antiferromagnetic Mn_5Si_3 is large and approximately constant of temperature at $T > T_N$. However, as temperature decreases through its transition point, the resistance drops rapidly. Such a relative resistance curve, together with impurity and electron-phonon contributions, is plotted against the reduced temperature T/T_N in Fig. 44a. The second contribution is due to the effect of antiferromagnetic Brillouin zones described earlier. According to Overhauser(72), these superzone planes always lie close to the Fermi surface and will presumably cause an increase in the effective mass of the conduction electrons and, therefore, an increase in electrical resistance. Furthermore, the temperature dependence of the energy gaps across these zone boundaries must bear a similar form to that of the neutron scattering intensity $F(T)$. Experimentally, $F(T)$ can be fitted to a Brillouin function(73). Whether the magnetic zone effects operate through a change in effective mass or through a change in area of the Fermi surface, all contributions to resistance will be multiplied by the factor $F(T)$. The relative resistance due to antiferromagnetic Brillouin zone effect $R_{af}(T)/R(300^\circ K)$ as a function of T/T_N is shown in Fig. 44c. Hence the total relative resistance is the sum of $R_o(T)/R(300^\circ K)$ and $R_{af}(T)/R(300^\circ K)$ as shown in Fig. 44d.

Comparison of curves in Figs. 41 and 44d shows good agreement, particularly in the relative minimum and maximum near $T = T_N$ as well as in its rapid decrease at low temperatures. This explains the resistance anomaly in Mn_5Si_3.

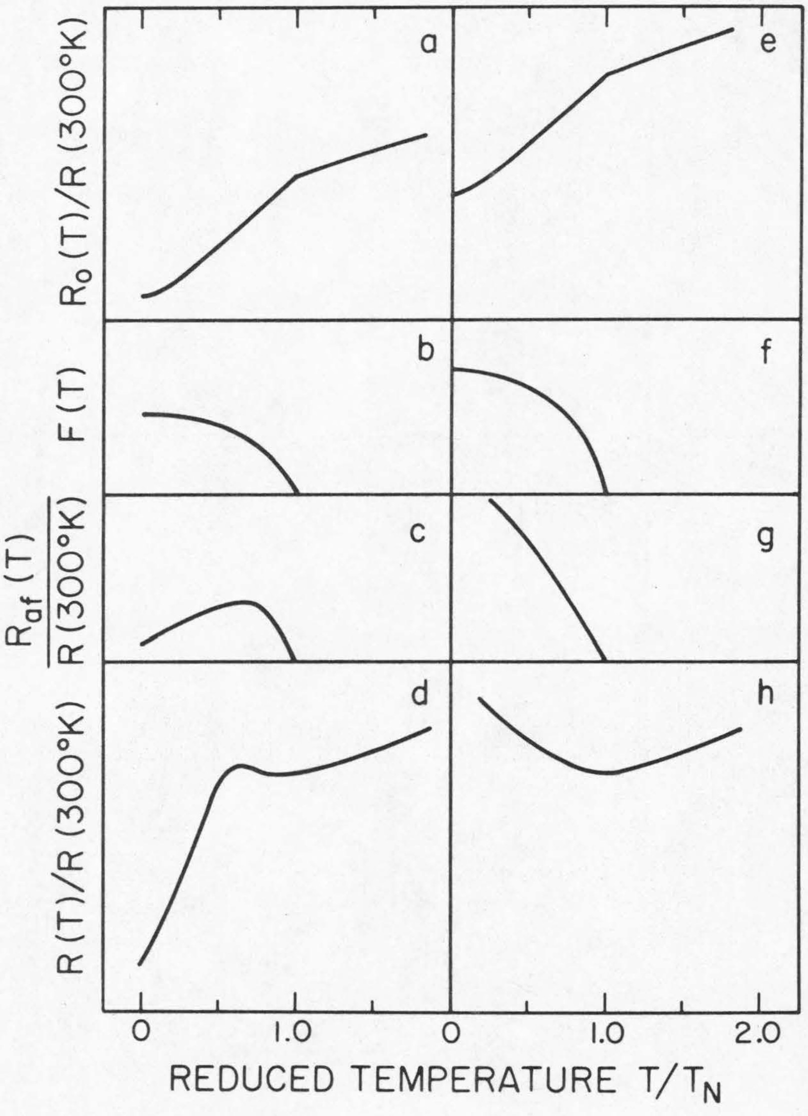

Fig. 44. Reduced temperature dependence (where T_N is the magnetic ordering temperature) of: (a) relative resistance of a typical ferromagnetic material with low impurity scattering; (b) resistance enhancement factor F(t) (see text); (c) resistance contribution due to antiferromagnetic Brillouin zone effect; (d) total relative resistance. In (e), (f), (g) and (h) are corresponding curves for a magnetic material with high impurity scattering.

The fact that a great resemblance exists in the temperature dependence of electrical resistance of Mn_5Si_3 to that of α-Mn$^{(74)}$ suggests that effect of alloying by Si atoms affects the conduction of electrons only indirectly through a depressed Néel temperature and an increased degree of lattice imperfection and that even with 37.5 at.% Si present Mn atoms dominate the conduction of electrons in Mn_5Si_3 .

c. Anomalous resistive minima in Mn-rich alloys ($x = 50,60,\cdots,90$)

As can be seen from Figs. 36-39, with only 6.25 at.% Fe added to Mn_5Si_3 (corresponding to $x = 90$), the relative resistance exhibits an interesting minimum near the Néel temperature. It is speculated that this phenomenon probably occurs in even more dilute Fe alloys, although no alloys were made in the composition range between $x = 90$ and $x = 100$. As Fe concentration increases, the minimum remains until composition $x = 50$ where only a gradual minimum is observed. Furthermore, in the vicinity of T_{min} , the relative resistance varies as T^2 (Fig. 40). This immediately eliminates the Kondo effect as a possible mechanism in which the $\log T$ dependence is characteristic at low temperatures. These resistance minima appear to be entirely different from the anomaly observed in Mn_5Si_3 , yet a closer examination shows that these phenomena result from basically the same mechanism. As Fe is added to Mn_5Si_3, due to alloying effect the residual resistance increases rapidly causing $R_o(T)/R(300^\circ K)$ to shift upward, and the energy gap or $F(T)$ increases presumably due to the same effect (Fig.

44e,f). Consequently, the antiferromagnetic superzone contribution $R_{af}(T)/R(300^oK)$ increases rapidly as temperature decreases from T_N, and hence a resistance minimum results (Fig. 44g,h).

As more Fe is introduced into the lattice (for $x > 50$), Fe atoms continue to enter the 4(d) site and it would mean further breaking of the Mn_{II} chains. Magnetically, these alloys are not significantly different from Mn_5Si_3. Hence a similar temperature variation is expected in the relative resistance minimum for each of these alloys.

$(Fe_{50}Mn_{50})_5Si_3$ (at $x = 50$) has a little different situation, however. The 4(d) site at this composition is close to being almost filled by Fe_{II} atoms, and results of magnetic measurements show that there exists a ferromagnetic as well as an antiferromagnetic transition in this alloy. The fact that the Curie and Néel temperatures are close to each other explains the relatively broad minimum in its resistance curve. The less pronounced minimum feature observed in Fig. 36 can be accounted for by the fact that the Néel temperature is rather low.

G. Suggestions on Further Studies

In order both to better understand the physics of the Fe_5Si_3-Mn_5Si_3 alloy system and to confirm some of the theories established in the present investigation, further studies may be carried out. They are, to name a few, listed in the following.

1. X-Ray Diffraction

a. High temperature work

According to the earlier discussion, a second phase (α') exists in the Fe-rich alloys as indicated by the broadened background of the (211) line (Fig. 9), and it has been suggested that this second phase tends to vanish as temperature is increased. This may, therefore, be confirmed by the possibility that the broad background under the (211) line may diminish at higher temperatures.

b. Low temperature work

It has been shown in the present investigation that the anomaly in the (room temperature) lattice parameter a curve is probably due to the ferromagnetic transition in the alloys for $x \leq 22.5$. This can be confirmed by the x-ray diffraction technique at several low temperature points, say, for $295^{\circ}K > T > 70^{\circ}K$. The anomaly in a will probably shift in composition according to the Curie temperature curve (Fig. 32), while the anomaly in lattice constant c is not expected to deviate from composition $x = 50$ at various temperatures.

2. Magnetic Measurements of Alloys near Composition $x = 50$

As discussed in the text, alloys near composition $x = 50$ deserve special attention since these are generally in an intermediate magnetic state. That two different magnetic transitions may occur consecutively in these alloys is possible in view of the transition temperature curves in Fig. 32. It would be interesting to study the order of these transitions and their effects on other properties such as specific heats and magnetic hyperfine fields.

3. Specific Heats in Alloys near Composition $x = 50$

Since the specific heat is directly related to entropy in a system, the heat capacity therefore is greatly affected by any structural or magnetic order-disorder transformations taking place in these alloys. Any such transition will in general show profound effects in the specific heats.

4. Low Temperature Mössbauer Effect

a. Near composition $x = 50$

Near this composition, the hyperfine field in site I H_{hf_I} decreases sharply to zero, whereas $H_{hf_{II}}$ of the Fe-rich and the Mn-rich alloys intersect each other with a minimum which is apparently due to the different magnetic states (namely ferro- and antiferromagnetic states) approaching from each direction. At low temperatures, say, $T = 4.2^o$, $H_{hf_{II}}$ would be sufficiently large for accurate measurement and it should be interesting to study its composition dependence. For hf fields in site I, on the other hand, it should be extremely rewarding to study its composition variation for alloy composition x slightly greater than 50. This will provide valuable insight on the magnetic state in a microscopic point of view.

b. Dilute $(Fe\underline{Mn})_5Si_3$ alloys

With enriched Fe^{57} as impurities in these Mn-rich alloys, Mössbauer spectra may be obtained with reasonable statistics. That zero hf field probably at even very low temperatures exists in 6(g) site of these alloys will further confirm the proposed magnetic model for Mn_5Si_3 in which Mn_{II} in 4(d) site are solely responsible for its antiferromagnetism.

5. Neutron Diffraction

Neutrons, unlike x-rays, are sensitive to the localized spins in alloys. Because of this, it would be extremely worthwhile performing neutron diffraction in all of these alloys. Special interest should be centered at compositions near $x = 50$ in regard to the spin ordering in each individual site as well as with respect to each other.

6. Electrical Resistance

a. Absolute resistivity measurement

Additional effort should be made with respect to sample preparation in order to obtain absolute resistivity ρ of all alloys. A plot of ρ against alloy composition can show whether or not an order-disorder transformation is present in alloys especially near $x = 50$.

b. Impurity scattering due to Fe atoms in Mn-rich alloys

It would be interesting to study the impurity effect due to addition of Fe in $(Fe\underline{Mn})_5Si_3$ alloys. It is expected that addition of only small quantities of Fe would give rise to the resistance minimum anomaly. In view of the fact that Mn atoms dominantly control the mobility of conduction electrons in Mn_5Si_3, it would be equally interesting to study the alloying effect in dilute $Fe\underline{Mn}$ alloys, and in fact, the reduced temperature dependence (T/T_N) of electrical resistance in $Fe\underline{Mn}$ is expected to resemble that in $(Fe\underline{Mn})_5Si_3$ alloys.

VI. SUMMARY AND CONCLUSIONS

The subject of this study is concerned with the lattice parameter anomalies and the magnetic states in the Fe_5Si_3-Mn_5Si_3 alloys. These alloys can be obtained by solid state quenching from high temperatures.

It has been found in the present investigation that, contrary to earlier reports, the intermetallic compounds Fe_5Si_3 and Mn_5Si_3, strictly speaking, do not form a complete solid solution. X-ray diffraction analysis indicates that a second phase α' exists in the Fe-rich alloys. As expected from the phase diagrams of Fe-Si and Mn-Si, the stability of these alloys increases rapidly as small amounts of Mn are added to the alloys or as temperature increases.

Results of the Mössbauer studies indicate that, when Fe atoms are replaced by Mn atoms, the latter prefer to occupy the 6(g) site (site I) until it is almost completely filled by Mn, and this leads to the introduction of a simple physical model known as the two-site model (TSM). It is found that the observed anomaly in the lattice constant c curve indeed can be accounted for by the effect of Fe_{II}-chain-breaking in terms of the two-site model. The slope anomaly of the lattice parameter a, on the other hand, is due to the effect of ferromagnetic ordering which causes a change in the separation of the magnetic atoms and hence the lattice spacing. Furthermore, the relative slope of the lattice constant curves a and c as functions of alloy composition can also be interpreted using the TSM.

The effect of alloying on the magnetic states in this alloy system has been studied. The reduced magnetization of these alloys deduced from magnetic hyperfine splittings has been correlated with the magnetic transition temperatures in terms of the molecular field theory. The Mössbauer effect and magnetization measurements reveal that for composition $0 \leq x < 50$ both sites I and II are ferromagnetic at the liquid-nitrogen temperature and possess moments parallel to each other. In the composition range $50 < x \leq 100$, the site II is antiferromagnetic, whereas site I is paramagnetic even at a temperature below the bulk Néel temperatures. In the vicinity of $x = 50$, however, site II is in a state of transition between ferromagnetism and antiferromagnetism. It appears from results of the transition temperature and magnetization measurements that a transition between ferromagnetic and antiferromagnetic states seems to take place in alloys in the neighborhood of $x = 50$ composition. The present study also suggests that only Mn atoms in site II are responsible for the antiferromagnetism in Mn_5Si_3 contrary to a previous report.

Electrical resistance has also been measured as a function of temperature and composition. For the Fe-rich alloys ($x < 50$) below the Curie temperatures it can be described reasonably well by the Bloch-Grüneisen equation. The resistive anomalies observed in the Mn-rich alloys are believed to arise from the interactions of conduction electrons with the antiferromagnetic superzones.

It should be pointed out that, in view of the complicated nature of this alloy system, the simple two-site model has been found surprisingly useful in understanding much of the experimental findings. These include mainly the lattice anomalies, the magnetic states and to some extent the resistive anomalies.

As to the future work, one may suggest the following: (1) Low temperature x-ray diffraction should be carried out to confirm the proposed origin of the anomaly in lattice parameter a. It is expected that at a lower temperature a similar slope discontinuity would occur however at a higher Mn concentration, while anomaly in lattice constant c should exhibit no compositional variation. (2) The composition $x = 50$ is particularly interesting structurally as well as magnetically. An even better understanding may be achieved by preparing more alloys near this composition and by measuring their magnetic and electrical properties. (3) It would also be interesting to study how the temperature dependence of the electrical resistance changes as a small amount of Fe (i.e., $90 < x < 100$) is added to Mn_5Si_3. (4) Finally, it should be emphasized that neutron diffraction experiments would be particularly worthwhile in order to confirm the present theory of magnetism in this alloy system especially in the neighborhood of $x = 50$.

REFERENCES

1. K. Amark, B. Boren and A. Westgren, Metallwirtschaft 15, 835 (1936).
2. B. Aronsson, Acta Chem. Scand. 12, 308 (1958).
3. N.F.M. Henry and K. Longsdale, International Tables for X-Ray Crystallography (Kynoch Press, Birmingham, 1952), Vol. 1.
4. B. Aronsson, Acta Chem. Scand. 14, 1414 (1960).
5. W. Hume-Rothery and G. Raynor, Proc. Roy. Soc. (London) A177, 27 (1940).
6. W. B. Pearson, A Handbook of Lattice Spacings and Structures of Metals and Alloys (Pergamon Press, New York, 1957), Vol. 1 and Vol. 2 (1967).
7. H. Jones, Proc. Roy. Soc. (London) A144, 224 (1934).
8. H. Jones, Proc. Roy Soc. (London) A147, 396 (1934).
9. H. Jones, Phil. Mag. 41, 663 (1950).
10. J. B. Goodenough, Phys. Rev. 89, 282 (1953).
11. D. W. Leviason, Acta Met. 3, 294 (1955).
12. F. H. Herbstein and B. L. Averbach, Acta Met. 4, 407 (1956).
13. G. V. Raynor, Proc. Roy. Soc. (London) A174, 457 (1957).
14. T. B. Massalski and H. W. King, Progr. Mater. Sci. 10, 56 (1961).
15. C. C. Tsuei and L. R. Newkirk, Phys. Rev. 183, 619 (1969).
16. T. Shinjo, Y. Nakamura and N. Shikazono, J. Phys. Soc. (Japan) 18, 797 (1963).
17. Y. Lecocq, P. Lecocq, and A. Michel, C. R. Acad. Sci. Paris 258, 5655 (1964).
18. C. E. Johnson, J. B. Forsyth, G. H. Lander and P. J. Brown, J. Appl. Phys. 39, 465 (1968).

19. G. H. Lander, P. J. Brown and J. B. Forsyth, Proc. Phys. Soc. 91, 332 (1967).

20. K.S.V.L. Narasimham, W. M. Reiff, H. Steinfink and R. L. Collins, J. Phys. Chem. Solids 31, 1511 (1970).

21. H. F. Sterling and R. W. Warren, Metallurgia 67, 301 (1963).

22. M. Hansen and K. Anderko, Constitution of Binary Alloys (McGraw-Hill, New York, 1958) p. 110.

23. See, for example, B. D. Cullity, Elements of X-Ray Diffraction (Addison-Wesley, Reading, Mass., 1956), Chapters 6, 10, and 11.

24. H. M. Lester, Photo-Lab-Index, Margan and Lester, N. Y., 1954.

25. E. Kankeleit, in Mössbauer Effect Methodology (Plenum, New York, 1965) Vol. 1, pp. 47-66.

26. R. S. Preston, S. S. Hanna, and J. Heberle, Phys. Rev. 128, 2207 (1962).

27. M. E. Weiner, Ph.D. Thesis, California Institute of Technology (1968).

28. G. K. Wertheim, Mössbauer Effect: Principles and Applications, (Academic Press, New York, 1964).

29. J. D. Jackson, Classical Electrodynamics (John Wiley and Sons, New York, 1962) p. 101.

30. H. Wegener, Der Mossbauer-Effekt und Seine Anwendungen in Physik und Chemie (Bibliographisches Institut AG. Manheim, 1965) .

31. S. Ofer, P. Avivi, R. Bauminger, A. Marinov and S. G. Cohen, Phys. Rev. 120, 406 (1960).

32. R. L. Cohen, Phys. Rev. 134, A94 (1964).

33. W. Marshall, Phys. Rev. 110, 1280 (1958).

34. W. Marshall and C. E. Johnson, J. Phys. Radium 23, 733 (1962).

35. R. L. Mossbauer and M. J. Clauser in Hyperfine Interactions, (Academic Press, New York, 1967) Chap. 11.

36. R. L. Mössbauer, Lecture Notes at California Institute of Technology, Pasadena, 1971 (unpublished).

37. J. S. Smart, Effective Field Theories of Magnetism (W. B. Saunders Co., Philadelphia, 1966).

38. A. H. Morrish, The Physical Principles of Magnetism (John Wiley and Sons, New York, 1965).

39. L. Néel, Science **174**, 985 (1971).

40. P. Weiss, J. Phys. Radium **4**, 661 (1907).

41. C. Kittel, Introduction to Solid State Physics, 3rd edition (John Wiley and Sons, New York, 1966).

42. F. J. Blatt, Physics of Electronic Conduction in Solids (McGraw-Hill, New York, 1968).

43. T. B. Massalski and H. W. King, Tables of Crystallographic Functions for Calculating Lattice Parameters of Hcp Metals and Alloys from X-Ray Diffraction Data (Mellon Institute, 1960).

44. M. F. Bent, B. I. Persson and D. G. Agresti, Comput. Phys. Comm. **1**, 67 (1969).

45. W. E. Wallace, J. Chem. Phys. **41**, 3857 (1964).

46. L. Vegard, Z. Physik **5**, 17 (1921).

47. D. H. Martin, Magnetism in Solids (M.I.T. Press, Cambridge, Mass. 1967).

48. T. E. Sharon and C. C. Tsuei, Phys. Rev. B**2**, 2302 (1970).

49. S. Alexander and D. Treves, Phys. Letters **20**, 134 (1966).

50. R. V. Pound, G. B. Benedek and R. Drever, Phys. Rev. Letters **7**, 405 (1961).

51. D. N. Pipkorn, C. K. Edge, P. Debrunner, G. DePasquali, H. G. Drickamer and H. Frauenfelder, Phys. Rev. **135**, A1604 (1964).

52. G. K. Wertheim, V. Jaccarino, J. H. Wernick and D.N.E. Buchanan, Phys. Rev. Letters 12, 24 (1964).

53. G. Bemski, J. Danon, A. deGraaf and X. A. da Silva, Phys. Letters 18, 213 (1965).

54. W. Marshall, T. E. Cranshaw, C. E. Johnson and M. S. Ridont, Rev. Mod. Phys. 36, 399 (1964).

55. G. B. Benedek and J. Armstrong, J. Appl. Phys. 32, 1065 (1961).

56. P. R. Craig, R. C. Perisho, R. Segnan and W. A. Steyert, Phys. Rev. 138A, 1460 (1965).

57. C. E. Johnson, A.E.R.E., Harwell, England, Private communication.

58. F. van der Wonde and A. J. Dekker, Phys. Stat. Sol. 13, 181 (1966).

59. D. E. Nagle, H. Frauenfelder, R. D. Taylor, D.R.F. Cochran, and B. T. Matthias, Phys. Rev. Letters 5, 364 (1960).

60. D.N.E. Buchanan and G. K. Wertheim, Bull. Am. Phys. Soc. [2] 7, 227 (1962).

61. G. T. Meaden, Electrical Resistance of Metals (Plenum Press, New York, 1965).

62. J. Bardeen, Phys. Rev. 52, 688 (1937).

63. F. Bloch, Z. Physik 52, 555 (1928).

64. F. Bloch, Z. Physik 53, 216 (1929).

65. F. Bloch, Z. Physik 59, 208 (1930).

66. J. M. Ziman, Proc. Roy. Soc. (London) A226, 436 (1954).

67. M. Kohler, Z. Physik 124, 772 (1948).

68. M. Kohler, Z. Physik 125, 679 (1949).

69. E. H. Sondheimer, Proc. Roy Soc. (London) A203, 75 (1950).

70. B. R. Coles, Adv. Phys. (Phil. Mag. Suppl.) 7, 40 (1958).

71. R. V. Bellan and B. R. Coles, Proc. Phys. Soc. 82, 121 (1963).

72. A. Overhauser, J. Phys. Chem. Solids 13, 71 (1960).

73. R. A. Erickson, Phys. Rev. 90, 779 (1953).

74. G. T. Meaden and P. Pellows-Gervais, Cryogenics 5, 227 (1965).